UNIVERSITAT POLITÈCNICA DE VALÈNCIA

School of Telecommunications Engineering

Analysis and experimental characterization of an entangled photon pair distribution system

End of Degree Project

Bachelor's degree in Engineering Physics

AUTHOR: López Muñoz, Samuel

Tutor: Ortega Tamarit, Beatriz

External cotutor: Zvanovec, Stanislav

Experimental director: Guerra Yánez, Carlos

ACADEMIC YEAR: 2025/2026

Abstract

This work presents the design, analysis, implementation, and characterization of an entangled-photon-pair distribution system between two laboratory nodes at the Czech Technical University in Prague.

The work begins with the characterization of the entangled photon source, combining photon-counting measurements of the pair-generation rate with quantum-state tomography of its polarization density matrix. Several fiber configurations are analyzed and compared, motivated by the diagnosis of polarization mode dispersion as a source of entanglement degradation in broadband sources; this diagnosis is supported by both an analytical model and a numerical density-matrix simulation. A set of entanglement metrics is then computed to characterize the polarization state produced by the source. The validated configuration is used to distribute the entangled photon pairs through the building's optical fiber infrastructure connecting the two laboratories, and the resulting coincidence rates are compared against independent loss measurements obtained by optical time-domain reflectometry and direct power characterization. The angular sensitivity of the tomographic reconstruction is assessed through a Monte Carlo analysis. The results are compared with the theoretical predictions made earlier in the thesis, and possible extensions of the system are outlined.

Resumen

Este trabajo presenta el diseño, análisis, implementación y caracterización de un sistema de distribución de pares de fotones entrelazados entre dos nodos de laboratorio en la Universidad Técnica Checa de Praga.

El trabajo comienza con la caracterización de la fuente de fotones entrelazados, combinando medidas de conteo de fotones con tomografía de estado cuántico para obtener la matriz de densidad. Se analizan y comparan varias configuraciones de montaje, condicionadas por la dispersión por modo de polarización como fuente de degradación del entrelazamiento en fuentes de banda ancha, respaldadas por un modelo analítico y una simulación numérica de la matriz de densidad. A continuación, se calcula un conjunto de métricas de entrelazamiento para caracterizar el estado producido por la fuente. La configuración validada se emplea para distribuir los pares de fotones a través de la infraestructura de fibra óptica del edificio que conecta ambos laboratorios, comparando las tasas de coincidencia con medidas de pérdidas independientes obtenidas mediante reflectometría óptica y mediante la caracterización de la potencia. La sensibilidad angular de la reconstrucción tomográfica se evalúa mediante un análisis de Monte Carlo. Los resultados se comparan con las predicciones teóricas del trabajo y se presentan posibles extensiones del sistema.

Resum

Este treball presenta el disseny, anàlisi, implementació i caracterització d'un sistema de distribució de parells de fotons entrellaçats entre dos nodes de laboratori en la Universitat Tècnica Txeca de Praga.

El treball comença amb la caracterització de la font de fotons entrellaçats, combinant mesures de comptatge de fotons amb tomografia d'estat quàntic per a obtindre la matriu de densitat. S'analitzen i comparen diverses configuracions de muntatge, condicionades per la dispersió per mode de polarització com a font de degradació de l'entrellaçament en fonts de banda ampla, recolzades per un model analític i una simulació numèrica de la matriu de densitat. A continuació, es calcula un conjunt de mètriques d'entrellaçament per a caracteritzar l'estat produït per la font. La configuració validada s'empra per a distribuir els parells de fotons a través de la infraestructura de fibra òptica de l'edifici que connecta els dos laboratoris, comparant les taxes de coincidència amb mesures de pèrdues independents obtingudes mitjançant reflectometria òptica i mitjançant la caracterització de la potència. La sensibilitat angular de la reconstrucció tomogràfica s'avalua mitjançant una anàlisi de Montecarlo. Els resultats es comparen amb les prediccions teòriques del treball i es presenten possibles extensions del sistema.

RESUMEN EJECUTIVO

La memoria del TFG del GIFIS debe desarrollar en el texto los siguientes conceptos, debidamente justificados y discutidos, centrados en el ámbito de la Physics Engineering

CONCEPT (ABET)	**CONCEPTO (traducción)**	**Done? (Y/N)**	**Where? (pages)**
1. IDENTIFY:	1. IDENTIFICAR:		
1.1. Problem statement and opportunity	1.1. Planteamiento del problema y oportunidad	Y	2-3, 5-6
1.2. Constraints (standards, codes, needs, requirements & specifications)	1.2. Toma en consideración de los condicionantes (normas técnicas y regulación, necesidades, requisitos y especificaciones)	Y	5-6, 8, 40-41, 43-46
1.3. Setting of goals	1.3. Establecimiento de objetivos	Y	7-8
2. FORMULATE:	2. FORMULAR:		
2.1. Creative solution generation (analysis)	2.1. Generación de soluciones creativas (análisis)	Y	37-40, 54-55
2.2. Evaluation of multiple solutions and decision-making (synthesis)	2.2. Evaluación de múltiples soluciones y toma de decisiones (síntesis)	Y	37-41
3. SOLVE:	3. RESOLVER:		
3.1. Fulfilment of goals	3.1. Evaluación del cumplimiento de objetivos	Y	74-75
3.2. Overall impact and significance (contributions and practical recommendations)	3.2. Evaluación del impacto global y alcance (contribuciones y recomendaciones prácticas)	Y	75-76

Contents

List of Figures

UNIVERSITAT POLITÈCNICA DE VALÈNCIA

_ TELECOM ESCUELA TÉCNICA VLC SUPERIOR DE INGENIERÍA DE TELECOMUNICACIÓN

List of Tables

List of acronyms used

CAR Coincidence-to-Accidental Ratio.

CLT Central Limit Theorem.

CTU Czech Technical University in Prague.

DCR Dark Count Rate.

EPPS Entangled Photon Pair Source.

FWHM Full Width at Half Maximum.

HWP Half-Wave Plate.

MLE Maximum Likelihood Estimation.

OTDR Optical time-domain reflectometry.

PBS Polarizing Beam Splitter.

PM Polarization-Maintaining (fiber).

PMD Polarization Mode Dispersion.

PPKTP Periodically Poled Potassium Titanyl Phosphate ($KTiOPO_4$).

QPM Quasi-Phase-Matching.

QST Quantum State Tomography.

QWP Quarter-Wave Plate.

SDG Sustainable Development Goal.

SMF Single-Mode Fiber.

SNR Signal-to-Noise Ratio.

SPAD Single Photon Avalanche Diode.

SPDC Spontaneous Parametric Down-Conversion.

UPV Universitat Politècnica de València.

WDM Wavelength Division Multiplexing.

List of symbols

Quantum states and operators

α, β	Complex amplitudes of a qubit superposition
θ, φ	Polar and azimuthal angles on the Poincaré sphere
$\vec{r}$	Bloch vector; $\vec{r} = (r_x, r_y, r_z) \in \mathbb{R}^3$, $\|\vec{r}\| \leq 1$
$\mathcal{H}$	Single-qubit polarisation Hilbert space; $\mathcal{H} \cong \mathbb{CP}^1$
$\mathbb{CP}^1$	Complex projective space (of single-qubit states)
$\mathcal{H}_A, \mathcal{H}_B$	Single-photon polarisation Hilbert spaces
$\mathcal{H}_{AB}$	Two-photon joint Hilbert space; $\mathcal{H}_A \otimes \mathcal{H}_B$
$\hat{\rho}$	Two-qubit polarization density matrix
$\hat{\rho}_A$	Reduced density matrix of photon A, obtained by tracing out photon B
$\hat{\rho}^{T_B}$	Partial transpose of $\hat{\rho}$ with respect to photon B
$\tilde{\rho}$	Spin-flipped density matrix used in the concurrence calculation
R	Matrix $R = \sqrt{\sqrt{\hat{\rho}}\,\tilde{\rho}\,\sqrt{\hat{\rho}}}$ used to compute concurrence
$\|\psi\rangle$	Pure quantum state (ket vector)
$\langle\psi\|$	Dual state (bra vector)
$\|e_i\rangle$	Eigenvectors of $\hat{\rho}$; $\hat{\rho}\,\|e_i\rangle = \lambda_i\,\|e_i\rangle$
$\|e_1\rangle$	Dominant eigenvector of $\hat{\rho}$
λ_i	Eigenvalues of $\hat{\rho}$; $\lambda_i \geq 0$, $\sum_i \lambda_i = 1$
λ_1	Dominant eigenvalue of $\hat{\rho}$; equals $F_{\max}$
$\|\Phi^\pm\rangle$	Maximally entangled Bell states $\frac{1}{\sqrt{2}}(\|HH\rangle \pm \|VV\rangle)$
$\|\Psi^\pm\rangle$	Maximally entangled Bell states $\frac{1}{\sqrt{2}}(\|HV\rangle \pm \|VH\rangle)$
$\hat{\Pi}_k$	Polarization projector for measurement setting k
$\hat{\Pi}_{\text{pol}}(\theta)$	Polarizer projector at angle θ
$\otimes$	Tensor (Kronecker) product
$\hat{\sigma}_0, \hat{\sigma}_1, \hat{\sigma}_2, \hat{\sigma}_3$	Single-qubit Pauli matrices (I, X, Y, Z)

$\hat{T}_j$	Two-qubit Pauli operator basis element; $T_j = \sigma_a \otimes \sigma_b$, with $a, b \in \{0, 1, 2, 3\}$, $j = 1, \ldots, 16$
$\mathbb{I}$	Identity matrix

Figures of merit

$\mathrm{Tr}(\hat{\rho}^2)$	Purity of the quantum state
$\mathcal{P}(\hat{\rho})$	Global purity of the two-photon density matrix
$\mathcal{P}(\hat{\rho}_A)$	Purity of the reduced density matrix of photon A
$C(\hat{\rho})$	Concurrence (entanglement measure)
$E_F(\hat{\rho})$	Entanglement of formation
$\mathcal{N}(\hat{\rho})$	Negativity
$E_N(\hat{\rho})$	Logarithmic negativity
$F(\hat{\rho}, \hat{\sigma})$	Fidelity between states $\hat{\rho}$ and $\hat{\sigma}$
$F_{\max}$	Fidelity to the closest pure state
$S(\hat{\rho}_A)$	Von Neumann entropy
$h(x)$	Binary entropy function
$\|\cdot\|_1$	Trace norm
$\|\cdot\|_F$	Frobenius norm
$\hat{\rho}_W(p)$	Werner-state model with mixing parameter p
p	Werner-state mixing parameter

Quantum State Tomography

n_k	Experimental net coincidence count for measurement k
μ_k	Expected (Poisson-mean) coincidence count predicted by $\hat{\rho}$
$n_k^{(\mathrm{sim})}$	Simulated coincidence count in the Monte Carlo analysis
$\mu_k^{(\mathrm{real})}$	Expected coincidence count; $N_{\mathrm{total}} \cdot P_k^{(\mathrm{real})}$
N	Total photon pairs emitted per acquisition window (normalization)
$\vec{t}$	Vector of 16 real expansion coefficients of $\hat{\rho}$ in the T_j basis
A	Design matrix (36×16); $A_{k,j} = \frac{1}{4}\mathrm{Tr}(T_j\,\Pi_k)$
A^+	Moore–Penrose pseudoinverse of A
T	Lower-triangular Cholesky support matrix; $\hat{\rho} = T^\dagger T/\mathrm{Tr}(T^\dagger T)$

$\mathcal{L}(\hat{\rho})$	Poisson likelihood function
$f(\hat{\rho})$	Negative log-likelihood cost function (minimized in MLE)

Photon source and detection

γ	Photon emission rate (Poisson process rate parameter)
η	Detector quantum efficiency
τ_d	Dead time; recovery interval after each detection
τ_j	Timing jitter (FWHM); uncertainty in detection timestamp
$\Delta\lambda$	Spectral bandwidth (FWHM) of the photon source
Δf	Frequency bandwidth; $\Delta f \approx (c/\lambda_0^2)\,\Delta\lambda$
Δt	Photon coherence time (wave-packet duration); $\Delta t \approx 1/\Delta f$
λ_0	Central wavelength of the photon source

Fiber and polarization

$\Delta\tau$	PMD-induced temporal delay between $\|H\rangle$ and $\|V\rangle$ components
U	2×2 unitary Jones matrix of a fiber or optical component
ϕ_H, ϕ_V	Phase accumulated by horizontal and vertical polarization modes
$U_{\text{HWP}}(\theta), U_{\text{QWP}}(\theta)$	Jones matrices of the HWP and QWP at angle θ
$\delta_{\text{wp}}, \delta_{\text{pol}}$	Angular errors on the waveplate and polarizer; $\delta \sim \mathcal{N}(0, 1^\circ)$
$\omega_p, \omega_s, \omega_i$	Angular frequencies of pump, signal and idler photons; $\omega_p = \omega_s + \omega_i$
$\mathbf{k}_p, \mathbf{k}_s, \mathbf{k}_i$	Wave vectors of pump, signal and idler; phase-matching condition $\mathbf{k}_p = \mathbf{k}_s + \mathbf{k}_i$
Δn	Fiber birefringence; $\Delta n = n_s - n_f$
L_b	Beat length of PM fiber; $L_b = \lambda/\Delta n$
M_{PM}	Jones matrix of PM fiber (diagonal phase retarder)
σ_ω	Standard deviation of the angular frequency spectrum
Δn_{SMF}	Residual birefringence of SMF-28 fiber $\approx 5 \times 10^{-7}$ ($L = 3\,\text{m}$)
Δn_{PM}	Birefringence of PM (PANDA) fiber $\approx 4 \times 10^{-4}$

Part I

Thesis

Chapter 1.

Introduction

1.1 Context and motivation

The history of technology follows a pattern. First, a new physical principle is understood, then exploited, then built into infrastructure so pervasive that a generation later people cannot imagine the world without it. The transistor followed that arc. So did the optical fiber. Each of these not only opened the door to new applications but new ways of thinking about what problems are worth solving. Quantum technologies are at an earlier point on that same curve—beyond the stage of mere scientific curiosity, but without having yet reached the stage of widespread deployment—and the physics involved is so strange that its implications are still being studied

What makes quantum mechanics unusual, from an engineering standpoint, is that its most counterintuitive features are also its most useful ones. Superposition, entanglement, and the no-cloning theorem are not theoretical errors; they are real properties we can use. Two photons produced together in a certain type of nonlinear optical process share correlations that persist regardless of the distance between them and that cannot be explained by any locally pre-assigned hidden variable [1]. That nonlocality is what makes entanglement a resource for the communication protocols described below, even though entanglement alone cannot transmit information; this no-signalling property is itself a deep and useful constraint, not a limitation to work around.

The connection to cryptography was made explicit in 1984 by Bennett and Brassard [2], who showed that encoding a key in quantum states makes eavesdropping physically detectable. Ekert extended this idea in 1991 by showing that entangled photon pairs could play the same role, with Bell inequality violations as a direct security certificate [3]. The experimental side took on importance in 1995, when Kwiat et al. demonstrated a practical source of polarization-entangled photon pairs via type-II spontaneous parametric down-conversion (SPDC) [4], turning entangled-photon experiments from specialized demonstrations into reproducible laboratory tools.

Beyond QKD, the same entangled pairs are the essential resource for a wider family of quantum communication protocols: superdense coding, which uses a pre-shared entangled pair to transmit two classical bits by sending only one physical qubit, effectively doubling the classical capacity of the qubit actually transmitted; quantum teleportation, which transfers an unknown quantum state between distant nodes without physically sending the particle; and entanglement swapping, which extends entanglement to nodes that have never directly interacted—the primitive that makes quantum repeaters possible. These applications are introduced briefly here because they define the long-term context of the present work; they are developed in Chapter 6.

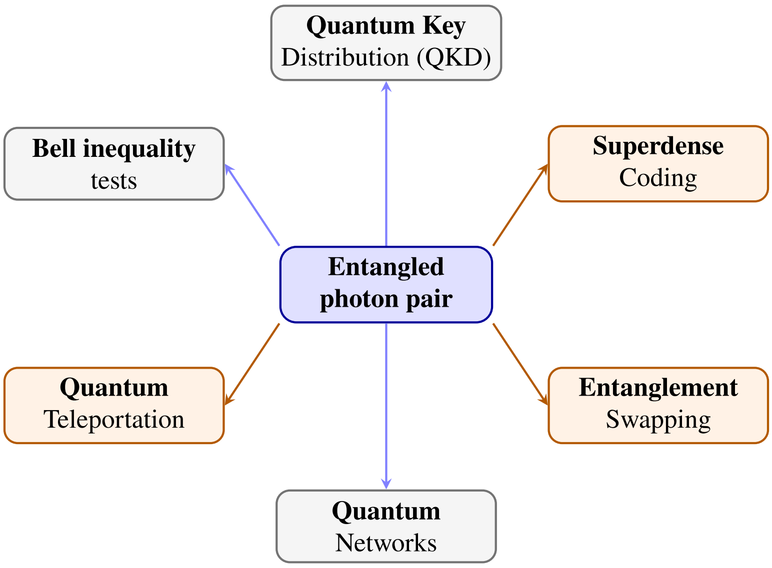

Figure 1: Overview of the primary applications and protocols enabled by polarization-entangled photon pairs in modern quantum technologies.

The institutional response has accelerated in the years since. The European Union launched the EuroQCI initiative in 2019, committing all 27 member states to building a continent-wide quantum communication infrastructure—terrestrial fiber links combined with a satellite segment—targeted for operation by 2027 [5].

This thesis was carried out during a research stay at the Czech Technical University (CTU) in Prague, an opportunity made possible through the supervision of Dr. Beatriz Ortega Tamarit at the Universitat Politècnica de València (UPV). The experimental work was conducted within the optical communications group led by Prof. Stanislav Zvanovec, under the direct guidance of Carlos Guerra Yánez, who supervised the day-to-day laboratory work. The group operates within CTU's inter-building fiber infrastructure, maintained by CESNET—the Czech national research and education network operator—which provided the physical link used for the distribution experiments described in this thesis.

Working experimentally with quantum systems does something that theory alone cannot: it makes the physics feel real. There is a difference between working with entanglement on paper and actually building a setup that produces it. That hands-on contact with the subject changes how you think about the field — and, more than anything, it makes the potential applications feel within reach rather than speculative.

1.2 State of the art

The distribution of entangled photon pairs via optical fiber has been a very active field of research for around three decades. The general trend is towards a steady increase in range, driven by advances in low-noise single-photon detectors and ultra-low-loss optical fiber. The accessible distances have grown from a few kilometres in early table-top experiments to intercontinental scales via satellite. Figure 2 places the key milestones in context.

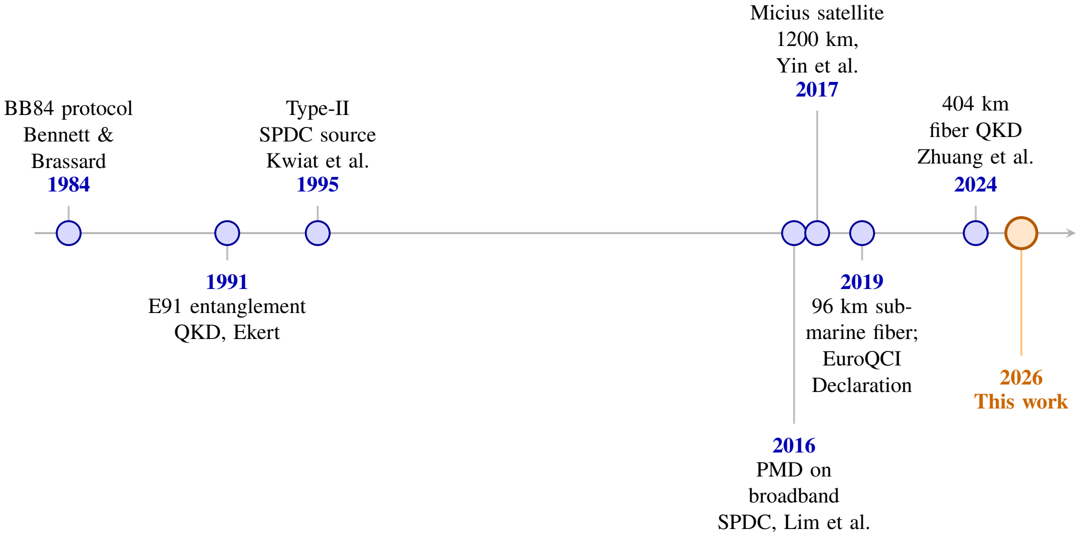

Figure 2: Selected milestones in quantum communication and entangled photon distribution, from the first quantum key distribution proposal (1984) to the present work (2026). Note the compressed spacing between the 2016–2026 events relative to the earlier decades.

Long-distance demonstrations have pushed fiber-based entanglement distribution to 96 km over a deployed submarine cable [6] and, more recently, to 404 km using ultra-low-loss fiber and superconducting nanowire single-photon detectors [7]. Free-space and satellite-based distribution have reached further: Yin et al. demonstrated entanglement between ground stations separated by over 1200 km using the Micius satellite [8], a distance that cannot be covered by fiber at any practical level of loss.

However, distance limitations are not the main obstacle to its implementation at present. Metropolitan-scale links—hundreds of metres to a few kilometres over existing cables—are the area where viable systems are currently being deployed, and the main challenges at that scale are not photon loss, but the control of polarisation. Standard single-mode fiber (SMF) exhibits a residual birefringence due to manufacturing imperfections and environmental stress. This birefringence varies along the cable and drifts with temperature and mechanical perturbation, rotating the polarization state in an uncontrolled way. Polarization-maintaining fiber (PM) eliminates this drift but introduces a different problem: its large and fixed birefringence causes a temporal differential group delay between the two polarization modes that, in the case of broadband sources, it is large enough to cause decoherence.

This is the mechanism studied by Lim et al. [9], who analysed the effect of polarization mode dispersion (PMD) on polarization-entangled photons from a broadband SPDC source. When the differential group delay accumulated in the fiber becomes comparable to the single-photon coherence time, information about the photon's polarization leaks into the temporal degree of freedom and the polarization entanglement degrades. The mitigation options are: reducing the source bandwidth with narrowband spectral filters, switching to standard SMF (whose birefringence is orders of magnitude smaller), or applying polarization compensation at the receiver. This work addresses the first two strategies.

Quantum state tomography (QST) is the standard tool for characterizing the reconstructed two-photon state. The protocol, based on coincidence measurements in 36 polarization projections, was described by James et al. [10] and reviewed in detail by Altepeter et al. [11]. Maximum-likelihood estimation with Cholesky parametrization is now the preferred reconstruction method because it guarantees a physical density matrix regardless of statistical noise in the measurement data [12]. Both the protocol and the reconstruction algorithm are used throughout this work without modification.

1.3 Problem statement, scope and limitations

This thesis forms part of a broader collaboration between CTU and CESNET, with the project scheduled to run until September 2026. The overall goal is a working quantum communication link between two laboratory nodes at CTU, connected through CESNET's inter-building fiber infrastructure. The present work covers the first phase: characterizing the entangled photon pair source (EPPS), identifying and mitigating the main decoherence mechanism, and distributing entangled photons over the available fiber link with a quantitative comparison against theoretical predictions. The subsequent phases of the project, which fall outside the scope of this thesis, aim to extend the system to more than two nodes, establishing entanglement dynamically between multiple terminals through time-division multiplexing of the photon pairs.

The project was divided into three main sections: source characterization, distributing entangled photon pairs through CTU fiber infrastructure, and comparing experimental performance against theoretical predictions.

The source characterization was the most laborious part, due to the high sensitivity of photon polarization and to the difficulty of controlling all the external variables that influence the process. Along the way, we encountered quite a few difficulties that we had to overcome to achieve the most pure source state possible.

The starting point was: Connect the EPPS source to two Single Photon Avalanche Diode (SPAD) detectors using the laboratory's fiber-optic connection cables, perform a full QST using waveplates, and characterize the state. The first reconstruction returned a purity of 0.28 — far below anything consistent with a usable entangled state. Rather than a technical failure, this was a diagnostic result: It appeared to be a physical mechanism that degraded the entanglement before the photons reached the detectors.

Identifying that mechanism and progressively eliminating it became the central thread of the experimental work. The source produces photon pairs with a per-photon spectral bandwidth of approximately 25 nm FWHM (Full Width at Half Maximum) at 1310 nm (Photon pair spectrum 50 nm FWHM). That broadband spectrum makes the state particularly sensitive to PMD in the connecting fiber: in a birefringent medium, each wavelength component of the photon accumulates a different phase shift, and what the detector detects is an average of a distribution of polarisation states, rather than a single, well-defined state. The polarization-maintaining fibers available in the laboratory have a birefringence large enough to destroy measurable entanglement over distances of a few meters, consistent with the theoretical predictions of Lim et al. [9].

Once the cause was identified, we tried to fix it with different methods: Narrowband spectral filters to reduce the photon bandwidth, fixing the fibers, replacing the PM fiber with a standard single-mode fiber (SMF), whose birefringence is three orders of magnitude smaller. Each configuration was characterized using a full QST with maximum-likelihood reconstruction, so that changes between steps could be quantitatively tracked rather than inferred. By the final local configuration, the reconstructed state reached a purity of 0.79 — sufficient to demonstrate clear entanglement and proceed to the distribution experiment.

That second phase used the same optimized setup to feed a 738 meter looped fiber path through CTU's inter-building infrastructure to a second laboratory node. The coincidence rate at the SPAD's was measured and compared against the theoretical prediction derived from Optical time-domain reflectometry (OTDR) fiber-loss measurements — the objective at this stage was to verify that entangled pairs survived the channel at a useful rate, not to perform a full state reconstruction at the far end. The full progression from initial characterization to final distribution, including all intermediate configurations and the Monte Carlo uncertainty analysis, is developed in Chapters 4 and 5.

1.4 Document structure

Chapter 2 states the general and specific objectives and describes the methodology. Chapter 3 covers the theoretical background: polarization qubits and entanglement, the SPDC process, single-photon detection, the PMD decoherence model, the QST protocol, and the entanglement metrics used throughout the work. Chapter 4 describes the system architecture, the equipment, and the measurement protocols. Chapter 5 presents the experimental results in the order they were obtained, from initial detector characterization through successive improvements in the local QST setup to the distribution experiment. Chapter 6 concludes the thesis by evaluating the project's achievements against its objectives and suggesting potential lines of future work.

Chapter 2.

Objectives

2.1 General objective

The general objective of this thesis is to design, implement, and characterize an entangled photon pair distribution system between two terminal nodes connected through the optical fiber infrastructure of the Czech Technical University, evaluating the performance of the implemented system against theoretical predictions derived from the characterization of the source and the optical fiber link loss measurements.

2.2 Specific objectives

1. Measure the dark count rate of each SPAD detector and select the two units with the most similar noise background for use in the experiment (**Detector characterization**).

2. Measure the coincidence histogram of the EPPS source and extract the key figures of merit: coincidence rate, average background, SNR and CAR (**Source characterization**).

3. Reconstruct the two-photon polarization density matrix of the EPPS source through four successive QST experimental runs, progressively mitigating PMD-induced decoherence, and compute the full set of entanglement metrics from the final reconstruction (**Quantum state tomography of the source**).

4. Measure the attenuation of the complete fiber link using an OTDR and a power meter, and develop a theoretical model that predicts the expected coincidence rate at the receiving end from the source characterization and the measured link loss parameters (**Distribution system characterization and modeling**).

5. Implement the distribution scheme through the CTU inter-building fiber infrastructure and compare the measured coincidence rate against the theoretical prediction (**Entanglement distribution**).

2.3 Methodology overview

The experimental work followed an iterative approach. Each modification to the setup was evaluated through a complete QST stages, so that changes in the reconstructed state could be tracked quantitatively and attributed to specific physical causes, rather than to statistical fluctuations. This measurement-driven cycle — modify, reconstruct, diagnose — was the backbone of the source characterization work.

The theoretical framework served as a guide throughout. Understanding the PMD decoherence mechanism described by Lim et al. [9] allowed the identification of the root cause of the initial low-purity results and directed the subsequent optimization of the experimental design. The theory did not prescribe exact solutions analytically, but it provided the conceptual tools to interpret each result and decide the next step.

For the distribution experiment, the fiber link attenuation was measured prior to implementation using an OTDR and a power meter. The theoretical predictions derived from those measurements and the source characterization were in good agreement with the coincidence rates subsequently observed at the final detectors, validating both the measurement protocol and the system model.

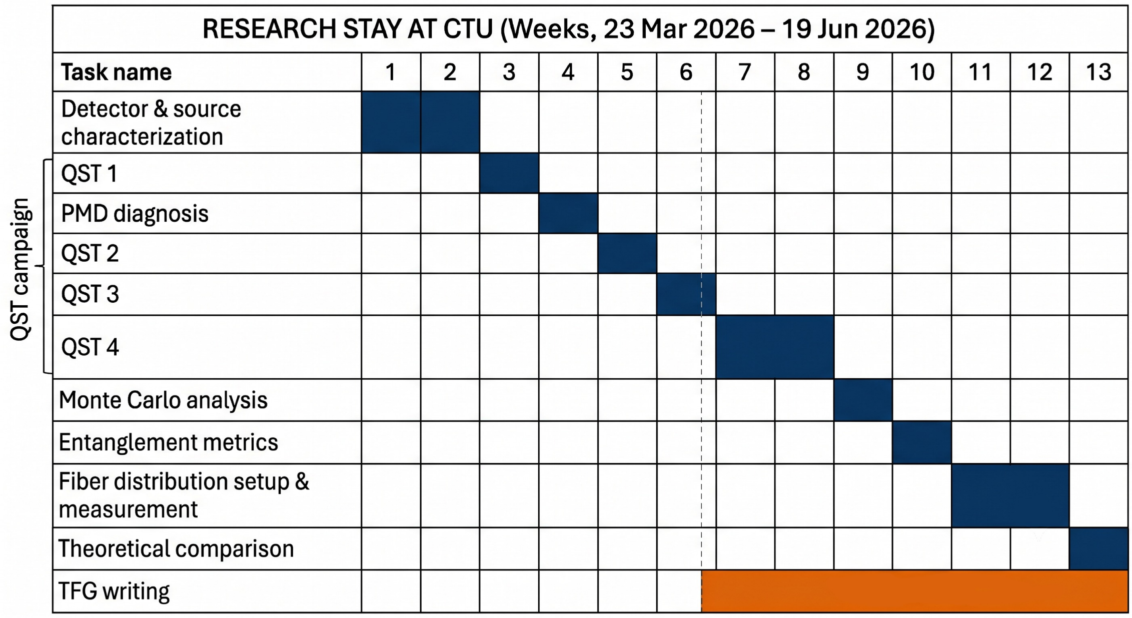

Figure 3: Project timeline during the research stay at CTU (23 March – 23 June 2026), showing the sequence of experimental phases, the QST characterization campaign, and the overlap with TFG writing.

Chapter 3.

Theoretical background

This chapter develops the theoretical basis required to understand the experimental work, from quantum and optics fundamentals to the mathematical framework of quantum state tomography.

3.1 Quantum states and polarization

Among the degrees of freedom of a photon, polarization can be particularly useful for quantum information applications: its state space is two-dimensional, so that any polarization measurement has exactly two orthogonal possible outcomes, it can be manipulated with standard optical elements, and it is robust against decoherence in free-space transmission [9]. A photon whose only relevant degree of freedom is polarization therefore constitutes a *qubit* — a two-level quantum system — and its state lives in a two-dimensional complex Hilbert space $\mathcal{H} \cong \mathbb{C}^2$ [1]; once global phase and normalization are removed, the space of physically distinct states is the projective space $\mathbb{CP}^1$, which is what is actually parametrized by the Bloch sphere introduced below.

The polarization qubit

The natural basis for a polarization qubit is the horizontal–vertical (H/V) linear polarization basis, which serves as the computational basis throughout this work [13]:

$$|H\rangle = \begin{pmatrix} 1 \\ 0 \end{pmatrix}, \qquad |V\rangle = \begin{pmatrix} 0 \\ 1 \end{pmatrix}. \tag{3.1}$$

Four additional polarization states are used in the tomographic measurements (see Section 4.4). Table 6 lists all six in terms of $|H\rangle$ and $|V\rangle$.

Table 6: The six single-photon polarization states used in the QST protocol, expressed in the H/V computational basis. D/A: diagonal/anti-diagonal linear polarization; R/L: right/left circular polarization. Convention follows [13, 1].

State	Ket expression	Jones vector
$\|H\rangle$	$\|H\rangle$	$(1,\ 0)^T$
$\|V\rangle$	$\|V\rangle$	$(0,\ 1)^T$
$\|D\rangle$	$\frac{1}{\sqrt{2}}(\|H\rangle + \|V\rangle)$	$\frac{1}{\sqrt{2}}(1,\ 1)^T$
$\|A\rangle$	$\frac{1}{\sqrt{2}}(\|H\rangle - \|V\rangle)$	$\frac{1}{\sqrt{2}}(1,\ -1)^T$
$\|R\rangle$	$\frac{1}{\sqrt{2}}(\|H\rangle + i\|V\rangle)$	$\frac{1}{\sqrt{2}}(1,\ i)^T$
$\|L\rangle$	$\frac{1}{\sqrt{2}}(\|H\rangle - i\|V\rangle)$	$\frac{1}{\sqrt{2}}(1,\ -i)^T$

The pairs $\{H, V\}$, $\{D, A\}$ and $\{R, L\}$ each form an orthonormal basis of $\mathcal{H}$, corresponding to the three axes of the Poincaré sphere introduced below.

Pure states

A pure state is a system where you have complete information and know exactly which state it is in, a well-defined quantum state. The most general pure state of a polarization qubit is a coherent superposition of the basis states [1],

$$|\psi\rangle = \alpha\,|H\rangle + \beta\,|V\rangle\,, \qquad \alpha, \beta \in \mathbb{C}, \quad |\alpha|^2 + |\beta|^2 = 1, \tag{3.2}$$

where $|\alpha|^2$ and $|\beta|^2$ are the probabilities of measuring horizontal and vertical polarization, respectively. The global phase of $|\psi\rangle$ is physically unobservable and is conventionally set to zero, leaving only the relative phase between α and β as a significant quantity.

A convenient parametrization that makes the geometry explicit is

$$|\psi\rangle = \cos\frac{\theta}{2}\,|H\rangle + e^{i\varphi}\sin\frac{\theta}{2}\,|V\rangle\,, \qquad \theta \in [0, \pi], \quad \varphi \in [0, 2\pi), \tag{3.3}$$

which maps every pure state to a unique point on the surface of the unit sphere — the *Poincaré sphere* [13] (or Bloch sphere in the quantum information literature [1]). The north pole ($\theta = 0$) corresponds to $|H\rangle$, the south pole to $|V\rangle$, the equatorial points to the four linearly or circularly polarized states D, A, R, L.

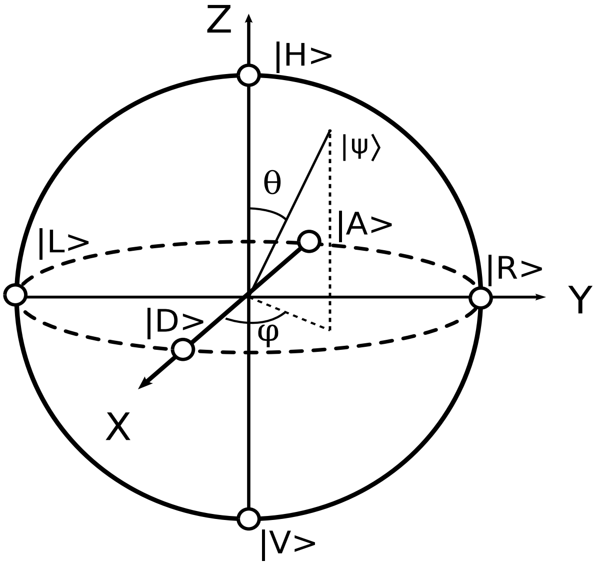

Figure 4: The Poincaré sphere. Every pure polarization state corresponds to a point on the surface, parametrized by the angles θ and φ of Eq. (3.3). The north and south poles correspond to $|H\rangle$ and $|V\rangle$; the equator contains the diagonal (D, A) and circular (R, L) states. Adapted from *Bloch sphere* by Smite-Meister and *Poincaré Sphere with Polarizations* by The-tenth-zdog, Wikimedia Commons, licensed under CC BY-SA 3.0.

The density matrix

In a real experiment, photons are rarely in a pure state. Decoherence, noise, and the statistical nature of the source produce *mixed states*: probabilistic mixtures of different pure states. A mixed state cannot be described by a ket vector; instead, it requires the *density matrix* $\hat{\rho}$ [1]:

$$\hat{\rho} = \sum_i p_i |\psi_i\rangle \langle\psi_i|, \qquad p_i \geq 0, \quad \sum_i p_i = 1, \tag{3.4}$$

where p_i is the classical probability that the photon is in state $|\psi_i\rangle$. The density matrix is the most general description of a quantum state and, in a finite-dimensional Hilbert space, reduces to $\hat{\rho} = |\psi\rangle\langle\psi|$ for a pure state.

For a density matrix to be valid, it must satisfy the following properties [1]:

$$\hat{\rho}^\dagger = \hat{\rho}, \qquad \mathrm{Tr}(\hat{\rho}) = 1, \qquad \langle v|\hat{\rho}|v\rangle \geq 0 \ \ \forall\ |v\rangle \in \mathcal{H}. \tag{3.5}$$

The first condition is Hermiticity; the second is unit trace (normalisation); the third is positive semidefiniteness, which ensures that all probabilities are non-negative.

For a single qubit, the density matrix can always be written in terms of the Bloch vector $\vec{r} = (r_x, r_y, r_z) \in \mathbb{R}^3$ with $\|\vec{r}\| \leq 1$ [12]:

$$\hat{\rho} = \frac{1}{2}\left(\mathbb{I} + r_x\hat{\sigma}_1 + r_y\hat{\sigma}_2 + r_z\hat{\sigma}_3\right) = \frac{1}{2}\left(\mathbb{I} + \vec{r}\cdot\hat{\vec{\sigma}}\right), \tag{3.6}$$

where $\hat{\sigma}_1, \hat{\sigma}_2, \hat{\sigma}_3$ are the Pauli matrices. The three components of $\vec{r}$ correspond to the expectation values of the three Pauli observables and have a direct physical meaning: r_z measures the H/V imbalance, r_x the D/A imbalance, and r_y the R/L imbalance.

Pure versus mixed states

The distinction between pure and mixed states is captured by the *purity* $\mathcal{P} = \mathrm{Tr}(\hat{\rho}^2) \in [1/2,\ 1]$ for a qubit, or equivalently by $\|\vec{r}\|$:

- **Pure state:** $\mathcal{P} = 1$, $\|\vec{r}\| = 1$. The state lies on the surface of the Bloch sphere. $\hat{\rho}$ has eigenvalues $\{1, 0\}$.
- **Mixed state:** $\mathcal{P} < 1$, $\|\vec{r}\| < 1$. The state lies inside the sphere. $\hat{\rho}$ has two positive eigenvalues summing to 1.
- **Maximally mixed state:** $\mathcal{P} = 1/2$, $\vec{r} = \vec{0}$, $\hat{\rho} = \mathbb{I}/2$. The state lies at the centre of the Poincaré sphere. This represents a photon with completely random polarization.

The eigenvalues λ_i of $\hat{\rho}$ are always non-negative (a consequence of positive semidefiniteness) and sum to 1. They quantify how the state is distributed over its eigenvectors, which form an orthonormal basis in which $\hat{\rho}$ is diagonal. A pure state has one eigenvalue equal to 1 and all others zero; a mixed state has at least two non-zero eigenvalues.

Two-qubit systems

The experiment in this work involves *pairs* of photons, each carrying an independent polarization qubit. The joint state of two photons lives in the tensor-product Hilbert space $\mathcal{H}_{AB} = \mathcal{H}_A \otimes \mathcal{H}_B \cong \mathbb{CP}^1 \otimes \mathbb{CP}^1$ [1]. The computational basis of $\mathcal{H}_{AB}$ is formed by the four product states:

$$\big\{ |HH\rangle\,,\ |HV\rangle\,,\ |VH\rangle\,,\ |VV\rangle \big\}, \tag{3.7}$$

where $|XY\rangle \equiv |X\rangle_A \otimes |Y\rangle_B$ and the labels A, B refer to the signal and idler photons of the entangled pair (the physical source producing them is introduced in Section 3.3).

$$|\psi_{AB}\rangle = c_{HH}\,|HH\rangle + c_{HV}\,|HV\rangle + c_{VH}\,|VH\rangle + c_{VV}\,|VV\rangle\,, \qquad \sum_{X,Y} |c_{XY}|^2 = 1, \tag{3.8}$$

and the corresponding density matrix is a 4×4 Hermitian, positive-semidefinite, unit-trace matrix with 15 independent real parameters. Recovering these 15 parameters from experimental data is the central problem of QST, addressed in Section 3.6.

3.2 Entanglement and the density matrix formalism

Section 3.1 established that two-photon states live in $\mathcal{H}_{AB} = \mathcal{H}_A \otimes \mathcal{H}_B$ and introduced the density matrix as the general description of any quantum state. However, not all states in $\mathcal{H}_{AB}$ are equally interesting: the ones that matter most for quantum communication are the *entangled* ones, and this section defines what that means and why it is useful.

Separability and entanglement

A two-photon state $\hat{\rho}_{AB}$ is called *separable* if it can be written as a probabilistic mixture of product states [1]:

$$\hat{\rho}_{AB}^{\text{sep}} = \sum_i p_i\, \hat{\rho}_i^A \otimes \hat{\rho}_i^B, \qquad p_i \geq 0, \quad \sum_i p_i = 1. \tag{3.9}$$

A separable state admits a classical explanation: the correlations between photon A and photon B can be reproduced by a shared classical probability distribution $\{p_i\}$ over local states. A state that cannot be written in this form is *entangled*: its correlations are genuinely non-classical and cannot be reproduced by any classical probability distribution.

For a pure two-photon state, the test is simple. Consider the state $|HH\rangle = |H\rangle_A \otimes |H\rangle_B$: photon A is horizontal and photon B is horizontal, independently. This is separable — it factors into a product of two single-photon states.

By contrast, the state $\frac{1}{\sqrt{2}}(|HH\rangle + |VV\rangle)$ cannot be written as any product $|\phi\rangle_A \otimes |\chi\rangle_B$: measuring photon A in $|H\rangle$ instantly forces photon B into $|H\rangle$, regardless of the distance between them. This state is entangled.

Bell states

The four *Bell states* are one of the possible maximally entangled pure states of a two-qubit system [1, 10]:

$$|\Phi^\pm\rangle = \frac{1}{\sqrt{2}}\big(|HH\rangle \pm |VV\rangle\big), \qquad |\Psi^\pm\rangle = \frac{1}{\sqrt{2}}\big(|HV\rangle \pm |VH\rangle\big). \tag{3.10}$$

They form an orthonormal basis of $\mathcal{H}_{AB}$ and share three properties that make them the ideal resource for quantum communication: equal measurement probabilities in every polarisation basis, perfect correlations between the two photons, and maximal violation of Bell inequalities.

It is important to highlight that $|\Phi^\pm\rangle$ and $|\Psi^\pm\rangle$ are only a *basis* of the maximally entangled subspace — they are not the only maximally entangled states. Any unitary combination of them is also maximally entangled. A practical consequence of this is that a real source can produce a maximally entangled state that has low fidelity with all four standard Bell states simply because its polarisation frame is rotated relative to the H/V basis. This is the situation encountered in this experiment, as discussed in Section 5.4.

Eigenstructure of the density matrix

The eigenvalues and eigenvectors of $\hat{\rho}$ carry direct physical information about the state. For a 4×4 density matrix, the eigenvalue equation is

$$\hat{\rho}\, |e_i\rangle = \lambda_i\, |e_i\rangle\,, \qquad i = 1, \ldots, 4, \tag{3.11}$$

where $\lambda_i \geq 0$ and $\sum_i \lambda_i = 1$ (consequences of positive semidefiniteness and unit trace). The eigenvectors $\{|e_i\rangle\}$ form an orthonormal basis in which $\hat{\rho}$ is diagonal:

$$\hat{\rho} = \sum_i \lambda_i\, |e_i\rangle \langle e_i|\,. \tag{3.12}$$

This spectral decomposition has a clear physical interpretation: λ_i is the probability that the system is in the pure state $|e_i\rangle$. A pure state has a single non-zero eigenvalue equal to 1; a mixed state has at least two non-zero eigenvalues. The dominant eigenvector $|e_1\rangle$, associated with the largest eigenvalue λ_1, is the pure state that best approximates $\hat{\rho}$ — represents the fraction λ_1 of the total state and provides the closest description of the system's pure state. This interpretation is used in Section 5.4 to characterise the state produced by the source.

Purity

The simplest scalar figure of merit that quantifies how mixed a state is follows directly from the eigenvalues [1]:

$$\mathcal{P}(\hat{\rho}) = \mathrm{Tr}(\hat{\rho}^2) = \sum_i \lambda_i^2 \in \left[\tfrac{1}{4}, 1\right]. \tag{3.13}$$

$\mathcal{P} = 1$ for a pure state and $\mathcal{P} = 1/4$ for the completely mixed state $\hat{\rho} = \mathbb{I}/4$. For a maximally entangled state, $\mathcal{P} = 1$ since Bell states are pure. In practice, however, noise and decoherence drive the reconstructed state towards lower purity.

To measure the degree of entanglement that a system has, we use a full set of entanglement metrics — concurrence, negativity, formation entropy, fidelity and the Werner mixing parameter — is defined and computed in Section 3.7.

3.3 Spontaneous Parametric Down-Conversion

In this work, the entangled photon pairs are generated by *Spontaneous Parametric Down-Conversion* (SPDC), a nonlinear optical process that takes place inside the EPPS source. In SPDC, a high-frequency pump photon is probabilistically converted into two lower-frequency photons through a nonlinear crystal [4]. The crystal does not absorb the pump energy: the $\chi^{(2)}$ susceptibility of the medium couples the pump field to two new modes — called *signal* and *idler* — and transfers the energy and momentum of the pump photon into the generated pair. The process is spontaneous and probabilistic: typically only around 1 in 10^{10} pump photons produces a pair [4], making SPDC an intrinsically low-rate but highly pure source of photon pairs.

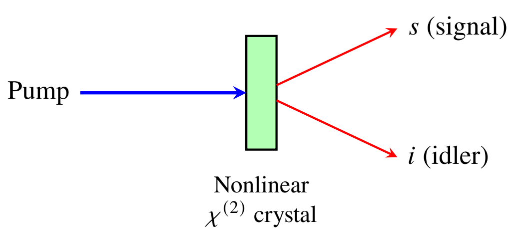

Figure 5: Schematic of the SPDC process inside the EPPS source. A pump photon enters the nonlinear crystal and is converted into two lower-frequency photons, signal (s) and idler (i).

3.3.1 Conservation laws and phase matching

The generation of each pair is governed by two conservation laws. Energy conservation requires

$$\omega_p = \omega_s + \omega_i, \tag{3.14}$$

and momentum conservation (the phase-matching condition) requires

$$\mathbf{k}_p = \mathbf{k}_s + \mathbf{k}_i, \tag{3.15}$$

or, more generally, in a periodically poled crystal under *quasi-phase-matching* (QPM),

$$\mathbf{k}_p = \mathbf{k}_s + \mathbf{k}_i + \mathbf{G}, \qquad \mathbf{G} = \frac{2\pi}{\Lambda}\hat{z}, \tag{3.16}$$

where Λ is the poling period and $\mathbf{G}$ is the reciprocal lattice vector it introduces along the propagation direction. QPM relaxes the strict birefringent phase-matching condition of Eq. (3.15) by compensating the momentum mismatch $\Delta k = k_p - k_s - k_i$ with $\mathbf{G}$, so that phase matching depends on the poling period instead of only on the crystal's natural birefringence [14].

where ω and $\mathbf{k}$ are the angular frequency and wave vector of the pump (p), signal (s) and idler (i) photons, respectively. These two conditions determine which frequencies and directions can be generated, and must be specifically designed by controlling the orientation of the crystal, the temperature or the periodic polarization.

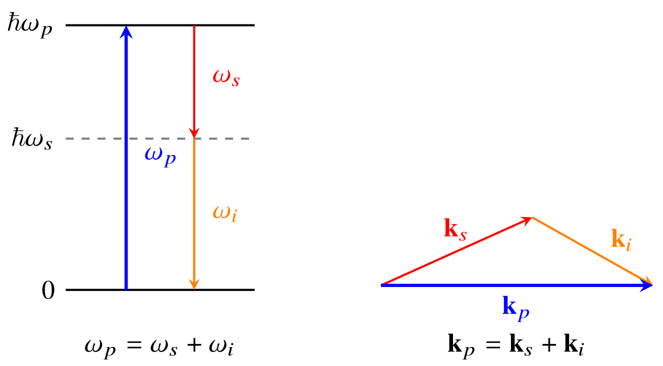

Figure 6: Conservation laws governing the SPDC process. *Left:* energy conservation — the pump photon energy $\hbar\omega_p$ is split into $\hbar\omega_s$ and $\hbar\omega_i$. *Right:* momentum conservation (phase-matching condition) — the pump wave vector $\mathbf{k}_p$ equals the vector sum of signal and idler wave vectors.

In this experiment the pump is at 660 nm and the down-converted photons are produced near 1320 nm [15].

3.3.2 Types of SPDC

SPDC processes are classified by the polarisation relationships between pump, signal and idler photons, as summarised in Table 7.

Table 7: Classification of SPDC processes by polarisation. H: horizontal; V: vertical.

Type	Signal	Idler	Pump
Type-0	H	H	H
Type-I	H	H	V
Type-II	H	V	$any(orthogonal pair)^*$

In Type-II phase matching, the pump must be oriented between the crystal's ordinary and extraordinary axes (typically at 45°), so that it drives both down-conversion processes at once, producing signal and idler with fixed, mutually orthogonal polarizations (H/V) independently of the exact pump polarization, as long as it is not aligned with either axis.

In Type-II SPDC, signal and idler are produced with orthogonal polarisations. This is the configuration used to generate polarisation-entangled photon pairs directly, without the need for an external interferometer [4].

3.3.3 The EPPS source.

The entangled photon pair source used in this experiment is the S-Fifteen EPPS-O [15]. According to its datasheet, the source generates polarisation-entangled photons at 1320 nm via SPDC in a Periodically Poled Potassium Titanyl Phosphate (PPKTP) crystal, driven by an integrated 660 nm pump laser. The photon pair rate exceeds 5×10^5 pairs/s and the polarisation-entanglement visibility is $> 96\%$. The spectrally non-degenerate photons of each pair are separated by a Wavelength Division Multiplexing (WDM) multiplexer, which routes signal and idler into two distinct output fibers.

The datasheet confirms the use of a PPKTP crystal but does not specify the phase-matching type. PPKTP is the standard crystal for Type-II polarisation-entangled SPDC sources [4, 9]: under Type-II quasi-phase-matching, signal and idler photons acquire orthogonal polarisations, and the output state can take the form

$$|\psi\rangle = \frac{1}{\sqrt{2}}\big(|H\rangle_A |V\rangle_B + e^{i\varphi} |V\rangle_A |H\rangle_B\big), \tag{3.17}$$

where φ is the relative phase determined by the crystal and pump conditions. For $\varphi = 0$ this is the Bell state $|\Psi^+\rangle$; for $\varphi = \pi$ it is $|\Psi^-\rangle$. It should be noted that Eq. (3.17) describes the *ideal output of the crystal*. By the time the photons reach the measuring device, they have propagated through optical fibers that apply an unknown unitary transformation, and the actual state recovered by QST may differ from $|\psi\rangle$ in Eq. (3.17). The characterisation of the measured state is the subject of Section 5.1 and Chapter 5.

3.4 Single-photon detection

Detecting individual photons is one of the key challenges in our project and in any quantum optics experiment. Unlike classical light measurements, where many photons are needed to a measurable current, QST and coincidence analysis require resolving single detection events with picosecond timing accuracy. This section describes the physical principles of single-photon detection and the specific detector that we used in this experiment.

Fundamental detector characteristics

Any photodetector is characterised by three fundamental parameters [16]:

Quantum efficiency (η): Probability that an incoming photon produces a measurable electrical signal. It depends on the detector material, geometry and the photon wavelength. A perfect detector would have $\eta = 1$; real devices rarely reach this ideal.

Dark noise: Photodetectors typically produce some level of signal even in the absence of light. In single-photon detectors, dark noise manifests as false clicks — called *dark counts* — generated by thermal excitation of charge carriers. The *DCR* (dark counts rate) quantifies this background noise. To reduce it, single-photon detectors are typically cooled.

Dead time (τ_d): The time the detector takes to recover after each detection event before it can be exited again (register another photon). During this window the detector is blind: any photon arriving within τ_d of a previous detection is lost. The maximum measurable count rate is therefore limited to $\sim 1/\tau_d$.

From APD to SPAD: Geiger-mode operation

In Geiger-mode operation, a single absorbed photon triggers a self-sustaining avalanche of charge carriers through the following process [16]:

1. The incoming photon is absorbed and promotes a valence electron into the conduction band, creating an electron–hole pair.
2. The large internal electric field accelerates this electron to extreme kinetic energies.
3. Moving at high speed, this electron strikes neighbouring atoms and frees additional electrons.
4. Each liberated electron is itself accelerated and ionises further atoms, producing a macroscopic, self-sustaining current pulse.

The resulting pulse is large enough to be detected by standard electronics, even though it originated from a single photon. An APD operated in Geiger mode is called a SPAD — Single Photon Avalanche Diode. After each avalanche, an active quenching circuit cuts the bias voltage below breakdown to stop the cascade and reset the detector, defining the dead time τ_d.

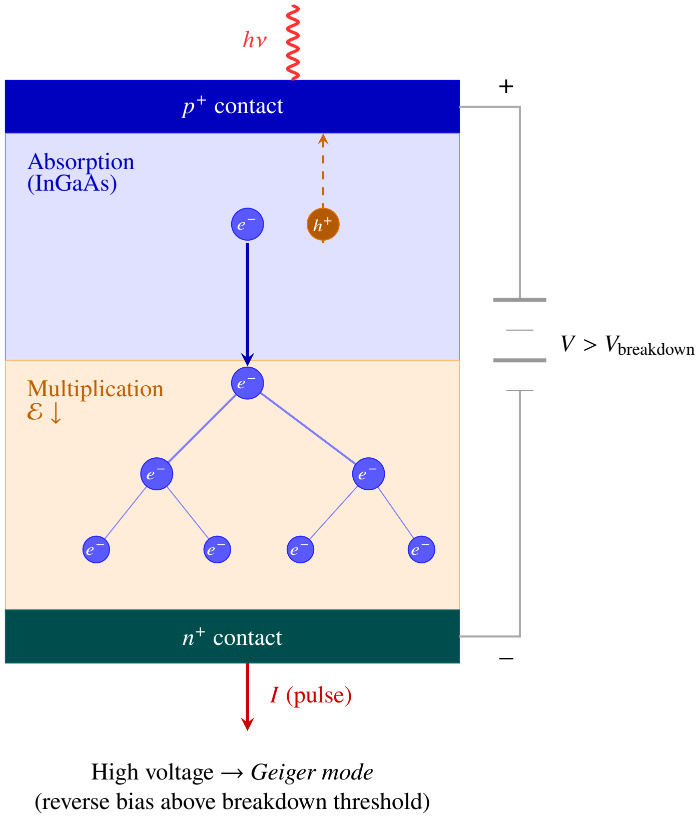

Figure 7: Cross-section of a SPAD in Geiger mode. A photon $h\nu$ is absorbed in the InGaAs layer, creating an electron–hole pair. The hole (h^+) drifts toward the p^+ contact while the electron (e^-) enters the high-field multiplication region, triggering an impact-ionisation avalanche ($1 \to 2 \to 4$ electrons) that produces a macroscopic current pulse I [16].

The MPD PDM-IR detector

Standard silicon SPADs have good efficiency in the visible range (up to $\sim 70\%$ at 650 nm) but are nearly blind at 1320 nm, where silicon's absorption drops to $\lesssim 2\%$. Since the photons produced by the EPPS source are centred at 1320 nm, the experiment requires a different semiconductor material.

The detectors used in this work are the **MPD PDM-IR** modules [17]: fiber-coupled SPADs based on an **InGaAs/InP** junction, which is sensitive from 900 nm to 1700 nm. The key specifications relevant to this experiment are listed in Table 8.

Table 8: Key specifications of the MPD PDM-IR detector [17]. η: Photon Detection Efficiency; DCR: Dark Count Rate; FWHM: Full Width at Half Maximum.

Parameter	Value	Condition
Spectral range	900–1700 nm	—
η (peak)	up to 30%	$V_{EX} = 7\,V$, $\lambda = 1550\,nm$
Timing jitter (FWHM)	as low as 80 ps	$V_{EX} = 7\,V$
DCR (min)	300 c/s	free-running, low temperature
SPAD temperature	225–243 K	Peltier-cooled
Hold-off (dead) time	1 µs–3 ms	software-selectable

The SPAD is cooled by an integrated Peltier element to reduce thermal excitation and minimise the DCR. The detector operates in free-running mode for this experiment, meaning it remains active continuously and registers every avalanche event as a timestamped pulse.

Dark counts and afterpulsing

Two noise mechanisms affect the measurement: DCR produces background clicks at a constant average rate, and *afterpulsing* generates spurious secondary pulses shortly after a real detection, caused by charges temporarily trapped in the semiconductor lattice during an avalanche.

In the experiment, dark counts are subtracted from the coincidence measurement following the characterisation procedure described in Section 5.1. Because the DCR results from a large number of independent thermal events summed over the integration window, the CLT guarantees that its distribution over repeated measurements converges to a Gaussian — a property exploited in the dark-count subtraction protocol of Section 5.1.

3.5 Polarization Mode Dispersion and decoherence

Distributing entangled photons through optical fiber is the central challenge in our project. Even if the SPDC source generates a pair of photons in a maximally entangled state (Section 3.3), the fiber that carries them to the measurement devices can partially or completely destroy that entanglement. The physical mechanism responsible is the polarization mode dispersion *PMD*: the dependence of the phase velocity on the polarisation of the photon. For a broadband photon source such as our EPPS, PMD had quite a significant impact, because the PMD is different for distinct frequencies, and understanding that it was essential for diagnosing and resolving the degradation observed in the first measurements (Section 5.2.2).

Standard single-mode fiber (SMF)

A standard single-mode fiber (SMF) is nominally cylindrically symmetric, but manufacturing imperfections, mechanical stress, and temperature gradients introduce a small random birefringence that varies along the fiber length. As a result, the polarisation state of a photon propagating through SMF evolves unpredictably: a photon entering as $|H\rangle$ may exit in any polarisation. Mathematically, the fiber acts as a general 2×2 unitary Jones matrix [13]

$$U = \begin{pmatrix} \alpha & -\beta^* \\ \beta & \alpha^* \end{pmatrix}, \qquad |\alpha|^2 + |\beta|^2 = 1 \quad \text{(unitarity condition)}, \tag{3.18}$$

which preserves the norm of the polarisation vector ($\|U\,|\psi\rangle\| = \||\psi\rangle\|$) but rotates it in an uncontrolled way. The key property of SMF is that, while the polarisation direction is unpredictable, the two polarisation components travel at nearly the same group velocity: the residual birefringence is small ($\Delta n_{\mathrm{SMF}} \sim 10^{-7}$–$10^{-6}$).

Polarization-maintaining fiber (PM)

A PM fiber is designed to have very high internal birefringence by incorporating stress rods inside the cladding, creating two well-defined polarisation axes: the *fast axis* (lower refractive index n_f, higher phase velocity) and the *slow axis* (higher refractive index $n_s > n_f$, lower phase velocity). The birefringence of a typical PM fiber is of the order $\Delta n = n_s - n_f \sim 4\times10^{-4}$ [18], approximately three orders of magnitude larger than the residual birefringence of SMF ($\Delta n_{\mathrm{res}} \sim 10^{-6}$).

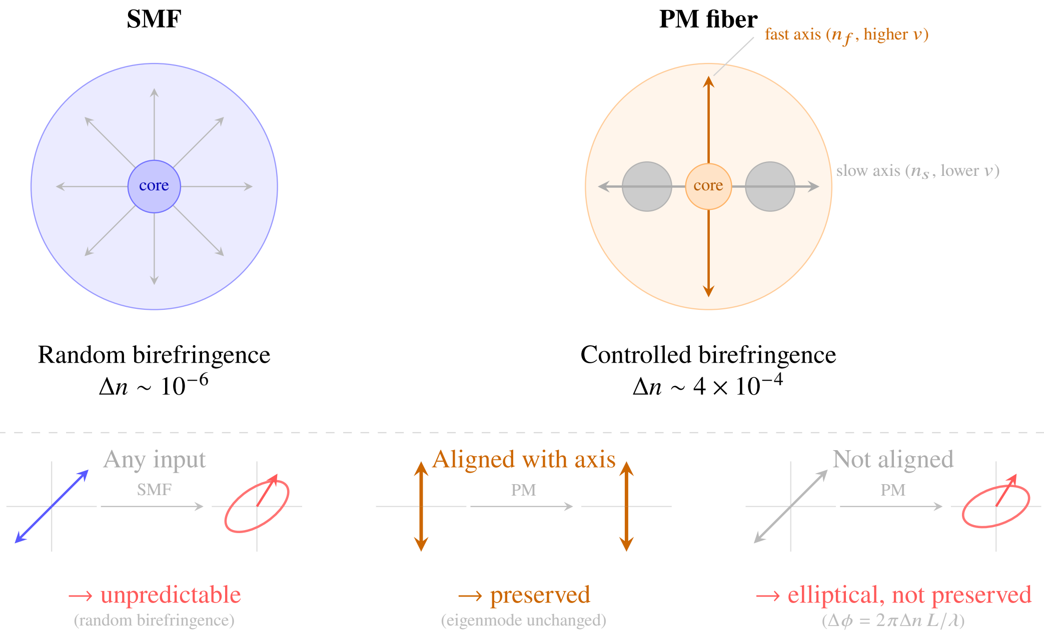

Figure 8: Cross-sections and polarisation behaviour of SMF (left) and PM fiber (right). In SMF, random residual birefringence rotates the polarisation unpredictably for any input. In PM fiber, a photon aligned with either principal axis maintains its polarisation state. If the input is not aligned, its components along the fast and slow axes travel at different speeds and accumulate a differential phase $\Delta\phi = 2\pi\,\Delta n\,L/\lambda$; the output polarisation is in general elliptical and the input state is not preserved.

When a photon is aligned with one of the PM fiber axes, its polarisation is preserved — but if it is not perfectly aligned, the two components develop independently. The Jones matrix of a PM fiber is diagonal [13]:

$$M_{\mathrm{PM}} = \begin{pmatrix} e^{i\phi_H} & 0 \\ 0 & e^{i\phi_V} \end{pmatrix}, \qquad \phi_{H,V} = \frac{n_{H,V}\,\omega\,L}{c}, \tag{3.19}$$

where L is the fiber length. The off-diagonal zeros reflect the key property of PM fiber: there is no mixing between axes, the fiber does not “mix the states”, but is decomposed in time and phase

The relative phase accumulated between the two components is $\Delta\phi = \phi_V - \phi_H = 2\pi\,\Delta n\,L/\lambda$, and the distance over which $\Delta\phi$ completes a full 2π cycle is the *beat length*:

$$L_b = \frac{\lambda}{\Delta n}. \tag{3.20}$$

Differential group delay and PMD

This differential phase arises because the two polarisation components travel at different *group velocities*:

$$v_{g,H} = \frac{c}{n_H}, \qquad v_{g,V} = \frac{c}{n_V}. \tag{3.21}$$

After propagating a length L, the H and V components of the same photon arrive at different times. The *differential group delay* is [9]

$$\Delta\tau = L\,\frac{n_H - n_V}{c} = \frac{\Delta n\,L}{c}. \tag{3.22}$$

This temporal differential group delay is the PMD.

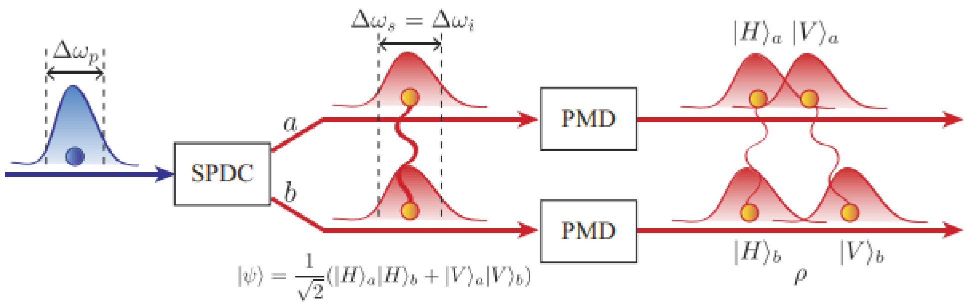

Figure 9: Illustration of the PMD differential group delay effect on a broadband polarisation-entangled photon pair distributed through two independent fiber channels a and b. The birefringence of each channel separates the $|H\rangle$ and $|V\rangle$ polarisation components of each photon in time by a differential group delay $\Delta\tau = \Delta n\,L/c$. Since the two channels may carry different fiber lengths ($L_1 \neq L_2$), the differential group delay experienced by each photon can differ, producing an asymmetric entanglement degradation. Reprinted from Lim *et al.* [9] under CC BY 4.0.

Effect on broadband entangled photons

The PM fiber acts as a *frequency-dependent wave plate*: for each angular frequency component ω of the photon, the Jones matrix $U_{\mathrm{PM}}(\omega)$ applies a differential phase $\Delta\phi(\omega) = \Delta\tau \cdot \omega$ between the $|H\rangle$ and $|V\rangle$ modes. For a narrowband source, all frequency components accumulate nearly the same phase, and the polarisation transformation is well defined. For the broadband EPPS source, however, $\Delta\phi(\omega)$ varies significantly across the spectrum: each wavelength component leaves the fiber with a *different* polarisation state. Since single-photon detectors cannot differentiate wavelength, what is detected is an average over all these differently-transformed polarisation states, and the measured coincidences no longer correspond to any well-defined polarisation projection. This is the fundamental reason why the first measurements performed with PM fiber yielded a near-maximally mixed state, as discussed in Section 5.2.1.

Because PM fiber has a fixed, well-defined birefringent axis, this effect can be quantified directly using the diagonal Jones matrix of Eq. (3.19): a full numerical simulation of the resulting two-photon density matrix, integrated over the source spectrum, is presented in Section 5.2.2. SMF does not admit the same treatment, for the reason developed below.

Numerical estimate for the experimental setup

The residual birefringence of standard single-mode fiber (SMF-28) can be estimated directly from its PMD specification. According to the Corning SMF-28 Ultra product datasheet [19], the maximum individual fiber PMD coefficient is PMD ≤ 0.1 ps/$\sqrt{\text{km}}$, defined such that the differential group delay accumulated over a length L is $\Delta\tau = \text{PMD} \cdot \sqrt{L}$. Substituting into Eq. (3.22), $\Delta\tau = \Delta n \cdot L/c$, and solving for Δn:

$$\Delta n = \frac{\Delta\tau \cdot c}{L} = \frac{\text{PMD} \cdot c}{\sqrt{L}}. \tag{3.23}$$

For the short SMF patch cords used in the experimental setup — estimated at $L \approx 2$–3 m — this gives $\Delta n_{\text{SMF}} \approx 5 \times 10^{-7}$, three orders of magnitude smaller than $\Delta n_{\text{PM}} \approx 4 \times 10^{-4}$. This value, however, cannot simply be substituted into the fixed-axis model of Eq. (3.19): unlike PM fiber, SMF does not have a single well-defined birefringent axis along its length, since manufacturing imperfections, bending, and temperature gradients cause its orientation to vary randomly from point to point. A more general treatment would replace the fixed-axis Jones matrix of Eq. (3.19) by a general SU(2) parametrization of the birefringent fiber [20]:

$$U(\theta, \phi, \chi) = \begin{pmatrix} \cos\theta\, e^{i\phi} & -\sin\theta\, e^{i\chi} \\ \sin\theta\, e^{-i\chi} & \cos\theta\, e^{-i\phi} \end{pmatrix}, \qquad \theta \in \left[0, \tfrac{\pi}{2}\right], \quad \phi, \chi \in [0, 2\pi), \tag{3.24}$$

where θ sets the relative weight of the two polarization components and ϕ, χ are phase parameters describing the orientation of the birefringent axis. The fixed-axis model of Eq. (3.19) corresponds to the particular case $\theta = 0$, where U reduces to a diagonal matrix and the birefringent axis is aligned with the $\{H, V\}$ basis. For SMF, θ is not fixed but varies randomly along the fiber; a precise model would therefore treat the fiber as a concatenation of many short segments, each described by Eq. (3.24) with its own random θ_i, so that the net transformation no longer accumulates coherently in a single basis as it does for PM fiber. This is the qualitative reason why SMF preserves entanglement far better than its raw birefringence value alone would suggest, even though setting up and validating this segment-by-segment model goes beyond the scope of this work.

3.6 Quantum State Tomography

The problem of characterizing a quantum state

Unlike a classical object, whose properties can be probed repeatedly without disturbing them, a quantum system is irrevocably altered by the act of measurement. A single projective measurement on a single copy of an unknown state $\hat{\rho}$ collapses it onto an eigenstate of the observable being measured, and therefore returns only one bit of information about the original state. The full density matrix $\hat{\rho}$ contains, for a two-qubit system, fifteen independent real parameters[1], so a single measurement is dramatically insufficient to recover it.

Quantum State Tomography (QST) is the experimental procedure designed to overcome this fundamental limitation. The strategy is to prepare a large number of identical copies of the state and to perform a collection of projective measurements in different, mutually incompatible bases. Each configuration provides a partial view of $\hat{\rho}$ that, taken in isolation, is incomplete; combined statistically, however, the set of measurement outcomes is sufficient to reconstruct the full density matrix [10, 11, 1].

Origin of the name and classical analogy

The term *tomography* derives from the Greek word *tomos* ('section', 'slice') and reflects a direct conceptual analogy with its classical equivalent. In medical computed-tomography (CT) imaging, a three-dimensional object is reconstructed from a series of two-dimensional projections taken at different angles around it. Quantum tomography proceeds in exactly the same spirit: each measurement basis plays the role of one viewing angle, and the density matrix is the multidimensional 'object' that emerges once enough projections have been combined [11]. You can think of it as *photographing the quantum state from* 36 *different angles*, where each 'photograph' is the coincidence count obtained for one of the 36 polarization projections.

Why QST

Quantum state tomography has become an essential tool in the development of quantum technologies. Whenever an unknown quantum state must be *verified*, *characterized* or *benchmarked*, QST is the most suitable method. Its main applications include:

- **Source certification.** Verifying the fidelity of an entangled photon source against an ideal Bell state—a prerequisite for any quantum-communication protocol.
- **Quantum-computation benchmarking.** Reconstructing the output of a logical gate to evaluate its performance and error budget [1].
- **Diagnosis of decoherence.** Quantifying how much coherence (off-diagonal elements of $\hat{\rho}$) is lost when a state propagates through a noisy channel, by tracking figures of merit such as purity $\mathrm{Tr}(\hat{\rho}^2)$, concurrence $C(\hat{\rho})$ or fidelity with a target state.

It is precisely this first role that motivates the use of QST in the present work. Rather than being an end in itself, the tomographic reconstruction of $\hat{\rho}$ is here employed as a *diagnostic instrument* to evaluate the quality of the entangled two-photon state produced by the EPPS source and, more importantly, to quantify the decoherence introduced by the propagation channel. As shown in Lim *et al.* [9] for broadband SPDC sources analogous to the one used in this work, polarization mode dispersion in optical fibers acts as an effective decoherence mechanism. In this thesis, that mechanism is not modelled quantitatively as in Lim *et al.*, but diagnosed through the loss of purity

[1] A general 4×4 Hermitian matrix has 16 real parameters; the trace-unit constraint $\mathrm{Tr}(\hat{\rho}) = 1$ removes one of them.

revealed by the tomographic reconstruction of $\hat{\rho}$. This diagnostic use of QST constitutes one of the central threads of the experimental work presented in Chapter 5.

Outline of the QST procedure followed in this work

The reconstruction protocol implemented in this thesis closely follows the formalism of James *et al.* [10] and Altepeter–James–Kwiat [11], and is developed in detail in the subsections that follow:

- Section 3.6.1 introduces the measurement projectors $\hat{\Pi}_k$ (built from the six polarization states H, V, D, A, R, L via tensor products) and the Pauli operator basis $\{\hat{T}_j\}_{j=1}^{16}$ used to expand the two-qubit density matrix.
- Section 3.6.2 formulates the tomographic problem as the linear system $\vec{n} = N\,A\,\vec{t}$, derives the design matrix $A_{k,j} = \frac{1}{4}\,\mathrm{Tr}(\hat{T}_j\,\hat{\Pi}_k)$, and presents the Moore–Penrose pseudoinverse as a first, fast (but not necessarily physical) reconstruction.
- Section 3.6.3 introduces the Maximum-Likelihood Estimation (MLE) refinement with the Cholesky parametrization of $\hat{\rho}$, which guarantees by construction that the reconstructed matrix is Hermitian, positive semidefinite and of unit trace—i.e., a valid physical density matrix.

Throughout this section the following notation is used: n_k denotes the experimental net coincidence count for the k-th measurement configuration ($k = 1, \ldots, 36$); μ_k denotes the expected (Poisson-mean) count predicted by a candidate density matrix; N denotes the total number of photon pairs emitted by the source per acquisition window, used as a global normalisation constant; the operator-basis index j runs from 1 to 16, labelling each of the sixteen tensor products $\hat{T}_j = \hat{\sigma}_a \otimes \hat{\sigma}_b$ with $a, b \in \{0, 1, 2, 3\}$.

3.6.1 Projectors and the Pauli operator basis

The reconstruction begins with what the laboratory actually delivers. For each of the 36 measurement configurations described in Section 4.4, the raw counts recorded by the time-tagger are taken and the dark-count background is subtracted, leaving a single net coincidence count per configuration. Stacking these counts gives a column vector of 36 real entries,

$$\vec{n} = (n_1,\; n_2,\; \ldots,\; n_{36})^T, \tag{3.25}$$

where n_k is the net coincidence count for the k-th configuration (e.g. $|H\rangle\,|H\rangle, |D\rangle\,|A\rangle, |R\rangle\,|V\rangle, \ldots$). Each n_k is proportional to the probability that the two-photon state projects onto that configuration. The whole point of the next steps is to translate this vector of 36 numbers into the 16 entries of the density matrix $\hat{\rho}$.

Projectors

The probability that a state $\hat{\rho}$ collapses onto a given measurement outcome is given by the Born rule:

$$P = \mathrm{Tr}(\hat{\Pi}\,\hat{\rho}), \tag{3.26}$$

where $\hat{\Pi}$ is the projector associated with the measurement. For a single photon, $\hat{\Pi}_H = |H\rangle\langle H|$ selects horizontal polarization, $\hat{\Pi}_V = |V\rangle\langle V|$ the vertical one, and so on for the diagonal (D, A) and circular (R, L) bases. For a two-photon system the joint projector is the tensor product of the two single-photon projectors; the projector that selects $|H\rangle|V\rangle$ is, for example,

$$\hat{\Pi}_{HV} = |H\rangle\langle H| \otimes |V\rangle\langle V|\,. \tag{3.27}$$

The full set of 36 projectors $\{\hat{\Pi}_k\}_{k=1}^{36}$ is built by combining the six single-photon polarizations H, V, D, A, R, L on each arm, giving $6 \times 6 = 36$ joint configurations.

Pauli matrices as a basis

For a single qubit (a 2-dimensional system), the four Pauli matrices form a complete basis for Hermitian operators: any 2×2 Hermitian matrix can be written as a linear combination of $\hat{\sigma}_0$, $\hat{\sigma}_1$, $\hat{\sigma}_2$ and $\hat{\sigma}_3$:

$$\hat{\sigma}_0 = \begin{pmatrix} 1 & 0 \\ 0 & 1 \end{pmatrix}, \quad \hat{\sigma}_1 = \begin{pmatrix} 0 & 1 \\ 1 & 0 \end{pmatrix}, \quad \hat{\sigma}_2 = \begin{pmatrix} 0 & -i \\ i & 0 \end{pmatrix}, \quad \hat{\sigma}_3 = \begin{pmatrix} 1 & 0 \\ 0 & -1 \end{pmatrix}. \tag{3.28}$$

Each has a direct physical meaning in this experiment:

- $\hat{\sigma}_3 \longrightarrow H/V$ **basis:** $\hat{\sigma}_3 = |H\rangle\langle H| - |V\rangle\langle V|$. Its expectation value answers the question "are there more horizontal or vertical photons?": $\langle\hat{\sigma}_3\rangle = +1$ means a fully horizontal photon, -1 fully vertical, and 0 a tie (diagonal or circular).
- $\hat{\sigma}_1 \longrightarrow D/A$ **basis:** $\hat{\sigma}_1 = |D\rangle\langle D| - |A\rangle\langle A|$.
- $\hat{\sigma}_2 \longrightarrow R/L$ **basis:** $\hat{\sigma}_2 = |R\rangle\langle R| - |L\rangle\langle L|$.
- $\hat{\sigma}_0 \longrightarrow$ **total intensity:** $\hat{\sigma}_0 = |H\rangle\langle H| + |V\rangle\langle V|$. This operator does not filter anything. It represents the total probability of finding the photon regardless of polarization; its expectation value is always 1 for any normalized state.

For two photons, instead of 4 single-qubit Paulis there are 16 two-qubit operators, each built as the tensor product of two single-qubit Paulis:

$$\hat{T}_j = \hat{\sigma}_a \otimes \hat{\sigma}_b, \qquad a, b \in \{0, 1, 2, 3\}, \tag{3.29}$$

indexed from $\hat{T}_1 = \hat{\sigma}_0 \otimes \hat{\sigma}_0$ to $\hat{T}_{16} = \hat{\sigma}_3 \otimes \hat{\sigma}_3$. These 16 operators span the space of 4×4 Hermitian matrices, which is exactly the space in which $\hat{\rho}$ lives.

Worked example

Expanding $\hat{T} = \hat{\sigma}_3 \otimes \hat{\sigma}_3$ explicitly:

$$\begin{aligned}\hat{T} &= \hat{\sigma}_3 \otimes \hat{\sigma}_3 = \big(|H\rangle\langle H| - |V\rangle\langle V|\big) \otimes \big(|H\rangle\langle H| - |V\rangle\langle V|\big) \\ &= |HH\rangle\langle HH| + |VV\rangle\langle VV| - \big(|HV\rangle\langle HV| + |VH\rangle\langle VH|\big). \end{aligned} \tag{3.30}$$

Expansion of the density matrix

We can parametrize any density matrix (4 single-qubit) as a linear combination of the 16 operators $\hat{T}_j$:

$$\hat{\rho} = \frac{1}{4}\sum_{j=1}^{16} t_j \hat{T}_j, \tag{3.31}$$

where the coefficients t_j are the unknowns of the tomographic problem. The factor $1/4$ normalizes the expansion so that $\mathrm{Tr}(\hat{\rho}) = 1$. Each t_j acts as a weighting coefficient, physically representing the expectation value of the corresponding operator $\hat{T}_j$.

$$t_j = \mathrm{Tr}(\hat{\rho}\,\hat{T}_j), \tag{3.32}$$

3.6.2 Design matrix and Moore–Penrose pseudoinverse

From Eq. (3.26) we can determine the probability of obtaining the outcome associated with projector $\hat{\Pi}_k$:

$$P_k = \mathrm{Tr}(\hat{\rho}\,\hat{\Pi}_k). \tag{3.33}$$

In the laboratory, however, what is measured is not a probability but a number of coincidences – typically a few thousand counts. To compare them with the model, the experimental counts n_k must be normalized by the total number of photon pairs N emitted by the source during the acquisition window,

$$n_{\mathrm{norm},k} = \frac{n_k}{N}, \tag{3.34}$$

so that the connection between data and theory takes the form $n_{\mathrm{norm},k} = \mathrm{Tr}(\hat{\rho}\,\hat{\Pi}_k)$.

Construction of the design matrix

When we have an overdetermined system (more samples than unknowns), we need to construct a design matrix to obtain a best-fit solution.

Substituting the expansion $\hat{\rho} = \frac{1}{4}\sum_j t_j \hat{T}_j$ into the equation above and using the linearity of the trace:

$$n_k = \mathrm{Tr}\left[\frac{1}{4}\sum_{j=1}^{16} t_j \hat{T}_j \cdot \hat{\Pi}_k\right] = \sum_{j=1}^{16} t_j \underbrace{\frac{1}{4}\mathrm{Tr}(\hat{T}_j\,\hat{\Pi}_k)}_{A_{k,j}}. \tag{3.35}$$

The bracketed values are the (k, j) entry of the *design matrix* A:

$$\boxed{A_{k,j} = \frac{1}{4}\,\mathrm{Tr}(\hat{T}_j\,\hat{\Pi}_k),} \tag{3.36}$$

so the entire tomographic problem reduces to the linear system

$$\boxed{A\,\vec{t} = \vec{n},} \tag{3.37}$$

where A has dimensions 36×16 (one row per measurement, one column per operator basis element), $\vec{t}$ is the column vector of 16 unknown coefficients, and $\vec{n}$ is the column vector of 36 normalized experimental counts:

$$\underbrace{\begin{pmatrix} A_{1,1} & \cdots & A_{1,16} \\ \vdots & \ddots & \vdots \\ A_{36,1} & \cdots & A_{36,16} \end{pmatrix}}_{A\ (36\times16)} \underbrace{\begin{pmatrix} t_1 \\ \vdots \\ t_{16} \end{pmatrix}}_{\vec{t}} = \underbrace{\begin{pmatrix} n_1 \\ \vdots \\ n_{36} \end{pmatrix}}_{\vec{n}}. \tag{3.38}$$

The system has mathematically 16 unknowns, so 16 well-chosen projective measurements would be sufficient to determine $\hat{\rho}$. Nevertheless, in the laboratory, many variables and noise sources are difficult to eliminate entirely. Thus, the choice of 36 measurements is mainly motivated by redundancy: the overdetermined system mitigates the effect of statistical noise on the reconstructed matrix. As an additional check, Chapter 5 also reports a reduced reconstruction using only 16 measurements, allowing a comparison between both approaches.

With 36 equations and 16 unknowns, there is no exact solution that passes through every data point, due to the noise in the measurements. The standard approach is the Moore–Penrose pseudoinverse A^+, which finds the vector $\vec{t}$ that minimizes the squared error between $A\vec{t}$ and $\vec{n}$. Conceptually, it works like fitting a trend line, but in 16 dimensions.

The derivation follows from requiring that $A\vec{t} - \vec{n}$ be orthogonal to the column space of A:

$$A\,\vec{t} = \vec{n} \;\Rightarrow\; A^T(A\,\vec{t} - \vec{n}) = \vec{0} \;\Rightarrow\; A^T A\,\vec{t} = A^T\vec{n}, \tag{3.39}$$

so that, provided A^TA is invertible (which holds for any well-chosen tomographic protocol, since the projectors are linearly independent),

$$\boxed{\vec{t}_{\mathrm{opt}} = (A^TA)^{-1}A^T\vec{n}.} \tag{3.40}$$

Once $\vec{t}_{\mathrm{opt}}$ is known, the density matrix is recovered by substituting it back into the expansion,

$$\hat{\rho} = \frac{1}{4}\sum_{j=1}^{16} t_j\,\hat{T}_j. \tag{3.41}$$

The diagonal entries of the reconstructed matrix correspond to *populations* – the probability of finding the system in each of the four computational-basis configurations $|HH\rangle$, $|HV\rangle$, $|VH\rangle$, $|VV\rangle$

– while the off-diagonal entries are *coherences*, encoding the quantum superposition between the basis states.

Limitation of the pseudoinverse

Although it is fast and numerically stable, the pseudoinverse has one important drawback: the matrix it returns is not guaranteed to be a physical density matrix. Statistical noise can cause the reconstructed $\hat{\rho}$ to fall outside the set of valid quantum states – for instance, producing small negative eigenvalues that violate positive semidefiniteness. This is a known limitation of any linear inversion method [10, 11], and it motivates the refined reconstruction described in the next subsection.

3.6.3 Maximum-Likelihood Estimation with Cholesky parametrization

The pseudoinverse gives the matrix that best fits the data in a least-squares sense, but it does not enforce the three physical conditions that any density matrix must satisfy: Hermiticity, Positive eigenvalues (Positive Semi-Definite matrix), and unit trace. To recover a matrix that is both close to the data and physically valid, the protocol used here applies a second step based on Maximum-Likelihood Estimation (MLE).

Cholesky parametrization

The key idea, due to James, Kwiat, Munro and White [10], is that the optimizer does not search directly for $\hat{\rho}$. Instead, it searches over the parameters of a lower-triangular complex matrix T – the Cholesky factor – and reconstructs the density matrix as:

$$\boxed{\hat{\rho} = \frac{T^\dagger T}{\mathrm{Tr}(T^\dagger T)},} \tag{3.42}$$

where T has the explicit form

$$T = \begin{pmatrix} t_1 & 0 & 0 & 0 \\ t_5 + i\,t_6 & t_2 & 0 & 0 \\ t_{11} + i\,t_{12} & t_7 + i\,t_8 & t_3 & 0 \\ t_{15} + i\,t_{16} & t_{13} + i\,t_{14} & t_9 + i\,t_{10} & t_4 \end{pmatrix}, \tag{3.43}$$

with 16 real parameters: $t_1, \ldots, t_4$ on the diagonal and 6 complex entries below it. The construction guarantees that $T^\dagger T$ is automatically Hermitian and positive semidefinite, and dividing by $\mathrm{Tr}(T^\dagger T)$ enforces unit trace. The result is that $\hat{\rho}$ is a physically valid density matrix by construction, turning a constrained optimization problem into an unconstrained one.

Optimization loop

The MLE algorithm works iteratively:

1. The optimizer proposes a set of values for the parameters $\vec{t} = (t_1, t_2, \ldots, t_{16})$.
2. With those parameters, it builds the support matrix T and computes $\hat{\rho} = T^\dagger T \,/\, \mathrm{Tr}(T^\dagger T)$.

3. It evaluates how well the resulting $\hat{\rho}$ reproduces the experimental data by computing a cost function that quantifies the disagreement between the predicted counts $\mu_k(\hat{\rho})$ and the measured counts n_k.

4. The optimizer uses the gradient of that cost to update $\vec{t}$ and proposes a new candidate. The loop repeats until convergence.

The cost function is therefore the heart of the method: it determines what "best fit" means in a statistically rigorous sense.

Photon counting and the Poisson distribution

Single-photon avalanche detectors act as independent counters. The number of photons recorded in a fixed time window follows a Poisson distribution, which follows from three properties of the detection process:

- **Temporal independence.** The number of detections in one interval is statistically independent of the number in any disjoint interval.
- **Proportionality on infinitesimal intervals.** In an infinitesimally short window dt, the probability of exactly one detection event is $P(1 \text{ event in } dt) = \gamma\, dt$, where γ is the emission rate.
- **Exclusion of simultaneous events.** The probability of two or more events in dt is of higher order: $P(\geq 2 \text{ events in } dt) = O(dt^2) \approx 0$.

Under these conditions, for measurement configuration k the candidate density matrix predicts an expected count μ_k, and the probability of observing exactly n_k counts is

$$P(n_k \mid \mu_k) = \frac{\mu_k^{n_k}\, e^{-\mu_k}}{n_k!}, \qquad \mu_k = N\, \mathrm{Tr}(\hat{\rho}\, \hat{\Pi}_k), \tag{3.44}$$

where μ_k is the theoretical prediction and n_k is the experimental datum.

The likelihood function

The likelihood function for the full set of 36 measurements is the joint probability of observing the entire data vector under the candidate model:

$$\mathcal{L}(\hat{\rho}) = \prod_{k=1}^{36} \frac{\mu_k(\hat{\rho})^{n_k}\, e^{-\mu_k(\hat{\rho})}}{n_k!}. \tag{3.45}$$

$\mathcal{L}(\hat{\rho})$ is a scalar – the score the algorithm assigns to each candidate $\hat{\rho}$. The larger $\mathcal{L}$, the better that matrix fits the experimental data. The goal of MLE is to find the $\hat{\rho}$ that maximizes $\mathcal{L}$.

Maximizing a product of 36 terms is numerically unstable due to underflow. Since the maximum of $\ln \mathcal{L}$ coincides with that of $\mathcal{L}$, it is common practice to work with the natural logarithm instead:

$$\ln \mathcal{L} = \sum_{k=1}^{36} \Big[n_k \ln(\mu_k) - \mu_k - \ln(n_k!) \Big]. \tag{3.46}$$

In computational optimization (SciPy library), algorithms are designed to search for the minimum of a function rather than the maximum (as in gradient descent), so the sign is flipped. The term $\ln(n_k!)$ does not depend on $\hat{\rho}$, so its derivative with respect to the parameters is zero and can be dropped without moving the minimum. The cost function used in the implementation is therefore:

$$\boxed{f(\hat{\rho}) = \sum_{k=1}^{36} \Big[\mu_k(\hat{\rho}) - n_k \ln \mu_k(\hat{\rho}) \Big].} \tag{3.47}$$

This is the exact Poisson negative log-likelihood.

Connection with the Gaussian / χ^2 regime

The Central Limit Theorem (CLT) states that the sum of N independent and identically distributed random variables converges to a Gaussian as $N \to \infty$, regardless of the original distribution. In this experiment, the photon detections satisfy both conditions: they are independent (SPDC is memoryless) and identically distributed (the pump-laser power is constant). When the count rate is high ($\mu_k \to \infty$), the Poisson distribution converges to a Gaussian with mean μ_k and variance $\sigma_k^2 = \mu_k$. Substituting $\sigma^2 = \mu$ into the Gaussian log-likelihood and discarding the constant prefactor (whose derivative is zero), the cost simplifies to

$$f_{\chi^2} = \sum_{k=1}^{36} \frac{(n_k - \mu_k)^2}{2\,\mu_k}, \tag{3.48}$$

which is the χ^2-like cost used in the high-count, Gaussian regime. The structure is transparent: the numerator $(n_k - \mu_k)^2$ keeps the error positive regardless of its sign, while the denominator $2\mu_k$ increases the relative penalty for measurements with low expected counts.

Why exact Poisson and not Gaussian

In entanglement experiments, projections orthogonal to the natural state of the source – so-called "dark" projections – yield near-zero coincidence counts. In this low-count regime the CLT breaks down: with only a handful of counts per configuration, the distribution is far from Gaussian, and using f_{χ^2} would distort the reconstructed matrix, particularly in the off-diagonal coherences that are the most physically relevant entries. Only the exact Poisson cost behaves correctly across the full range from dark projections to bright ones, which is why it is the form used in this work.

3.7 Entanglement metrics

A 4×4 complex density matrix contains too much information to interpret directly, and the goal of the experiment is not to identify every element of $\hat{\rho}$ but to answer a concrete question: how much entanglement does the source actually produce?

Different metrics probe different aspects of the same state — some measure how mixed each photon is when the other is ignored, others detect entanglement through geometric properties of $\hat{\rho}$, and others compare the experimental state to a theoretical ideal. No single metric is sufficient on its own, precisely because entanglement itself is not reducible to a single number; taken together, the metrics introduced in the following subsections give a more complete picture of the state produced by the source.

The natural unit for all these metrics is the *ebit* (entanglement bit). One ebit is exactly the quantity of entanglement that contains a perfect Bell state: 1 ebit = entanglement of $|\Psi^+\rangle = \frac{1}{\sqrt{2}}(|HV\rangle + |VH\rangle)$. Just as one can say "this file is 4 MB", one can say "this state has 0.72 ebits of entanglement".

The metrics described in this section are organized into three families. All of them are computed from the experimental density matrices and reported in Section 5.4.

3.7.1 Family 1: Reduced-state metrics

These metrics start from the *reduced density matrix* of one photon, obtained by tracing out the other. The partial trace over photon B is:

$$\hat{\rho}_A = \mathrm{Tr}_B(\hat{\rho}) = \langle H|_B \, \hat{\rho} \, |H\rangle_B \; + \; \langle V|_B \, \hat{\rho} \, |V\rangle_B \,, \tag{3.49}$$

and gives a 2×2 matrix describing photon A alone, with photon B averaged out. The key physical point is this: in an entangled state, neither photon has a definite polarization of its own. The more entangled the pair, the more mixed $\hat{\rho}_A$ becomes — and that mixture is what the following metrics quantify.

Von Neumann entropy

The von Neumann entropy of $\hat{\rho}_A$ is

$$\boxed{S(\hat{\rho}_A) = -\,\mathrm{Tr}\big(\hat{\rho}_A \log_2 \hat{\rho}_A\big) = -\sum_i \lambda_i \log_2 \lambda_i,} \tag{3.50}$$

where λ_i are the eigenvalues of $\hat{\rho}_A$. It is the quantum extension of the Shannon entropy: Shannon (1948) defined $S_{\mathrm{Sh}} = -\sum_i p_i \log_2 p_i$ to measure the uncertainty in a classical probability distribution, and von Neumann replaced the classical probabilities p_i with the eigenvalues of the density matrix. Applied to $\hat{\rho}_A$, the entropy measures how much information about photon A is hidden in its correlations with photon B.

Two limiting cases: If the two photons are not entangled, photon A has a definite pure state and $\hat{\rho}_A$ has eigenvalues $\{1, 0\}$; the entropy is $S = -1 \cdot \log_2 1 - 0 \cdot \log_2 0 = 0$, meaning no uncertainty. If the pair is maximally entangled, all information about photon A is locked in its correlation with B; $\hat{\rho}_A = \mathbb{I}/2$ with eigenvalues $\{\frac{1}{2}, \frac{1}{2}\}$ and $S = 1$ bit — the more entangled the two photons are, the less information is available about each one and the greater the entropy of their reduced matrix .

For pure two-qubit states, the von Neumann entropy of $\hat{\rho}_A$ is an clear entanglement measure. For mixed states $S(\hat{\rho}_A)$ indistinguishably mixes entanglement uncertainty with classical mixing uncertainty, so a high value does not guarantee that there is actual entanglement. That is why we need more metrics.

Purity of the reduced state

The purity of $\hat{\rho}_A$ is

$$\boxed{\mathcal{P}(\hat{\rho}_A) = \mathrm{Tr}\big(\hat{\rho}_A^2\big) \;\in\; \big[\tfrac{1}{2},\, 1\big].} \tag{3.51}$$

$\mathcal{P} = 1$ when $\hat{\rho}_A$ is a pure state (separable pair) and drops to $\frac{1}{2}$ when $\hat{\rho}_A = \mathbb{I}/2$ (maximally entangled pair). It is the complement of Von Neumann entropy - cheaper to compute.

3.7.2 Family 2: Direct entanglement metrics

These metrics quantify entanglement directly by operating on the full 4×4 matrix $\hat{\rho}$.

Global state purity

Before any entanglement-specific quantity, it is useful to know how mixed the two-photon state is overall:

$$\mathcal{P}(\hat{\rho}) = \mathrm{Tr}\big(\hat{\rho}^2\big) \;\in\; \big[\tfrac{1}{4},\, 1\big]. \tag{3.52}$$

$\mathcal{P} = 1$ is a pure state; $\mathcal{P} = 1/4$ is the completely mixed state $\hat{\rho} = \mathbb{I}/4$. This metric does not measure entanglement by itself — a mixed state can be entangled or separable regardless of its purity. A low global purity signals that noise or decoherence has degraded the state; the remaining metrics then determine how much entanglement survives.

Concurrence

The concurrence, introduced by Wootters [21], measures entanglement as the overlap between $\hat{\rho}$ and its *spin-flipped* version. It is defined as

$$\boxed{C(\hat{\rho}) = \max\big(0,\; \lambda_1 - \lambda_2 - \lambda_3 - \lambda_4\big)} \tag{3.53}$$

where $\lambda_1 \geq \lambda_2 \geq \lambda_3 \geq \lambda_4$ are the eigenvalues in decreasing order of the matrix

$$R = \sqrt{\sqrt{\hat{\rho}}\;\tilde{\rho}\;\sqrt{\hat{\rho}}}, \qquad \tilde{\rho} = (\hat{\sigma}_y \otimes \hat{\sigma}_y)\,\hat{\rho}^*\,(\hat{\sigma}_y \otimes \hat{\sigma}_y), \tag{3.54}$$

with $\hat{\rho}^*$ denoting the complex conjugate in the computational basis $|HH\rangle$, $|HV\rangle$, $|VH\rangle$, and $|VV\rangle$. $\tilde{\rho}$ is the spin-flipped version of $\hat{\rho}$ and R measures the overlap between them. C runs from 0 (no entanglement) to 1 (maximally entangled).

It is worth analyzing the physics behind the spin-flip operation. $\hat{\sigma}_y$ acts on a single polarization qubit as

$$\hat{\sigma}_y = \begin{pmatrix} 0 & -i \\ i & 0 \end{pmatrix}, \quad \hat{\sigma}_y\,|H\rangle = i\,|V\rangle\,, \quad \hat{\sigma}_y\,|V\rangle = -i\,|H\rangle\,, \tag{3.55}$$

exchanging horizontal and vertical polarization with phases $\pm i$. Applied to both photons at once, $\hat{\sigma}_y \otimes \hat{\sigma}_y$ performs a simultaneous polarization flip. A Bell state is invariant under this operation; a separable state maps to an orthogonal state.

For example, For $|\Psi^+\rangle = \frac{1}{\sqrt{2}}(|HV\rangle + |VH\rangle)$:

$$(\hat{\sigma}_y \otimes \hat{\sigma}_y) |HV\rangle = (\hat{\sigma}_y |H\rangle) \otimes (\hat{\sigma}_y |V\rangle) = (i |V\rangle) \otimes (-i |H\rangle) = |VH\rangle ,$$
$$(\hat{\sigma}_y \otimes \hat{\sigma}_y) |VH\rangle = |HV\rangle , \tag{3.56}$$

so $(\hat{\sigma}_y \otimes \hat{\sigma}_y) |\Psi^+\rangle = |\Psi^+\rangle$: the Bell state comes out unchanged ($C = 1$). For a separable state $|HH\rangle$:

$$(\hat{\sigma}_y \hat{\otimes} \sigma_y) |HH\rangle = (i |V\rangle) \otimes (i |V\rangle) = - |VV\rangle , \tag{3.57}$$

which is orthogonal to $|HH\rangle$ ($C = 0$).

For a pure state $|\psi\rangle$, the concurrence reduces to $C = | \langle\psi| (\hat{\sigma}_y \otimes \hat{\sigma}_y) |\psi^*\rangle |$, which avoids the full eigendecomposition. For mixed states, the R matrix is needed because there is no single state vector.

Entanglement of formation

The entanglement of formation is the minimum quantity of entanglement, defined in ebits, that contains a quantum mixed state. [21]:

$$\boxed{E_F(\hat{\rho}) = h\left(\frac{1 + \sqrt{1 - C(\hat{\rho})^2}}{2}\right),} \tag{3.58}$$

where $h(x) = -x \log_2 x - (1 - x) \log_2(1 - x)$ is the binary entropy function. For a pure two-qubit state $|\psi\rangle$, the eigenvalues of $\hat{\rho}_A$ are $\nu = \frac{1+\sqrt{1-C^2}}{2}$ and $1 - \nu$, so $E_F = h(\nu) = S(\hat{\rho}_A)$: formation entropy and von Neumann entropy coincide for pure states. For mixed states they diverge, and the Wootters result in Eq. (3.58) provides the only known closed form.

Negativity and the Peres–Horodecki criterion

In 1996, Peres and Horodecki proved that for two-qubit systems, the partial transpose provides an exact test for entanglement [22, 23]. The 4×4 density matrix can be written in 2×2 blocks organized by the state of photon A:

$$\hat{\rho} = \begin{pmatrix} A & B \\ C & D \end{pmatrix}, \qquad A = \begin{pmatrix} \rho_{HH,HH} & \rho_{HH,HV} \\ \rho_{HV,HH} & \rho_{HV,HV} \end{pmatrix}, \quad \text{etc.} \tag{3.59}$$

Partial transposition with respect to photon B transposes the contents of each block, leaving the structure of photon A unchanged and reversing the order of the indices:

$$\hat{\rho}^{T_B} = \begin{pmatrix} A^T & B^T \\ C^T & D^T \end{pmatrix}. \qquad A^T = \begin{pmatrix} \rho_{HH,HH} & \rho_{HV,HH} \\ \rho_{HH,HV} & \rho_{HV,HV} \end{pmatrix}, \quad \text{etc.} \tag{3.60}$$

Any valid density matrix has non-negative eigenvalues. For a separable state $\hat{\rho}_{\text{sep}} = \sum_i p_i \, \hat{\rho}_i^A \otimes \hat{\rho}_i^B$, the partial transpose gives $\hat{\rho}_{\text{sep}}^{T_B} = \sum_i p_i \, \hat{\rho}_i^A \otimes (\hat{\rho}_i^B)^T$, which is still a valid density matrix (transposing a density matrix always gives another density matrix), so all eigenvalues stay non-negative. For an entangled state, the partial transpose breaks this structure and at least one eigenvalue becomes negative: the operation reveals correlations that cannot exist in any separable state.

The negativity, introduced by Vidal and Werner [24], quantifies those negative eigenvalues:

$$\boxed{\mathcal{N}(\hat{\rho}) = \frac{\|\hat{\rho}^{T_B}\|_1 - 1}{2} = \sum_i \frac{|\lambda_i^{T_B}| - \lambda_i^{T_B}}{2} = \sum_{\lambda_i<0} |\lambda_i|,} \tag{3.61}$$

where $\|\cdot\|_1$ is the trace norm (the sum of the absolute values of all eigenvalues). This equality can be explicitly derived by noting that the partial transpose operation preserves the trace:

$$\mathrm{Tr}(\hat{\rho}) = \mathrm{Tr}(\hat{\rho}^{T_B}) = 1 \tag{3.62}$$

Let $P = \sum_{\lambda_i \geq 0} \lambda_i$ be the sum of the non-negative eigenvalues, and $\mathcal{N} = \sum_{\lambda_i<0} |\lambda_i|$ be the sum of the absolute values of the negative eigenvalues. Since the trace is the sum of all eigenvalues:

$$P - \mathcal{N} = 1 \implies P = 1 + \mathcal{N} \tag{3.63}$$

The trace norm computes the sum of the absolute values of all eigenvalues:

$$\|\hat{\rho}^{T_B}\|_1 = \sum_i |\lambda_i| = P + \mathcal{N} = 1 + 2\mathcal{N} \tag{3.64}$$

Rearranging for $\mathcal{N}$ directly yields the expression for negativity:

$$\mathcal{N}(\hat{\rho}) = \frac{\|\hat{\rho}^{T_B}\|_1 - 1}{2} \tag{3.65}$$

The value of $\mathcal{N}$ ranges from 0 to 0.5 for two qubits.

For $|\Psi^+\rangle = \frac{1}{\sqrt{2}}(|HV\rangle + |VH\rangle)$:

$$\hat{\rho} = \frac{1}{2}\begin{pmatrix} 0 & 0 & 0 & 0 \\ 0 & 1 & 1 & 0 \\ 0 & 1 & 1 & 0 \\ 0 & 0 & 0 & 0 \end{pmatrix}, \qquad \hat{\rho}^{T_B} = \frac{1}{2}\begin{pmatrix} 0 & 0 & 0 & 1 \\ 0 & 1 & 0 & 0 \\ 0 & 0 & 1 & 0 \\ 1 & 0 & 0 & 0 \end{pmatrix}. \tag{3.66}$$

The eigenvalues of $\hat{\rho}^{T_B}$ are $\{0.5, 0.5, 0.5, -0.5\}$, so $\mathcal{N} = 0.5$, which is the maximum for two qubits.

Logarithmic negativity

The logarithmic negativity is

$$\boxed{E_{\mathcal{N}}(\hat{\rho}) = \log_2 \|\hat{\rho}^{T_B}\|_1 = \log_2(2\mathcal{N} + 1),} \tag{3.67}$$

and ranges from 0 to 1. Three properties motivate this form over $\mathcal{N}$ directly. First, *additivity*: the trace norm of a tensor product factorizes, $\|\hat{\rho}_1^{T_B} \otimes \hat{\rho}_2^{T_B}\|_1 = \|\hat{\rho}_1^{T_B}\|_1 \cdot \|\hat{\rho}_2^{T_B}\|_1$, so the logarithm converts the product into a sum and entanglement becomes additive over independent pairs. Second, the scale $[0, 1]$ matches that of the concurrence and formation entropy, making direct comparisons between metrics meaningful. Third, $E_{\mathcal{N}} = 1$ for any Bell state, equal to $E_F = 1$ ebit.

3.7.3 Family 3: Fidelity and comparison with ideal states

The metrics in this family do not quantify entanglement in the abstract. They answer a different question: how close is the experimental state to a specific theoretical reference?

General fidelity

For any two quantum states $\hat{\rho}$ and $\hat{\sigma}$, the fidelity is [1]

$$F(\hat{\rho}, \hat{\sigma}) = \left(\mathrm{Tr}\sqrt{\sqrt{\hat{\rho}}\,\hat{\sigma}\,\sqrt{\hat{\rho}}}\right)^2 . \tag{3.68}$$

When the reference is a pure state $\hat{\sigma} = |\psi\rangle\langle\psi|$, this simplifies to $F = \langle\psi|\,\hat{\rho}\,|\psi\rangle$, which is the probability of detecting $|\psi\rangle$ in a projective measurement on $\hat{\rho}$. For two pure states it further reduces to $F = |\langle\psi|\phi\rangle|^2$.

Fidelity to the closest pure state

A natural and unbiased reference is the dominant eigenvector $|e_1\rangle$ of $\hat{\rho}$, i.e. the pure state that provides the closest approximation to the experimental state. The corresponding fidelity equals the dominant eigenvalue:

$$F_{\max} = \langle e_1|\,\hat{\rho}\,|e_1\rangle = \lambda_1 . \tag{3.69}$$

$F_{\max} > 0.5$ certifies entanglement, since no separable state can have fidelity greater than 0.5 with any pure entangled state. $F_{\max} > 0.5$ certifies entanglement only if $|e_1\rangle$ itself is entangled, since no separable state can have fidelity greater than 0.5 with a pure entangled state; if $|e_1\rangle$ is itself separable, $F_{\max}$ provides no information about the entanglement of $\hat{\rho}$.

One might instead compute the fidelity to the four standard Bell states $|\Phi^\pm\rangle$, $|\Psi^\pm\rangle$. This is simpler but less rigorous. The four standard Bell states are only a *basis* of the maximally entangled subspace, not its only elements: any unitary combination of them is also maximally entangled. A source can produce a maximally entangled state with low fidelity to all four standard Bell states simply because its polarization frame is rotated relative to the H/V basis. Using $F_{\max}$ corrects for this: the dominant eigenvector adapts to whatever state the source actually produces.

Werner state model and mixing parameter

The Werner state [25] is the standard model for a Bell state degraded by white noise:

$$\boxed{\hat{\rho}_W(p) = p\,|e_1\rangle\langle e_1| + \frac{1-p}{4}\,\mathbb{I},} \tag{3.70}$$

where $|e_1\rangle$ is the dominant eigenvector of $\hat{\rho}$ and $p \in [0, 1]$ is the mixing parameter. $p = 1$ gives a perfect Bell state with no noise; $p = 0$ gives the completely mixed state $\mathbb{I}/4$ with no entanglement. Physically, p is the probability that a photon pair from the source is genuinely in the entangled state $|e_1\rangle$; with probability $1 - p$ it ends up in the uniform mixture.

The mixing parameter is extracted from the fidelity. Substituting Eq. (3.70) into $F_W = \langle e_1|\,\hat{\rho}_W\,|e_1\rangle$:

$$F_W = p + \frac{1-p}{4} = \frac{1+3p}{4}, \tag{3.71}$$

which gives

$$\boxed{p = \frac{4F_{\text{max}} - 1}{3}.} \tag{3.72}$$

Equivalently, p can be found numerically by minimizing $\|\hat{\rho} - \hat{\rho}_W(p)\|_F$ over p, where $\|\cdot\|_F$ is the Frobenius norm; both methods give the same result.

It should be noted hat using $|e_1\rangle$ rather than a fixed standard Bell state as the reference in Eq. (3.70) is not merely a technical detail. When the source operates outside the standard H/V basis, fitting against a fixed Bell state gives a Werner parameter that severely underestimates the actual entanglement quality. The correct procedure is to first identify $|e_1\rangle$ from the dominant eigenvector of the reconstructed $\hat{\rho}$, and then carry out the Werner fit against that state.

Chapter 4.

System design and methodology

4.1 Design alternatives and decision-making

The polarization analysis module is the central element of any QST setup: it is the component that selects which polarization projection is measured in each arm. In this experiment, that module was implemented using a fiber-bench (*U-bench*) architecture from Thorlabs, in which a pair of collimators faces each other across an open free-space section. Inside that section, the waveplate and polarizer are placed in sequence; the polarizer transmits one polarization component, which is then collected back into fiber by the output collimator and routed to the SPAD detector.

The choice of U-bench type — fixed or adjustable — was not trivial and had direct consequences for the fiber types used throughout the setup, and therefore for the PMD experienced by the photons. The following subsections describe the four successive configurations tested, each evaluated through a complete QST measurement.

4.1.1 Configuration 1 (QST 1): fixed U-benches with PM fiber

The first and most straightforward option was to use fixed U-benches (Thorlabs FBC-1550PM-APC), whose collimators are factory-aligned and require no manual adjustment. This was a deliberate choice to avoid the time-consuming and uncertain alignment procedure required by adjustable U-benches, which have multiple degrees of freedom and offer no guarantee of reaching the optimum within a reasonable time.

The fixed U-bench collimators are permanently connected with polarization-maintaining (PM) fiber with FC/APC connectors. Since the EPPS source outputs SMF with FC/PC connectors, a direct FC/PC–APC patchcord was used at the U-bench input on each channel. The same patchcord type was used at the U-bench output to connect back to the SMF fiber of the MPD SPAD detectors. The complete signal path for each channel was therefore:

EPPS (SMF) → adp. PC/APC → PM fiber → U-bench (QWP/HWP + pol.) → PM fiber → adp. APC/PC → SPAD (SMF)

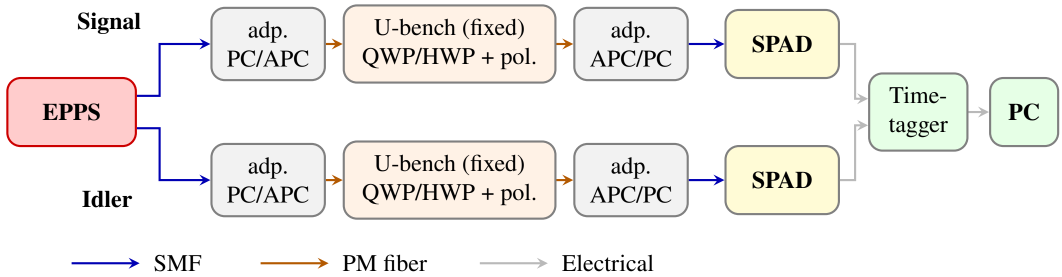

Figure 10: QST 1 setup. Both channels route through PM fiber inside and around the fixed U-benches (Thorlabs FBC-1550PM-APC), connected to the SMF outputs of the EPPS source and the SPAD detectors via FC/PC–APC adapters. The high birefringence of the PM fiber introduced severe PMD, resulting in a reconstructed purity of $\mathcal{P} = 0.28$. (Note: HWP = Half-Wave Plate, QWP = Quarter-Wave Plate, Pol = Polarizer)

The reconstructed purity was $\mathcal{P} = 0.28$, indicating a highly mixed state; while purity alone does not quantify entanglement directly (Section 3.7), a state this mixed is very unlikely to retain any useful degree of entanglement. The initial hypothesis was detector saturation: optical attenuators (10 dB + 5 dB) were inserted at the SPAD inputs and the measurement was repeated, resulting in the same low purity. Saturation was therefore ruled out. The correct diagnosis, consistent with the theoretical predictions of Lim et al. [9], was PMD-induced decoherence: the PM fiber introduces a differential group delay that, for a broadband source such as the EPPS, accumulates fast enough to eliminate the polarization coherence over fiber lengths as short as those used in the setup. The attenuators were removed and a spectral filtering strategy was adopted instead.

4.1.2 Configuration 2 (QST 2): fixed U-benches with narrowband filters

The first mitigation strategy tested was spectral filtering. The physical reasoning follows directly from the PMD coherence model (Section 3.5): reducing the photon bandwidth narrows the range of wavelengths propagating through the PM fiber. Since each wavelength accumulates a different polarization transformation, a broader spectrum produces a wider spread of transformed states that average out at the detector, destroying the coincidence signal. Filtering the spectrum limits this spread and partially recovers the polarization coherence.

Two fiber-coupled optical bandpass filters were inserted between the EPPS source and the U-benches — one per channel. The signal channel used a Santec OTF-300 [26] tunable optical filter (range 1290–1330 nm, passband ±7.5 nm, SMF, FC/APC, tuned to 1320 nm), while the idler channel used a CWDM filter (channel 1311 nm, passband ±6.5 nm, SMF, SC/APC).

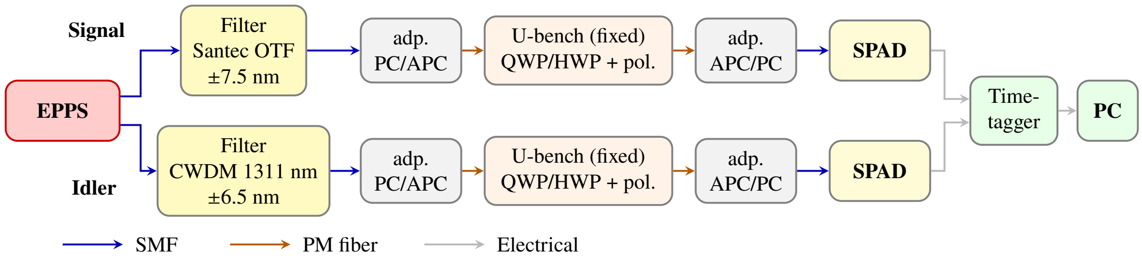

Figure 11: QST 2 setup. A narrowband filter is inserted in each channel between the EPPS source and the U-bench: a Santec OTF-300 (±7.5 nm passband, tuned to 1320 nm) on the signal channel and a CWDM filter (±6.5 nm passband, centred at 1311 nm) on the idler channel. Purity improved to $\mathcal{P} = 0.61$.

The purity improved substantially to $\mathcal{P} = 0.61$, confirming the PMD hypothesis. However, the PM fiber of the U-benches remained in the optical path, and residual decoherence limited the purity achievable with this configuration.

4.1.3 Configuration 3 (QST 3): mechanical stabilization attempt

The third configuration was identical to QST 2 optically, but added mechanical stabilization: the fiber patch cords were fixed to the optical table with adhesive tape, and the U-benches were fastened more firmly to prevent displacement during waveplate rotation. Any small displacement of the U-bench or fiber during waveplate changes alters the polarization transformation of that arm for each projection, directly invalidating the QST reconstruction.

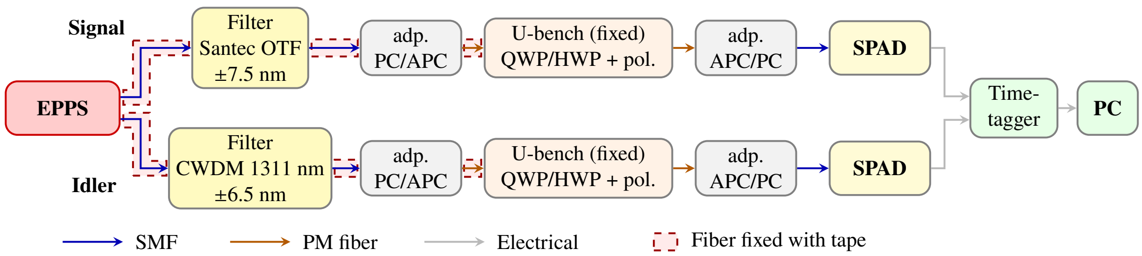

Figure 12: QST 3 setup. Identical to QST 2 optically; fiber patch cords were fixed to the optical table with adhesive tape (marked in red) and the U-benches were fastened more firmly to prevent displacement during waveplate rotation. Purity decreased to $\mathcal{P} = 0.53$.

Contrary to expectations, the purity decreased to $\mathcal{P} = 0.53$. Two effects contributed: adhesive tape may apply mechanical stress to the PM fiber, inducing additional birefringence; and the coincidence count rate dropped by roughly half compared to QST 2, worsening the signal-to-noise ratio. The attempt was abandoned and the tape removed.

4.1.4 Configuration 4 (QST 4): adjustable U-benches with SMF

Once all mitigation strategies compatible with the fixed U-bench architecture had been exhausted, the decision was made to move to adjustable U-benches. Replacing the collimator pigtails with

SMF eliminates all PM fiber from the optical path. Since SMF has a residual birefringence three orders of magnitude smaller than PM fiber ($\Delta n \sim 10^{-7}$ vs. $\Delta n \sim 4 \times 10^{-4}$), the polarization transformation across the photon bandwidth becomes negligible — each wavelength component exits the fiber with nearly the same polarization state, and the coincidence signal is preserved.

The alignment of adjustable U-benches requires independent adjustment of tip, tilt, and lateral position on both collimators, and is time-consuming. This is the reason the option had been deferred until all fixed U-bench alternatives were exhausted. The narrowband filters were also removed: with PM fiber eliminated, the broad photon bandwidth no longer caused significant decoherence.

EPPS (SMF) → U-bench adjustable (SMF, QWP/HWP + pol.) → SPAD (SMF)

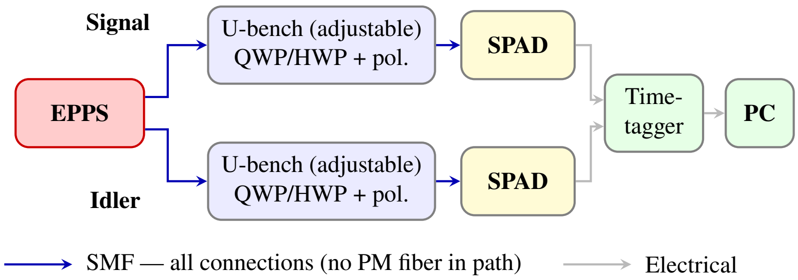

Figure 13: QST 4 setup. Adjustable U-benches with SMF pigtails eliminate all PM fiber from the optical path. Narrowband filters removed. Purity reached $\mathcal{P} = 0.79$.

The purity reached $\mathcal{P} = 0.79$, the highest value obtained in the local characterization. This configuration became the reference setup for the entanglement metrics analysis (Section 5.4) and the distribution experiment (Section 5.5).

4.2 Final architecture

The distribution experiment connects two laboratories within the CTU building through the existing passive fiber infrastructure. The link uses three fiber patch panels: one in Laboratory 1 (the source laboratory), one on the sixth floor, and one in Laboratory 2 (the remote node). The two laboratories are not directly connected; the fiber path passes through the sixth-floor panel in both directions. The total fiber length, measured by OTDR, is 738 m. The route is assembled from several shorter segments joined with connectors, each introducing a small additional insertion loss (Section 5.5). The approximately 10 m segment between the source and the patch panel in Laboratory 1 was itself assembled from several shorter patch cords, each characterized individually with the tunable laser and power meter before integration.

From the EPPS source in Laboratory 1, two SMF patch cords carry the signal and idler photons to the patch panel in Laboratory 1. The fibers then run through the building infrastructure to the sixth-floor panel and on to Laboratory 2, where they loop back at the patch panel and return via the same route to the SPAD detectors in Laboratory 1. Each photon of a pair therefore travels independently through the full loop before being detected.

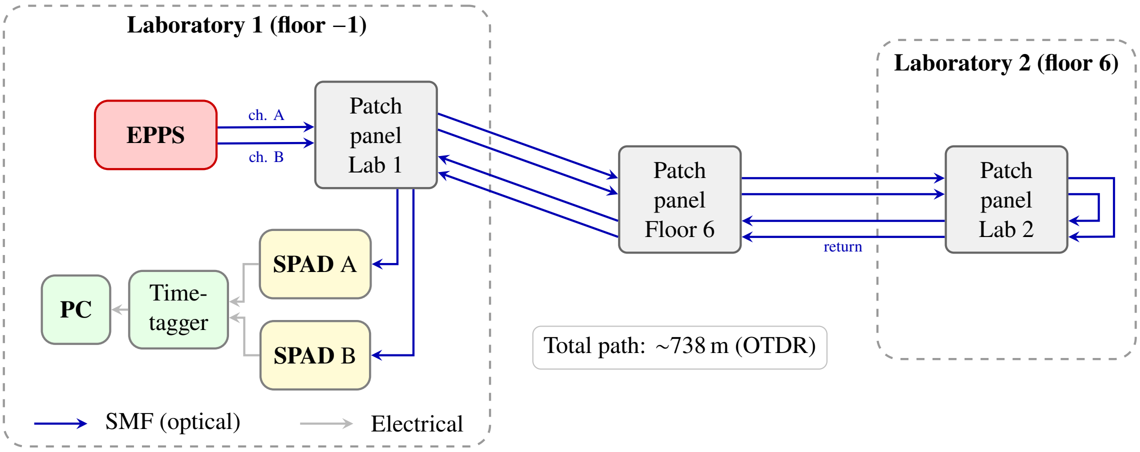

Figure 14: Final distribution architecture. The EPPS source in Laboratory 1 sends both photon channels through the building fiber infrastructure via three passive patch panels (Laboratory 1, sixth floor, and Laboratory 2). The photons loop back at Laboratory 2 and return to the SPAD detectors in Laboratory 1. Total fiber path: 738 m**.**

Before measuring the distribution, the system was characterized under direct connection conditions: the EPPS outputs were connected directly to the SPAD detectors via short SMF cables, without the building fiber infrastructure. This reference measurement used the same 9 dB attenuators retained throughout the experiment, ensuring identical detector operating conditions. The coincidence histogram, detection rates, and coincidence rate per second serve as the baseline for comparison with the distribution results in Section 5.5.

(a) EPPS source with output fibers.

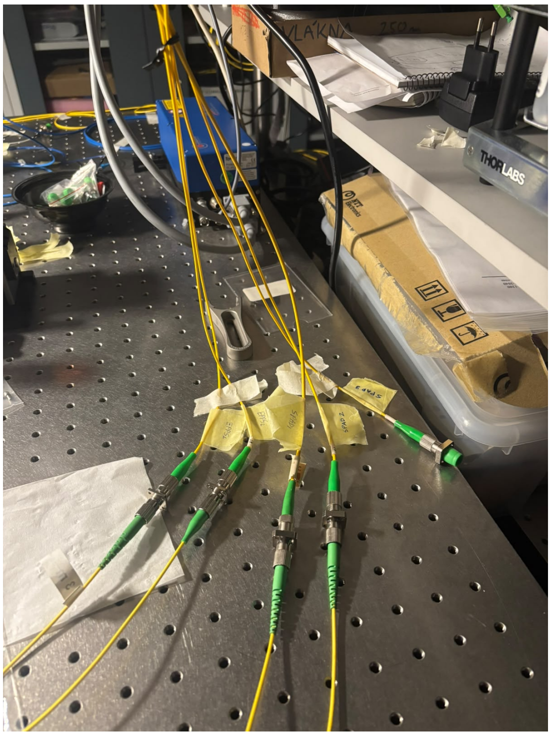

(b) Labeled fiber connectors (EPPS1, EPPS2, SPAD1, SPAD2).

(c) Fiber routing along the laboratory ceiling.

(d) Patch panel in Laboratory 1.

Figure 15: Fiber distribution infrastructure in Laboratory 1.

4.3 Equipment and components

This section describes the instruments and optical components used throughout the experimental work. Table 9 provides a summary; the subsections that follow give the relevant technical details for each category.

Table 9: Summary of equipment used in the experiment. η: photon detection efficiency; DCR: dark count rate; FWHM: full width at half maximum.

Component	Model	Manufacturer	Key parameter
Entangled pair source	EPPS-O	S-Fifteen Instruments	> 500 000 pairs/s, 1320 nm
SPAD detector (×2)	PDM-IR	MPD	η up to 30%, DCR ≥300 c/s
Time-to-digital converter	Time Tagger 20	Swabian Instruments	34 ps RMS jitter, 8 channels
Tunable optical filter	OTF-300	Santec	±7.5 nm passband, 1290–1330 nm
CWDM filter	CWFD01E2E2BS155	OEM (unidentified)	±6.5 nm passband, 1311 nm
Fixed U-bench	FBC-1550PM-APC	Thorlabs	PM fiber, FC/APC
Adjustable U-bench	FBP-A-FC	Thorlabs	SMF compatible, FC/PC
Half-wave plate	FBR-AH3	Thorlabs	Achromatic, 1100–2000 nm
Quarter-wave plate	FBR-AQ3	Thorlabs	Achromatic, 1100–2000 nm
Linear polarizer	FBR-LPNIR	Thorlabs	650–2000 nm, rotating mount
Tunable laser (aux.)	CoBrite DX4	IDPhotonics	1550 nm, fiber-coupled
Power meter	PM100A	Thorlabs	Analog + digital display
OTDR	FTB-1	EXFO	Fiber loss characterization

4.3.1 Entangled photon pair source

The photon pair source is the S-Fifteen Instruments EPPS-O [15], a compact fiber-coupled module that generates polarization-entangled photon pairs at 1320 nm via type-II SPDC in a PPKTP crystal driven by an integrated 660 nm pump laser. The source produces more than 5×10^5 pairs per second with a polarization entanglement visibility exceeding 96% [15]. Signal and idler photons are separated internally by a WDM multiplexer and delivered through two SMF output fibers with FC/PC connectors.

4.3.2 Single-photon detectors

The detectors are MPD PDM-IR modules [17]: fiber-coupled SPADs operating in Geiger mode (Section 3.4) based on an InGaAs/InP junction sensitive from 900 to 1700 nm, Peltier-cooled to reduce thermal noise. The photon detection efficiency reaches up to 30% near 1300–1400 nm at

V_{EX} = 7 V, covering the 1320 nm emission wavelength of the EPPS source, with a timing jitter as low as 80 ps FWHM and a DCR as low as 300 c/s in free-running mode [17].

4.3.3 Time-to-digital converter

Timestamping of detection events is performed by the Swabian Instruments Time Tagger 20 [27], which converts each SPAD output pulse into a digital timestamp referenced to an internal clock: 8 input channels, 34 ps RMS jitter, 1 ps digital resolution, 6 ns dead time per channel, USB 2.0 interface at up to 9 Mtags/s. Coincidence histograms and count rates are exported by Swabian Instruments' own software and loaded in Python for further analysis (Section 4.5).

4.3.4 Polarization analysis module

Each measurement arm uses a Thorlabs U-bench containing an achromatic half-wave plate (FBR-AH3, 1100–2000 nm) [28], an achromatic quarter-wave plate (FBR-AQ3, 1100–2000 nm) [29], and a rotating linear polarizer (FBR-LPNIR, 650–2000 nm) [30]. All three have a graduated rotation scale with $\sim 1^\circ$ resolution, which is the angular uncertainty used in the Monte Carlo analysis of Section 5.3. The **fixed U-bench** (FBC-1550PM-APC) was used in QST 1–3; the **adjustable U-bench** (FBP-A-FC), fitted with SMF pigtails, was used in QST 4 and the distribution experiment (alignment procedure in Section 4.4).

4.3.5 Spectral filters

Two narrowband filters were used in QST 2 and QST 3. The signal channel used a Santec OTF-300 [26] (±7.5 nm FWHM, tuned to 1320 nm); the idler channel used a CWDM filter (±6.5 nm centred at 1311 nm, IL 0.35 dB, PDL 0.02 dB). Both removed in QST 4 once PM fiber was eliminated.

4.3.6 Auxiliary instrumentation

Link loss was characterized using an IDPhotonics CoBrite DX4 tunable laser [31] at 1550 nm and a Thorlabs PM100A power meter [32]. Full fiber-path loss profiling used an EXFO FTB-1 OTDR [33].

4.3.7 Fiber connectors and attenuators

All connections use FC/APC or FC/PC connectors on SMF-28 fiber, with FC/PC–APC adapters at the EPPS–U-bench interfaces. End-faces were inspected and cleaned before each session (Section 4.4). Fixed 9 dB attenuators were inserted at each SPAD input for the source characterization and distribution measurements.

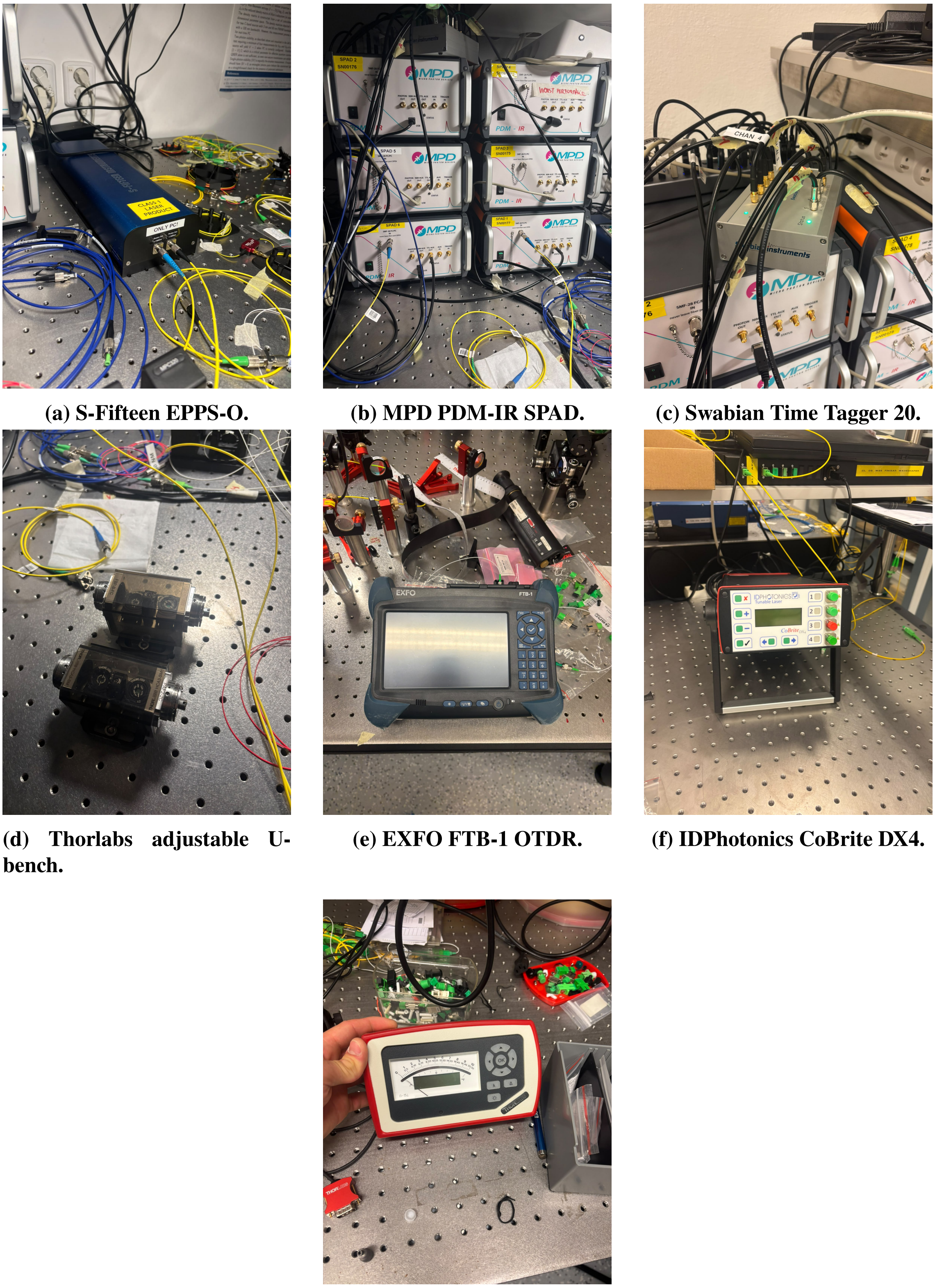

(a) S-Fifteen EPPS-O. **(b) MPD PDM-IR SPAD.** **(c) Swabian Time Tagger 20.**

(d) Thorlabs adjustable U-bench. **(e) EXFO FTB-1 OTDR.** **(f) IDPhotonics CoBrite DX4.**

(g) Thorlabs PM100A power meter.

Figure 16: Main instruments used in the experiment.

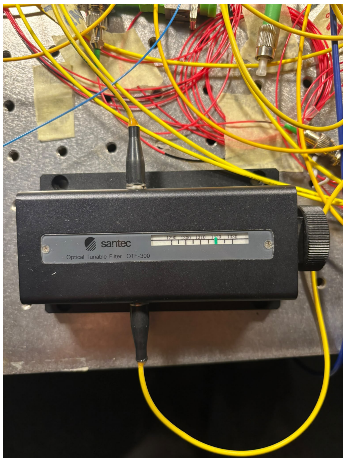

(a) Santec OTF-300 filter.

(b) CWDM filter (1311 nm).

(c) Thorlabs FBR-LPNIR polarizer.

(d) Thorlabs FBR-AQ3 QWP.

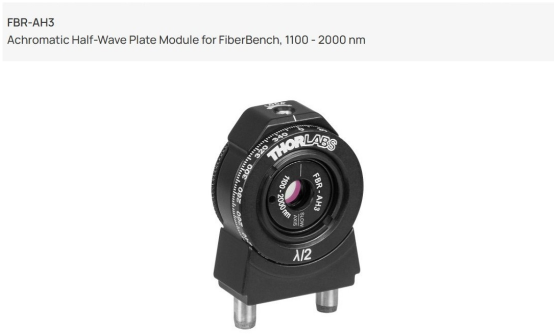

(e) Thorlabs FBR-AH3 HWP.

Figure 17: Optical components used in the polarization analysis module.

4.4 Measurement protocols

4.4.1 Fiber inspection and cleaning

Before every measurement session, all fiber connector end-faces were inspected under a fiber inspection microscope and cleaned with a one-click fiber cleaner. A connector was considered ready only when the core region showed no visible contamination or scratches.

4.4.2 Detector characterization

The dark count rate of each SPAD was measured with the fiber input capped, in free-running mode at standard operating conditions. The Time Tagger 20 recorded counts with a 1 s integration window for a total of 60 s per detector. The mean and standard deviation were used as the dark count correction in all subsequent measurements. The procedure was applied to all four available units; the two with the most similar rates were selected (Section 5.1).

4.4.3 Source characterization

The source was connected directly to the two selected SPAD detectors with 9 dB attenuators at each input. The Time Tagger 20 recorded a bidirectional coincidence histogram and the single-channel count rates in parallel. A virtual channel offset ($\Delta t = 0$) centred the coincidence peak. The peak coincidence rate, average background, Signal-to-Noise Ratio (SNR), and Coincidence-to-Accidental Ratio (CAR) were extracted from the histogram.

4.4.4 U-bench alignment

The adjustable U-bench collimators were aligned by iteratively adjusting tip, tilt, and lateral position on both collimators while monitoring the transmitted power with the Thorlabs PM100A. The alignment was considered acceptable when no further improvement could be obtained from any adjustment.

4.4.5 QST measurement protocol

Each QST measurement consisted of 36 coincidence acquisitions covering all combinations of the six polarization projections $\{H, V, D, A, R, L\}$ on the two arms (waveplate settings in Table 12). Integration times were 60 s per projection for QST 1 and QST 4, and 120 s for QST 2 and QST 3.

The net coincidence count per configuration was obtained by integrating the histogram peak and subtracting the background estimated from a flat region away from the peak. For QST 1 and QST 4 the integration window was ±500 ps around the peak center; for QST 2 the bin size (1000 ps) captured the peak in a single bin; for QST 3 the window was ±300 ps. Background regions: −6000 to −4000 ps for QST 1–3; 3000 to 4000 ps for QST 4.

In addition, a reduced 16-projection reconstruction was performed for QST 1 using projections onto $\{H, V, D, R\}$ on each arm. The comparison with the full 36-projection result is discussed in Section 5.2.1.

4.5 Software and data processing

4.5.1 Data acquisition

The Time Tagger 20 is controlled via Swabian Instruments' own software. For each configuration, a virtual coincidence channel accumulates time differences into a histogram; single-channel count rates are recorded in parallel with a 1 s integration window. Both outputs are exported to tab-separated `.txt` files for offline processing (a valid Swabian Instruments Time Tagger license was required to use their Python library, which is in turn necessary to read and process the files generated by the Time Tagger).

4.5.2 QST reconstruction

The reconstruction pipeline runs in a Jupyter notebook (NumPy, SciPy). The 36 net coincidence counts are assembled into the measurement vector $\vec{n}$ and passed to two estimators in sequence. First, the Moore–Penrose pseudoinverse provides a fast initial estimate (Section 3.6.2). The physical reconstruction then follows from Maximum-Likelihood Estimation with Cholesky parametrization, minimized with `scipy.optimize.minimize` (`L-BFGS-B`), as described in Section 3.6.3.

4.5.3 Entanglement metrics and uncertainty

The full set of entanglement metrics defined in Section 3.7 is computed from the reconstructed matrix using NumPy. Uncertainties are estimated by the Monte Carlo simulation of Section 5.3: 500 realizations of $\pm 1^\circ$ Gaussian angular errors on the waveplates and polarizers, with Poisson shot noise added at each realization. The mean, standard deviation, and 95% confidence interval of each metric are reported in Section 5.4.

Chapter 5.

Experimental results

5.1 Detector and source characterization

Detector characterization

Four MPD PDM-IR SPAD detectors were available in the laboratory, connected to channels 3, 4, 5, and 6 of the Time Tagger 20. Before any optical measurement, the DCR of each unit was measured with the fiber input capped, following the protocol described in Section 4.4. The Time Tagger recorded count rates in 1 s bins over a 60 s acquisition window. The results are summarized in Table 10.

Table 10: Dark count rates for the four available SPAD detectors. Values are averaged over 60 s**.**

Channel	Mean DCR (counts/s)	Notes
3	2850	Selected
4	2941	Selected
5	602	Not used
6	8700	Not used

Channels 3 and 4 showed the most similar DCR values — 2850 and 2941 counts/s respectively — and were selected for all subsequent measurements. Channels 5 and 6 were not selected: channel 5, despite having the lowest DCR of 602 counts/s, was excluded because we wanted two detectors with similar noise levels so that any asymmetry in coincidence rates could be attributed to the optical path rather than detector differences; channel 6 was discarded for the same reason as channel 5; furthermore, due to ts high DCR of 8700 counts/s, which would have raised the accidental background and degraded the SNR.

Figure 18 shows the DCR distributions for all four channels over the acquisition window. The distributions are approximately Gaussian, consistent with the central limit theorem applied to Poisson-distributed photon counts accumulated over the 1 s integration window [16].

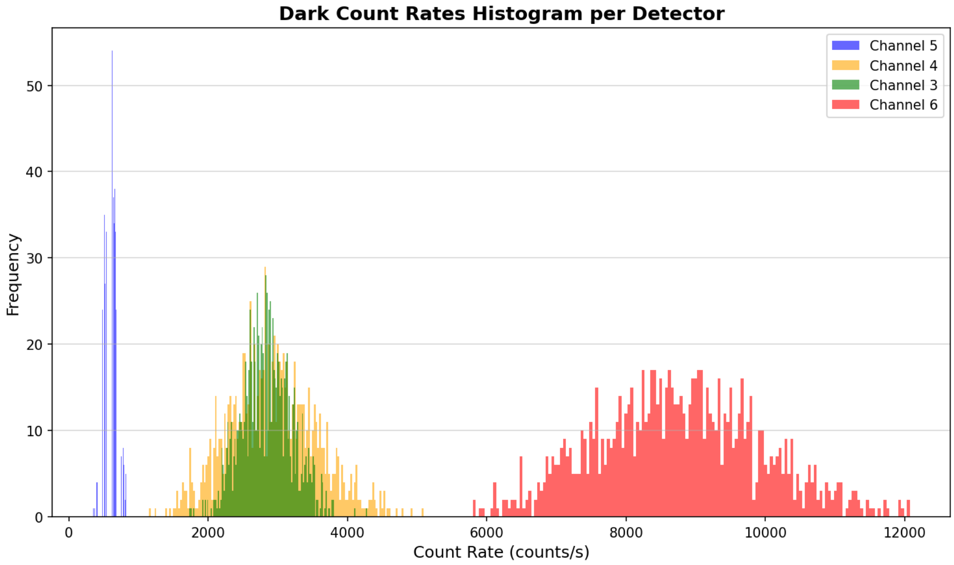

Figure 18: Dark count rate distributions for the four SPAD detectors (channels 3–6) over a 60 s acquisition with fiber inputs capped. The distributions are approximately Gaussian. Channels 3 and 4 were selected for the experiment based on their similar count rates (∼2900 counts/s).

Source characterization

The EPPS source was characterized by connecting its two outputs directly to the selected SPAD detectors via short SMF connections, with 10 dB attenuators at each detector input. The Time Tagger 20 recorded the single-channel detection rates on channels 3 and 4 and the bidirectional coincidence histogram between them.

The single-channel detection rates, averaged over the acquisition, were $\bar{R}_3 = 63\,081 \pm 415$ counts/s on channel 3 and $\bar{R}_4 = 68\,904 \pm 402$ counts/s on channel 4. These rates include contributions from true photon detections together with the intrinsic dark count rate of each detector (∼2900 counts/s, Table 10). The small standard eviations confirm that the source operates stably under continuous-wave pumping.

The coincidence histogram (Figure 19) shows a sharp peak at a physical delay of $\Delta t = 5.51$ ns, corresponding to the propagation time difference introduced by the cable lengths, as well as small differences in group velocity between the signal and idler wavelengths. The peak was shifted to zero in software by setting the virtual channel offset of the Time Tagger accordingly. The peak height was 388 counts per bin (bin width 10 ps), over an average background of 11.8 counts/bin. The figures of merit extracted from the histogram are summarized in Table 11.

Table 11: Source characterization results (10 dB attenuation per channel, direct connection). CAR computed over a ±0.5 ns coincidence window.

Parameter	Value
Singles rate, channel 3	63 081 ± 415 counts/s
Singles rate, channel 4	68 904 ± 402 counts/s
Peak height	388 counts/bin
Background (accidentals)	11.8 counts/bin
SNR (peak / background)	32.9
CAR (±0.5 ns window)	11.4
True coincidences (±0.5 ns)	13 494

SNR is computed from the peak height C_{peak} and background level C_{acc} (both in counts/bin) as SNR = $C_{\text{peak}}/C_{\text{acc}}$. CAR is computed over the ±0.5 ns window as CAR = $C_{\text{true}}/C_{\text{acc,win}}$, where C_{true} is the true coincidence count and $C_{\text{acc,win}}$ is the total accidental background within the same window.

The SNR of 32.9 and CAR of 11.4 confirm that the source produces a bright, high-purity photon pair flux with a low accidental background. These values serve as the baseline for all subsequent measurements. A second source characterization was performed immediately before the distribution experiment using 9 dB attenuators; those results are reported in Section 5.5 alongside the distribution data.

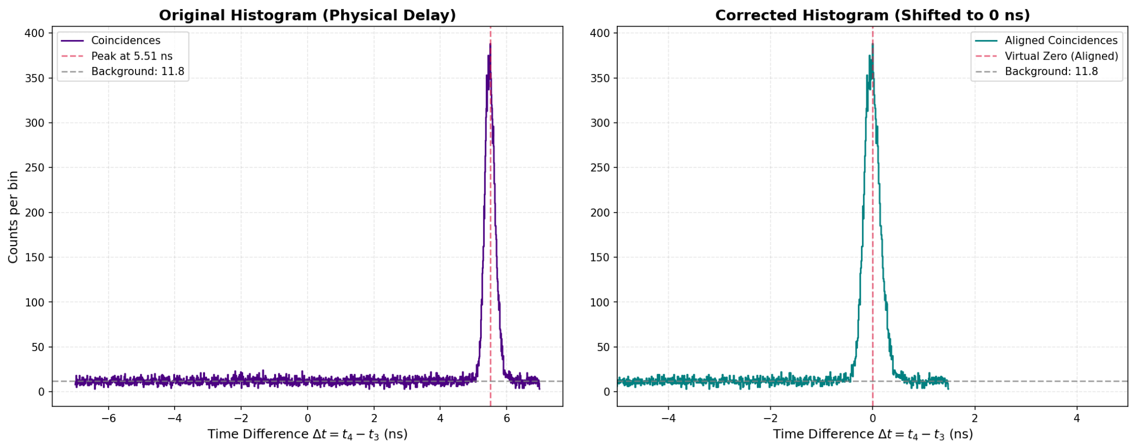

Figure 19: Coincidence histogram of the EPPS source under direct connection (10 dB attenuation per channel). Left: raw histogram showing the physical delay of 5.51 ns. Right: histogram shifted to zero by the virtual channel offset. The peak height is 388 counts per 10 ps bin over a background of 11.8 counts/bin, giving SNR = 32.9 **and CAR** = 11.4.

5.2 QST results

5.2.1 QST 1: fixed U-benches with PM fiber

The first QST measurement was performed using the configuration described in Section 4.1.1: fixed U-benches connected to the EPPS source and the SPAD detectors through PM fiber, with

FC/PC–APC adapters at both interfaces.

36-projection reconstruction

The 36 net coincidence counts, obtained following the protocol of Section 4.4.5, ranged from approximately 6700 to 11 900 counts per projection. The pseudoinverse estimate (Section 3.6.2) yielded the density matrix

$$\hat{\rho}_{\text{pinv}} = \begin{pmatrix} 0.186 & -0.028-0.002i & -0.017-0.003i & -0.061-0.004i \\ -0.028+0.002i & 0.298 & -0.015-0.008i & 0.035-0.009i \\ -0.017+0.003i & -0.015+0.008i & 0.313 & 0.027-0.001i \\ -0.061+0.004i & 0.035+0.009i & 0.027+0.001i & 0.203 \end{pmatrix}, \tag{5.1}$$

with eigenvalues $\{0.132,\ 0.215,\ 0.317,\ 0.336\}$ and purity $\mathcal{P}_{\text{pinv}} = 0.277$. The MLE reconstruction with Cholesky parametrization (Section 3.6.3) converged to a nearly identical result:

$$\hat{\rho}_{\text{MLE}} = \begin{pmatrix} 0.184 & -0.029-0.002i & -0.018-0.003i & -0.060-0.004i \\ -0.029+0.002i & 0.299 & -0.014-0.007i & 0.035-0.010i \\ -0.018+0.003i & -0.014+0.007i & 0.314 & 0.028-0.000i \\ -0.060+0.004i & 0.035+0.010i & 0.027+0.000i & 0.203 \end{pmatrix}, \tag{5.2}$$

with eigenvalues $\{0.132,\ 0.214,\ 0.318,\ 0.337\}$ and purity $\mathcal{P} = 0.277$. The close agreement between the pseudoinverse and MLE results confirms that the pseudoinverse estimate was already close to a physical state, which only requires a small correction to ensure a positive outcome.

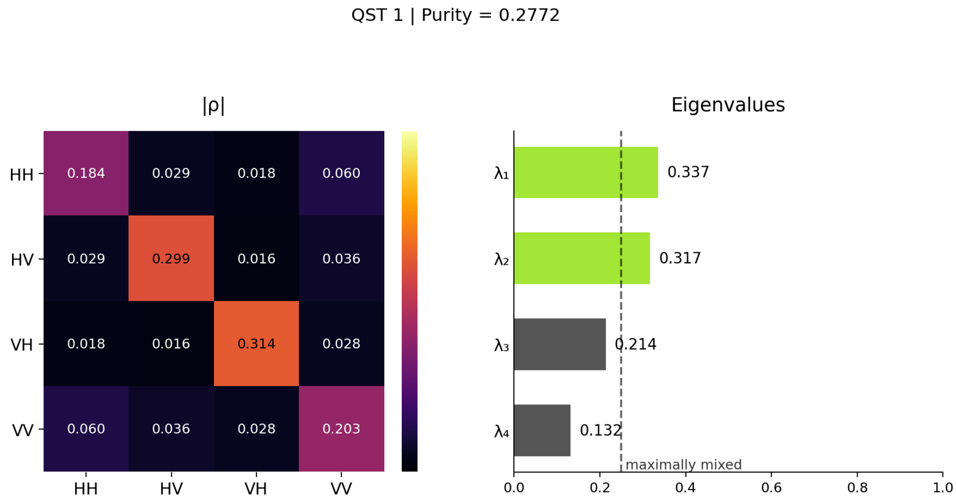

Figure 20: QST 1 reconstructed density matrix (36-projection MLE). Left: magnitude $|\rho|$. Right: eigenvalue spectrum. All four eigenvalues are close to 0.25, the value for a maximally mixed state (dashed line), indicating that the measured state is not a pure state.

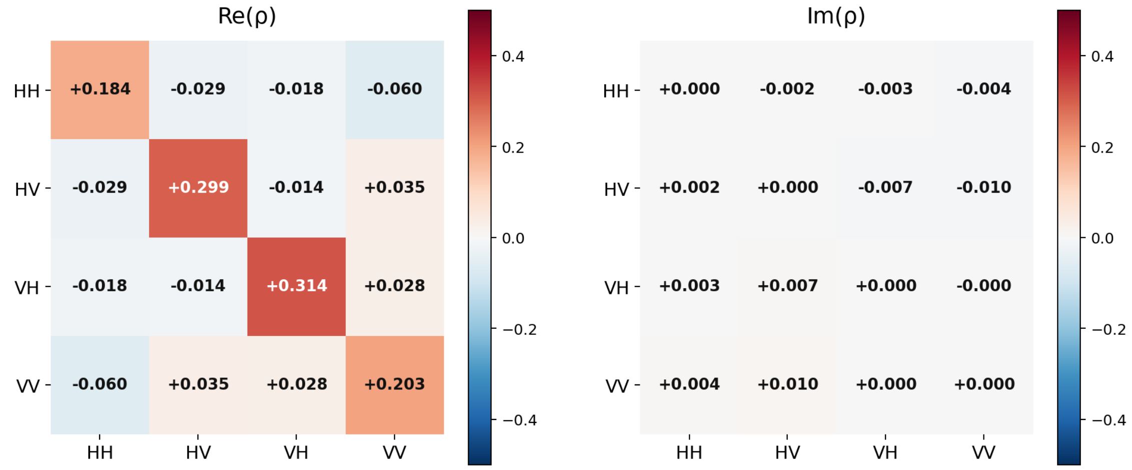

Figure 21: Real and imaginary parts of the QST 1 reconstructed density matrix. The diagonal populations are nearly equal (~0.18–0.31), and the off-diagonal coherences $\rho_{HH,VV}$ and $\rho_{VV,HH}$ — which would be close to 0.5 **for a maximally entangled Bell state — are reduced to approximately** -0.06.

The reconstructed purity of $\mathcal{P} = 0.277$ is far below the value expected for the entangled state generated by the source (visibility >96%, Section 4.3.1). The eigenvalue spectrum is close to $\{0.25, 0.25, 0.25, 0.25\}$, the spectrum of the maximally mixed state $\hat{\rho} = \frac{1}{4}\mathbb{I}$, indicating that almost all polarization entanglement was lost between the source and the detectors.

16-projection cross-check

For verification purposes, a reduced reconstruction was performed using only the projections onto $\{H, V, D, R\}$ on each arm (16 combinations), which is the minimum set required to fully determine the two-qubit density matrix (Section 3.6.2). The MLE reconstruction gave purity $\mathcal{P}_{16} = 0.287$, with eigenvalues $\{0.123,\ 0.206,\ 0.293,\ 0.379\}$ — consistent with the 36-projection result to within 0.01. This agreement confirms that the 16-projection set already determines the physical state correctly, and that the additional 20 projections in the 36-projection protocol serve mainly to average out statistical noise rather than to add new information, as discussed in Section 3.6.2.

Diagnosis

The low purity obtained in QST 1 was initially attributed to detector saturation. To test this hypothesis, optical attenuators (10 dB + 5 dB) were inserted at the SPAD inputs and the measurement was repeated; the reconstructed purity remained at the same low level, discarding saturation as the cause. The correct diagnosis — PMD-induced decoherence from the PM fiber inside the fixed U-benches — is discussed in detail in the following Section (5.2.2).

5.2.2 Diagnosis: PMD-induced decoherence

The low purity obtained in QST 1 ($\mathcal{P} = 0.28$), together with the ruling out of detector saturation, pointed towards PMD as the cause of the entanglement degradation. The fixed U-benches used in QST 1 are connected with PM fiber, whose birefringence ($\Delta n_{\text{PM}} \approx 4 \times 10^{-4}$, Section 3.5) is three orders of magnitude larger than that of SMF ($\Delta n_{\text{SMF}} \approx 5 \times 10^{-7}$, Eq. (3.23)). To quantify this effect, the two-photon density matrix evolution under PMD was simulated numerically for PM fiber, whose fixed birefringent axis allows the diagonal Jones matrix of Eq. (3.19) to be applied directly; as discussed in Section 3.5, the same fixed-axis model is not applicable to SMF, whose birefringent axis varies randomly along the fiber length

To illustrate the effect of PMD on a maximally entangled state, an ideal Bell state $|\psi_0\rangle = \frac{1}{\sqrt{2}}(|HH\rangle + |VV\rangle)$ is taken as the initial state $\hat{\rho}_0 = |\psi_0\rangle\langle\psi_0|$. This is not the state actually produced by the EPPS source, but a reference idealization that allows the degradation mechanism to be visualized. The operator $U(\omega)$ is the frequency-dependent Jones matrix of the fiber introduced in Eq. (3.19), evaluated at frequency ω: a birefringent fiber applies a phase $\phi_{H,V}(\omega) = n_{H,V}(\omega)\, L\, \omega/c$ to each polarization component, so that different frequencies acquire different relative phases $\Delta\phi(\omega) = \phi_V(\omega) - \phi_H(\omega)$. Each photon in the pair passes through its own fiber and is therefore acted on by its own copy of $U(\omega)$, which is why the operator $U(\omega) \otimes U(\omega)$ acts on the joint two-photon state. The state is evolved for each frequency component ω of the photon spectrum by applying this operator to both photons:

$$\hat{\rho}(\omega) = \left[U(\omega) \otimes U(\omega)\right] \hat{\rho}_0 \left[U^\dagger(\omega) \otimes U^\dagger(\omega)\right], \tag{5.3}$$

where $U(\omega) = \text{diag}(1,\, e^{i\Delta\phi(\omega)})$ - global phase factored out - and $\Delta\phi(\omega) = \Delta n \cdot L \cdot \omega/c$. The final state is obtained by integrating over the EPPS source spectrum, modeled here by a Gaussian approximation for $S(\omega)$ (25 nm FWHM per photon):

$$\hat{\rho}_{\text{final}} = \int S(\omega)\, \hat{\rho}(\omega)\, d\omega, \tag{5.4}$$

and the purity $\text{Tr}(\hat{\rho}^2_{\text{final}})$ and concurrence $C(\hat{\rho}_{\text{final}})$ are computed for a range of fiber lengths L.

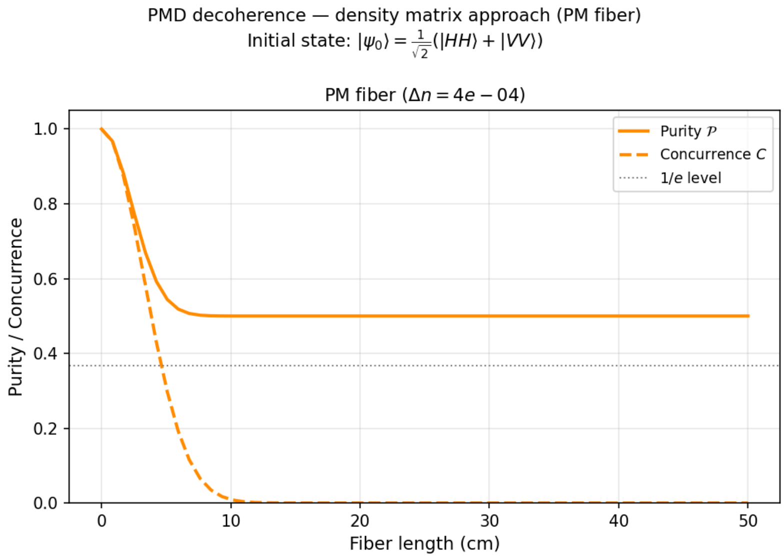

Figure 22: Simulated purity and concurrence of the two-photon state as a function of PM fiber length ($\Delta n_{\mathbf{PM}} = 4 \times 10^{-4}$). Both quantities drop from their maximal values to the fully-mixed level ($\mathcal{P} = 0.5$, $C = 0$) within a few centimetres.

Simulations show that in PM fiber, purity and concurrence drop to fully-mixed values ($\mathcal{P} = 0.5$, $C = 0$) within centimeters. The PM fiber used in the QST 1 setup greatly exceeds this length, explaining the nearly maximally mixed state observed.

Replacing this PM fiber with SMF in QST 4 (Section 5.2.5) removed the dominant source of PMD. As discussed in Section 3.5, this is not only because the residual SMF birefringence is three orders ofmagnitude smaller, but also because its randomly varying orientation prevents the same kind of coherent phase accumulation that destroys entanglement in PM fiber. This is the explanation for the improvement from $\mathcal{P} = 0.28$ in QST 1 to $\mathcal{P} = 0.79$ in QST 4.

5.2.3 QST 2: setup with narrowband filters

Following the diagnosis of PMD-induced decoherence (Section 5.2.2), the first mitigation strategy was to reduce the spectral bandwidth of the photons. Since the coherence length scales as $L_{1/e} = c/(\Delta n \cdot \sigma_\omega)$ (Section 3.5), narrowing σ_ω increases $L_{1/e}$ proportionally, without modifying the fiber infrastructure.

Two narrowband filters were inserted between the EPPS source and the U-benches, one per channel (Section 4.3): a CWDM filter with a passband of ±6.5 nm centred at 1311 nm on one channel, and a Santec OTF-300 with a passband of ±7.5 nm centred at 1320 nm on the other.

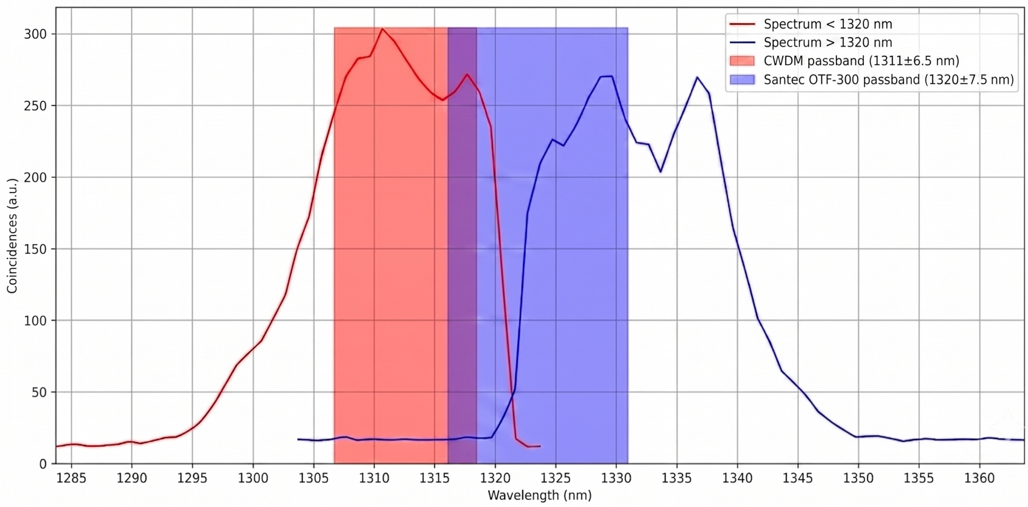

Figure 23: Photon-pair spectrum of the EPPS source with the passbands of the two filters used in QST 2. The shaded regions are the wavelengths each filter lets through; everything else is blocked.

The 36 net coincidence counts, obtained following the protocol of Section 4.4.5, ranged from approximately 2 to 150 counts per projection — significantly lower than in QST 1, as expected given the reduced transmitted bandwidth. The pseudoinverse estimate (Section 3.6.2) resulted in:

$$\hat{\rho}_{\text{pinv}} = \begin{pmatrix} 0.141 & 0.122-0.044i & 0.090-0.081i & 0.076+0.029i \\ 0.122+0.044i & 0.194 & 0.110-0.336i & -0.155+0.091i \\ 0.090+0.081i & 0.110+0.336i & 0.194 & -0.195-0.009i \\ 0.076-0.029i & -0.155-0.091i & -0.195+0.009i & 0.471 \end{pmatrix}, \tag{5.5}$$

with eigenvalues $\{-0.201,\ 0.070,\ 0.343,\ 0.788\}$ and purity $\mathcal{P}_{\text{pinv}} = 0.784$. Unlike QST 1, where the pseudoinverse and MLE results agreed closely, here the pseudoinverse estimate is *not physical*: one eigenvalue is negative, which is impossible for a density matrix. This negative eigenvalue inflates the apparent purity ($\mathcal{P}_{\text{pinv}} = 0.784$) well above the physically achievable value. This is the clearest illustration in this work of why the MLE reconstruction with Cholesky parametrization (Section 3.6.3) is necessary: it enforces positivity and produces the closest physical state consistent with the data. The MLE reconstruction gave:

$$\hat{\rho} = \begin{pmatrix} 0.115 & 0.122-0.021i & 0.039-0.126i & 0.059+0.060i \\ 0.122+0.021i & 0.218 & 0.108-0.191i & -0.122+0.129i \\ 0.039+0.126i & 0.108+0.191i & 0.222 & -0.175-0.017i \\ 0.059-0.060i & -0.122-0.129i & -0.175+0.017i & 0.444 \end{pmatrix}, \tag{5.6}$$

with eigenvalues $\{0.000,\ 0.000,\ 0.268,\ 0.732\}$ and purity $\mathcal{P} = 0.608$. For QST 3 and QST 4, only the MLE result is shown, since this example illustrates that it is the physically meaningful reconstruction.

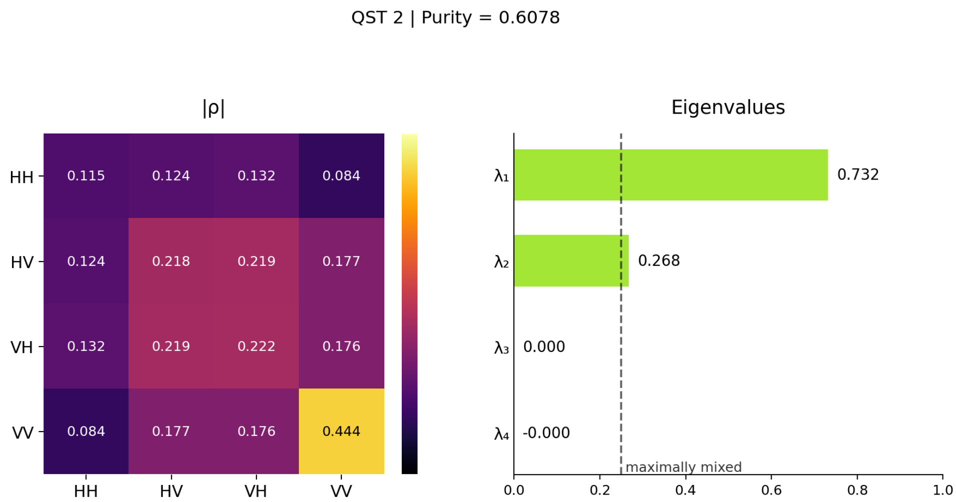

Figure 24: QST 2 reconstructed density matrix (36-projection MLE). Left: magnitude $|\rho|$. Right: eigenvalue spectrum

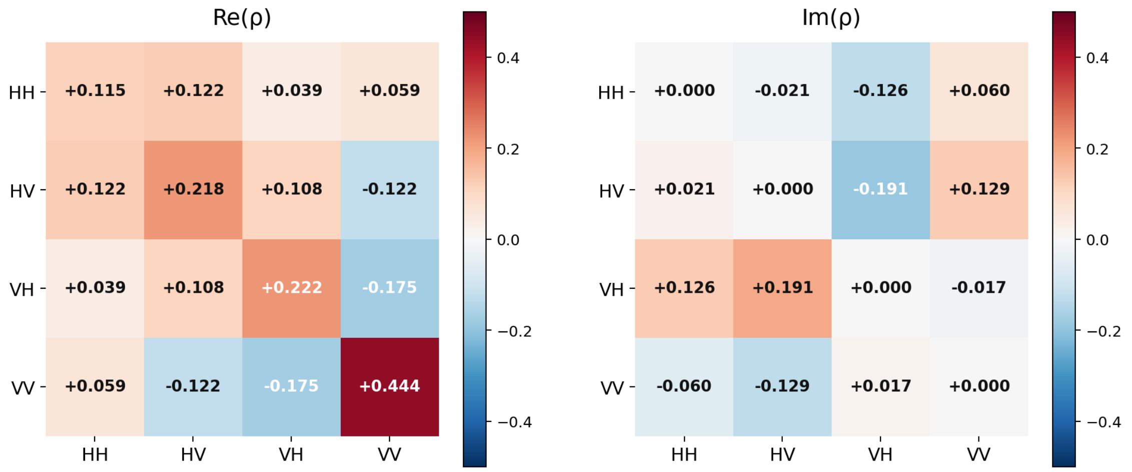

Figure 25: Real and imaginary parts of the QST 2 reconstructed density matrix

The purity improved substantially compared to QST 1 ($\mathcal{P} = 0.28 \rightarrow 0.61$), confirming that reducing the photon bandwidth partially recovers the polarization coherence, as predicted in Section 5.2.2. However, the improvement is limited: two of the four eigenvalues are now zero, indicating that the state has collapsed into a two-dimensional subspace rather than remaining in a fully mixed state, but it is still far from being a pure Bell state (which would have a single eigenvalue equal to 1). The PM fiber of the fixed U-benches remains in the optical path (Section 4.1), so residual PMD continues to limit the purity achievable with this configuration.

5.2.4 QST 3: mechanical stabilisation attempt

The third configuration was optically identical to QST 2, with the same narrowband filters and fixed U-benches, but added mechanical stabilization: the fibers were fixed to the optical table with adhesive tape, and the U-benches were fastened more firmly (Section 4.1.3). The motivation was to reduce perturbations introduced when manually rotating the waveplates between the 36 measurement configurations.

The 36 net coincidence counts, obtained following the protocol of Section 4.4.5 (with the ±300 ps integration window used for QST 3, Section 4.4.5), ranged from approximately 26 to 147 counts per projection. The MLE reconstruction gave:

$$\hat{\rho} = \begin{pmatrix} 0.151 & 0.130 - 0.091i & -0.181 + 0.005i & 0.094 + 0.004i \\ 0.130 + 0.091i & 0.345 & -0.091 - 0.126i & 0.091 + 0.077i \\ -0.181 - 0.005i & -0.091 + 0.126i & 0.385 & -0.100 - 0.026i \\ 0.094 - 0.004i & 0.091 - 0.077i & -0.100 + 0.026i & 0.120 \end{pmatrix}, \tag{5.7}$$

with eigenvalues $\{0.020,\ 0.063,\ 0.224,\ 0.694\}$ and purity $\mathcal{P} = 0.535$.

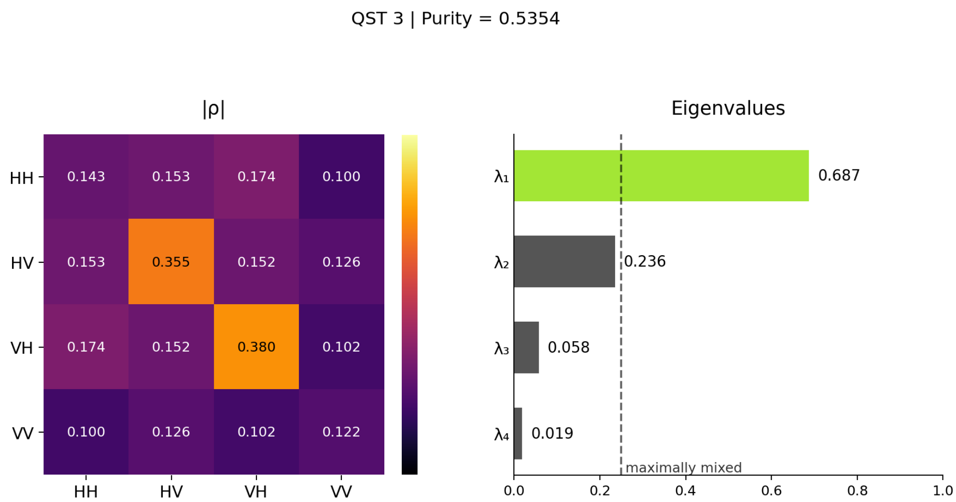

Figure 26: QST 3 reconstructed density matrix (36-projection MLE). Left: magnitude $|\rho|$. Right: eigenvalue spectrum.

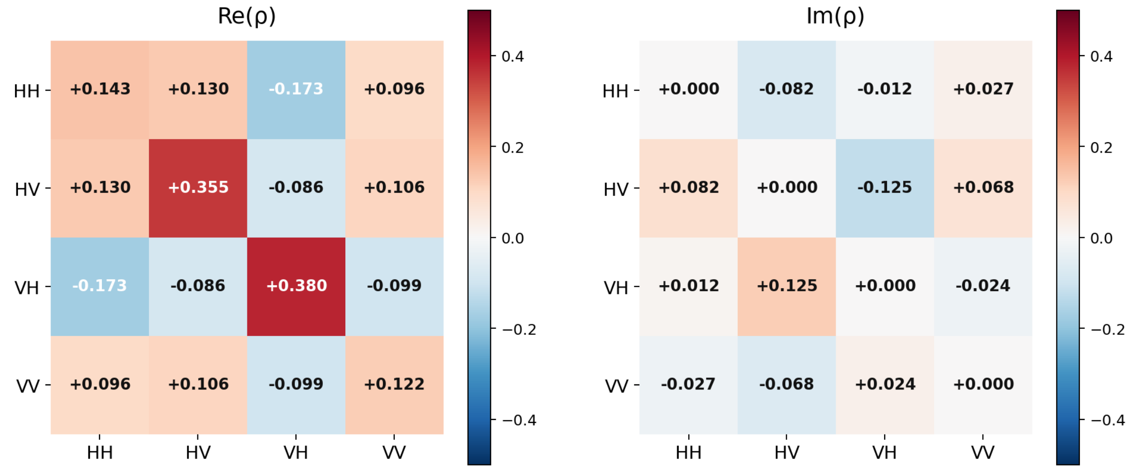

Figure 27: Real and imaginary parts of the QST 3 reconstructed density matrix.

Contrary to expectations, the purity decreased relative to QST 2 ($\mathcal{P} = 0.61 \to 0.54$). Two effects are likely responsible. First, the adhesive tape may apply mechanical stress to the PM fiber, inducing additional birefringence and altering the polarization transformation in an uncontrolled way. Second, the net coincidence counts in QST 3 are comparable to or lower than in QST 2 despite the longer integration time, indicating a reduced coincidence rate that worsens the signal-to-noise ratio and degrades the quality of the tomographic reconstruction. The mechanical stabilization attempt was abandoned and the tape removed (Section 4.1.4).

5.2.5 QST 4: adjustable U-benches with SMF

In the fourth configuration, the fixed U-benches were replaced by adjustable U-benches fitted with SMF connections, eliminating all PM fiber from the optical path; the narrowband filters used in QST 2 and QST 3 were removed (Section 4.1). Following the alignment procedure of Section 4.4.4, the 36 net coincidence counts were obtained with the ±500 ps integration window, ranging from approximately 63 to 997 counts per projection — between one and two orders of magnitude higher than in QST 2–3, reflecting the elimination of the narrowband filters and the improved overall performance of the SMF path.

The MLE reconstruction gave:

$$\hat{\rho} = \begin{pmatrix} 0.258 & -0.188 + 0.126i & -0.075 + 0.214i & 0.164 + 0.154i \\ -0.188 - 0.126i & 0.261 & 0.157 - 0.160i & -0.052 - 0.153i \\ -0.075 - 0.214i & 0.157 + 0.160i & 0.244 & 0.040 - 0.194i \\ 0.164 - 0.154i & -0.052 + 0.153i & 0.040 + 0.194i & 0.237 \end{pmatrix}, \tag{5.8}$$

with eigenvalues $\{0.000,\ 0.010,\ 0.109,\ 0.881\}$ and purity $\mathcal{P} = 0.789$.

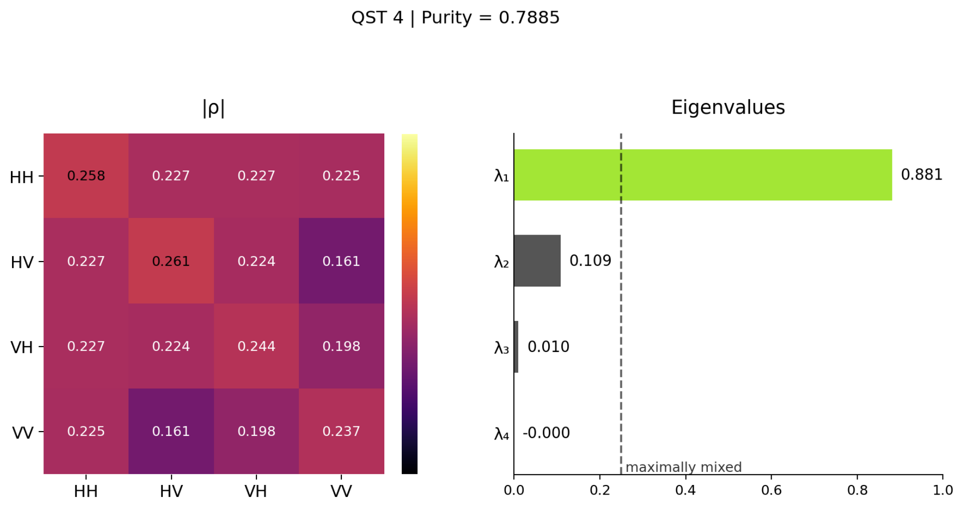

Figure 28: QST 4 reconstructed density matrix (36-projection MLE). Left: magnitude $|\rho|$. Right: eigenvalue spectrum. A single eigenvalue dominates the spectrum, close to the value of 1 expected for a pure state.

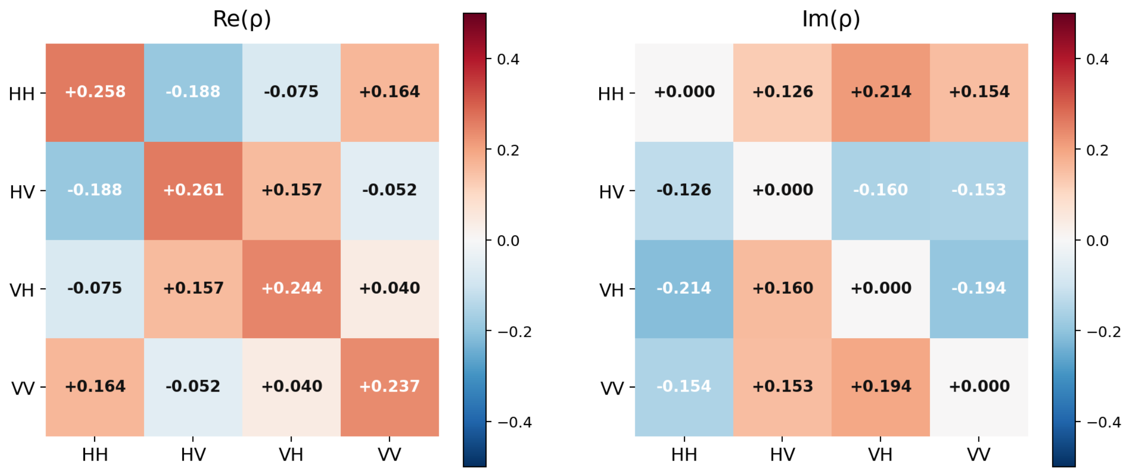

Figure 29: Real and imaginary parts of the QST 4 reconstructed density matrix.

The eigenvalue spectrum is now dominated by a single eigenvalue close to 1 ($\lambda_1 = 0.881$), with the remaining three eigenvalues close to zero — nearly pure state. The purity reached $\mathcal{P} = 0.789$, the highest value obtained in the local characterization, confirming the diagnosis of Section 5.2.2: eliminating the PM fiber from the optical path removes the dominant source of PMD, and the residual SMF birefringence is minimal over the lengths involved. This configuration was used as the reference setup for the entanglement metrics analysis (Section 5.4) and the distribution experiment (Section 5.5).

5.3 Angular error analysis (Monte Carlo ±1°)

The QST protocol described in Section 4.4 requires setting the HWP and QWP in each arm to a specific angle for each of the 36 measurement configurations. The angle of the waveplates is rotated manually, so each setting carries a small mechanical error. Therefore, it is logical to think: how much do these angular imperfections affect the reconstructed density matrix and the derived entanglement metrics?

To answer this, a parametric Monte Carlo simulation was implemented, taking the result of QST 4 (Section 5.2.5) as the reference state $\hat{\rho}_{\text{ref}}$ (purity $\mathcal{P} = 0.7885$). The simulation repeats the full reconstruction $N = 500$ times, each time with possible angular errors, and collects the distribution of the output metrics. Since the errors originate from the projectors and not from the state, there is a definite expression for the resulting uncertainty; the Monte Carlo method is the most appropriate approach. [34, 10, 11].

Step 1 — Measurement model and Jones formalism.

Each measurement arm consists of a QWP and a HWP followed by a polarizer and a SPAD (Figure 30). The polarizer defines the measurement basis: the transmitted port selects $|V\rangle$. In the Jones formalism, a photon with linear polarization oriented at an angle θ with respect to the transmission axis is described by the two-component vector [13]

$$|\theta\rangle = \begin{pmatrix} \cos\theta \\ \sin\theta \end{pmatrix}, \tag{5.9}$$

where, by the convention adopted throughout this work, $\theta = 0$ corresponds to $|V\rangle$. The polariser projector at angle θ_{pol} is

$$\hat{\Pi}_{\text{pol}}(\theta_{\text{pol}}) = |\theta_{\text{pol}}\rangle \langle\theta_{\text{pol}}| = \begin{pmatrix} \cos^2\theta_{\text{pol}} & \sin\theta_{\text{pol}}\cos\theta_{\text{pol}} \\ \sin\theta_{\text{pol}}\cos\theta_{\text{pol}} & \sin^2\theta_{\text{pol}} \end{pmatrix}, \tag{5.10}$$

so that at its nominal setting ($\theta_{\text{pol}} = 0$) it projects onto $|V\rangle$. The Jones matrices of the two retardation plates at angle θ are

$$U_{\text{HWP}}(\theta) = \begin{pmatrix} \cos 2\theta & \sin 2\theta \\ \sin 2\theta & -\cos 2\theta \end{pmatrix}, \quad U_{\text{QWP}}(\theta) = \begin{pmatrix} \cos^2\theta - i\sin^2\theta & (1+i)\sin\theta\cos\theta \\ (1+i)\sin\theta\cos\theta & \sin^2\theta - i\cos^2\theta \end{pmatrix}. \tag{5.11}$$

The waveplate U rotates the incoming state so that the desired polarisation is aligned with the polarizer transmission axis. Defining the measurement vector as $M = U^\dagger |pol\rangle$, where $|pol\rangle = (1,0)^T$ is the polarizer reference state, the single-photon projector is

$$\hat{\Pi} = M\,M^\dagger = U^\dagger |pol\rangle \langle pol|\, U = U^\dagger\, \hat{\Pi}_{\text{pol}}\, U. \tag{5.12}$$

Table 12 lists the six nominal waveplate settings used in the tomographic protocol.

Table 12: Nominal waveplate settings for each single-photon projection in one arm of the QST setup. For state $|V\rangle$ no waveplate is inserted. Abbreviations: $U_H \equiv U_{\mathbf{HWP}}$, $U_Q \equiv U_{\mathbf{QWP}}$, $\hat{\Pi}_0 \equiv \hat{\Pi}_{\mathbf{pol}}(0^\circ) = |V\rangle\langle V|$.

State	Element	Nominal angle	Nominal projector
$\|V\rangle$	—	—	$\hat{\Pi}_0$
$\|H\rangle$	HWP	45.0°	$U_H^\dagger(45^\circ)\,\hat{\Pi}_0\,U_H(45^\circ)$
$\|D\rangle$	HWP	22.5°	$U_H^\dagger(22.5^\circ)\,\hat{\Pi}_0\,U_H(22.5^\circ)$
$\|A\rangle$	HWP	−22.5°	$U_H^\dagger(-22.5^\circ)\,\hat{\Pi}_0\,U_H(-22.5^\circ)$
$\|R\rangle$	QWP	−45.0°	$U_Q^\dagger(-45^\circ)\,\hat{\Pi}_0\,U_Q(-45^\circ)$
$\|L\rangle$	QWP	45.0°	$U_Q^\dagger(45^\circ)\,\hat{\Pi}_0\,U_Q(45^\circ)$

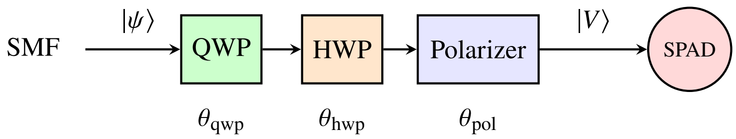

Figure 30: Single-arm polarisation analysis module. The photon from the SMF fiber passes through the QWP and HWP (manual adjustment) and is transmitted by the linear polarizer, also manually adjusted. The polarizer transmits the polarisation component aligned with its axis ($|V\rangle$ at $\theta_{\mathbf{pol}} = 0$). The transmitted photon is detected by the SPAD. All three optical elements introduce independent angular errors, modelled as $\delta \sim \mathcal{N}(0^\circ, 1^\circ)$.

When an angular error is present, the *real* single-photon projector for a waveplate at nominal angle θ, a waveplate error δ_{wp}, and a polariser error δ_{pol} is

$$\boxed{\hat{\Pi}^{(\text{real})} = U^\dagger(\theta + \delta_{\text{wp}})\,\hat{\Pi}_{\text{pol}}(\delta_{\text{pol}})\,U(\theta + \delta_{\text{wp}}).} \tag{5.13}$$

As a concrete example, for the $|H\rangle$ projection in arm A:

$$\hat{\Pi}_H^{A,(\text{real})} = U_{\text{HWP}}^\dagger\big(45^\circ + \delta_{\text{HWP}}^A\big)\,\hat{\Pi}_{\text{pol}}\big(\delta_{\text{pol}}^A\big)\,U_{\text{HWP}}\big(45^\circ + \delta_{\text{HWP}}^A\big). \tag{5.14}$$

For a joint two-photon configuration (i, j), the combined projector is the tensor product of the two single-photon projectors:

$$\hat{\Pi}_{i,j}^{(\text{real})} = \hat{\Pi}_i^{A,(\text{real})} \otimes \hat{\Pi}_j^{B,(\text{real})}, \tag{5.15}$$

a 4×4 operator acting on the joint polarisation space of both photons.

Step 2 — Error model.

There are two physically different types of angular error.

The *polariser error* is set once at the start of the experimental session and is the same for all 36 measurements within that session:

$$\delta^A_{\text{pol}} \sim \mathcal{N}(0, 1^\circ), \qquad \delta^B_{\text{pol}} \sim \mathcal{N}(0, 1^\circ). \tag{5.16}$$

The *waveplate error* is introduced each time a plate is manually rotated to a new position; since each of the 36 configurations requires an independent adjustment, these errors are uncorrelated across measurements. For configuration k:

$$\delta^{A,k}_{\text{HWP}},\ \delta^{B,k}_{\text{HWP}},\ \delta^{A,k}_{\text{QWP}},\ \delta^{B,k}_{\text{QWP}} \ \sim\ \mathcal{N}(0, 1^\circ), \quad \text{all independent.} \tag{5.17}$$

The Gaussian distribution is preferred over a uniform $\mathcal{U}(-1^\circ, 1^\circ)$ to represent the angular errors. In error propagation, a Gaussian distribution is the standard choice because it better models physical reality; mechanical errors naturally tend to cluster around zero rather than spreading evenly. Figure 31 illustrates the Gaussian distribution with zero mean and a standard deviation of 1°.

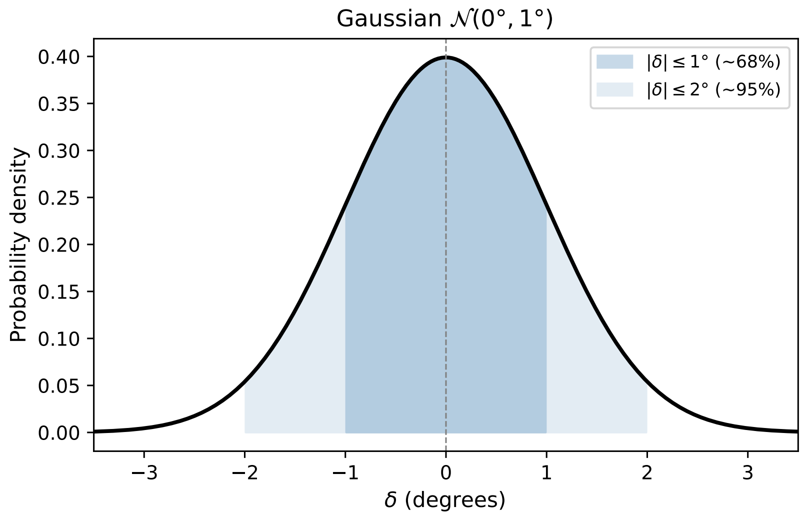

Figure 31: Candidate distributions for the angular error δ (degrees). Gaussian $\mathcal{N}(0^\circ, 1^\circ)$, adopted in this analysis; approximately 68% of draws fall within $\pm 1^\circ$. The Gaussian better models the behaviour of a manually positioned rotation stage, whose error tends to concentrate near zero.

Step 3 — Simulation procedure.

Each Monte Carlo iteration follows five steps.

1. **Draw errors.** Sample a set of errors according to Equations (5.16)–(5.17).
2. **Build real projectors.** Construct all 36 single-photon real projectors via Eq. (5.13) and assemble the 36 two-photon projectors via Eq. (5.15).
3. **Compute expected counts.** For each configuration k, the probability of a coincidence given the reference state and the perturbed projectors is

$$P^{(\text{real})}_k = \text{Tr}\big(\hat{\rho}_{\text{ref}}\, \hat{\Pi}^{(\text{real})}_k\big). \tag{5.18}$$

The expected coincidence count is $\mu_k = N_{\text{total}} \cdot P_k^{(\text{real})}$.

4. **Add Poisson shot noise.** The simulated count is drawn as

$$n_k^{(\text{sim})} \sim \text{Poisson}(\mu_k). \tag{5.19}$$

This step is essential: without it the simulation would model a noiseless experiment, which is unrealistic.

5. **Reconstruct with nominal projectors.** The simulated counts $n_k^{(\text{sim})}$ are passed to the MLE algorithm (Section 3.6.3) using the *nominal* projectors $\hat{\Pi}_k^{(\text{nom})}$ — the same projectors used in the real laboratory, which has no knowledge of the actual angular errors.

The loop is repeated for $N = 500$ iterations and the distribution of the reconstructed purity and all entanglement metrics is recorded.

Step 4 — Step 4: Systematic bias due to a lack of consistency between projectors.

The most important outcome of the simulation is a *systematic* downward bias in the reconstructed purity. The mechanism is as follows.

In the laboratory, $\hat{\rho}$ is reconstructed using the nominal projectors, with no knowledge of the actual angular errors. The MLE searches for the matrix $\hat{\rho}$ that best explains the measured counts by minimising

$$f(\hat{\rho}) = \sum_{k=1}^{36} \Big[\underbrace{N_{\text{total}}\ \text{Tr}\big(\hat{\rho}\, \hat{\Pi}_k^{(\text{nom})}\big)}_{\mu_k^{(\text{nom})}} - n_k^{(\text{sim})}\ \ln \mu_k(\hat{\rho}) \Big]. \tag{5.20}$$

The problem is the following. The simulated counts $n_k^{(\text{sim})}$ were generated with the real projectors $\hat{\Pi}_k^{(\text{real})}$, which include angular errors. The MLE tries to explain those counts using the nominal projectors $\hat{\Pi}_k^{(\text{nom})}$, which assume perfect angles. Since $\hat{\Pi}_k^{(\text{real})} \neq \hat{\Pi}_k^{(\text{nom})}$, the predictions with the reference state $\hat{\rho}_{\text{ref}}$ do not match the data:

$$N_{\text{total}}\ \text{Tr}\big(\hat{\rho}_{\text{ref}}\, \hat{\Pi}_k^{(\text{nom})}\big) \neq n_k^{(\text{sim})}. \tag{5.21}$$

The MLE sees this discrepancy and concludes that $\hat{\rho}_{\text{ref}}$ is not the correct state. The physical effect of angular errors is to balance the distribution of counts: projections whose angular error increases their overlap with the real state register more counts than expected, while those whose error decreases it register fewer. The MLE interprets this levelling as evidence of a more mixed state and returns a slightly more mixed $\hat{\rho}$ that better fits the displaced data. The reconstructed purity is consistently *lower* than the true purity, and this is the way we measure how much the angular error disturbs the ideal and real results.

Results.

Figure 32 shows the distribution of the reconstructed purity over 500 iterations. Table 13 summarises the quantitative results.

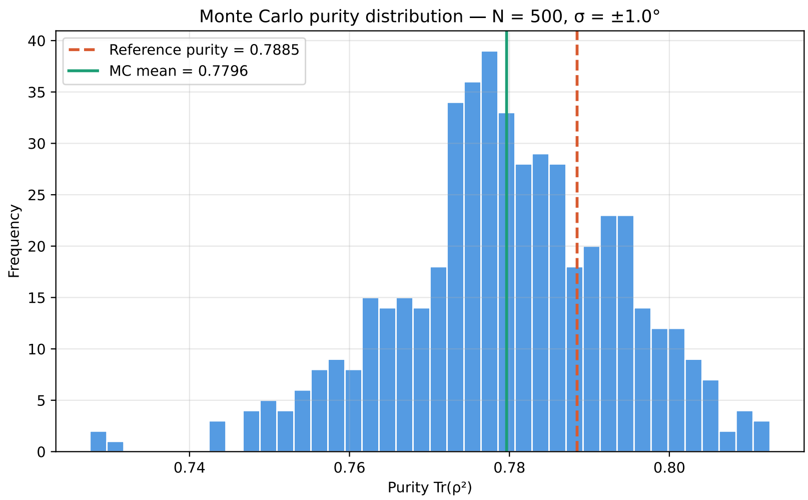

Figure 32: Monte Carlo distribution of the reconstructed purity $\mathcal{P} = \mathrm{Tr}(\hat{\rho}^2)$ over $N = 500$ iterations with angular errors $\sigma = \pm 1^\circ$. The red dashed line marks the reference purity ($\mathcal{P}_{\mathbf{ref}} = 0.7885$); the green solid line marks the Monte Carlo mean ($\bar{\mathcal{P}} = 0.7796$). The leftward offset between the two lines is the bias described in this section, caused by the mismatch between nominal and real projectors.

Table 13: Monte Carlo results for the angular error analysis ($N = 500$ iterations, $\sigma = \pm 1^\circ$, Gaussian errors). The systematic bias equals $\bar{\mathcal{P}} - \mathcal{P}_{\mathbf{ref}}$.

Quantity	Reference	MC mean	Std	95% CI
Purity $\mathrm{Tr}(\hat{\rho}^2)$	0.7885	0.7796	0.0141	[0.7505, 0.8050]
Systematic bias $\Delta\mathcal{P}$	−0.0088	—	—	—
λ_1	0.8812	0.8761	0.0085	—
λ_2	0.1088	0.1075	0.0093	—
λ_3	0.0100	0.0156	0.0093	—
λ_4	0.0000	0.0007	0.0023	—

The dominant eigenvalue $\lambda_1 = 0.8812$ is highly robust ($\sigma = 0.0085$), confirming that the entangled character of the state is unaffected by the angular errors. The two minor eigenvalues λ_3 and λ_4 show larger relative uncertainty, but their absolute values are small enough that this has no impact on the physical conclusions.

The 95% confidence interval $\mathcal{P} \in [0.7505, \ 0.8050]$ contains the reference value, and its total width (≈ 0.055) gives the full range of purity variation under $\pm 1^\circ$ angular error.

Angular errors of $\pm 1^\circ$ introduce an uncertainty of $\sigma_{\mathcal{P}} = 0.014$ and a systematic bias of -0.009 in the reconstructed purity. Both figures are small compared to the improvements observed between successive experimental configurations, confirming that the results are physically significant and not dominated by mechanical calibration errors.

The uncertainty estimates obtained here apply to all entanglement metrics: the ± values and confidence intervals presented in section 5.4 are obtained by applying the same Monte Carlo protocol to each metric independently.

5.4 Entanglement metrics

The full set of entanglement metrics defined in Section 3.7 was computed for the QST 4 reconstructed state ($\hat{\rho}$, purity $\mathcal{P} = 0.7885$), the reference configuration used for the source characterization. The metric uncertainties were obtained from the same Monte Carlo simulation described in the previous section ($N = 500$ realizations, $\pm 1^\circ$ angular errors), applied independently to each metric.

Table 14: Entanglement metrics for the QST 4 reconstructed state, with Monte Carlo uncertainties ($N = 500$, $\pm 1^\circ$). The Range column gives the theoretical range of each metric, with the value indicating maximal entanglement underlined.

Metric	Range	Reference	MC mean ± std	95% CI
Purity $\mathrm{Tr}(\hat{\rho}^2)$	$[0.25, \underline{1}]$	0.7885	0.7796 ± 0.0141	$[0.7505, 0.8050]$
Purity of $\hat{\rho}_A$	$[\underline{0.5}, 1]$	0.5406	$- \pm 0.0066$	$[0.5289, 0.5543]$
Von Neumann entropy $S(\hat{\rho}_A)$ [bits]	$[0, \underline{1}]$	0.9406	0.9397 ± 0.0098	$[0.9202, 0.9578]$
Concurrence C	$[0, \underline{1}]$	0.7356	0.7260 ± 0.0194	$[0.6844, 0.7603]$
Entanglement of formation E_F [ebits]	$[0, \underline{1}]$	0.6374	0.6251 ± 0.0249	$[0.5722, 0.6695]$
Negativity $\mathcal{N}$	$[0, \underline{0.5}]$	0.3551	0.3498 ± 0.0091	$[0.3325, 0.3666]$
Log-negativity $E_{\mathcal{N}}$	$[0, \underline{1}]$	0.7742	0.7650 ± 0.0155	$[0.7355, 0.7934]$
Fidelity to $\lvert\Phi^+\rangle$	$[0, \underline{1}]$	0.4116	0.4162 ± 0.0084	$[0.4001, 0.4319]$
Fidelity to closest pure state $F_{\max}$	$[0, \underline{1}]$	0.8812	—	—
Werner parameter p (optimal state)	$[0, \underline{1}]$	0.8416	—	—

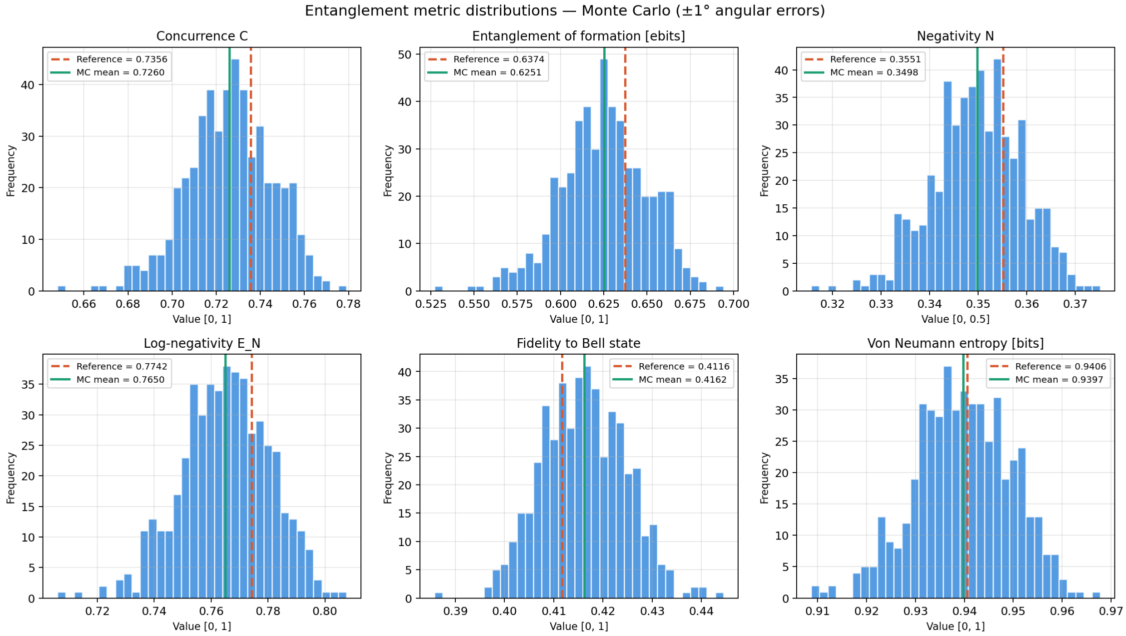

Figure 33: Monte Carlo distributions of the entanglement metrics for the QST 4 state, over $N = 500$ realizations with $\pm 1^\circ$ angular errors. The dashed line marks the reference value; the solid line marks the Monte Carlo mean. All distributions are unimodal and approximately centred on the reference value, consistent with the small systematic biases discussed in Section 5.3.

The concurrence $C = 0.74$ and entanglement of formation $E_F = 0.64$ ebits indicate substantial entanglement, consistent with the purity result. The von Neumann entropy of the reduced state $S(\hat{\rho}_A) = 0.94$ bits is close to the maximum of 1 bit for a Bell state, confirming that the marginal state of each photon is close to maximally mixed — the signature of strong bipartite entanglement.

The fidelity to the standard Bell state $|\Phi^+\rangle$ is only $F = 0.41$, which might suggest weak entanglement if interpreted in isolation. However, the fidelity to the *closest pure state* (the dominant eigenvector of $\hat{\rho}$) is $F_{\max} = \lambda_1 = 0.8812$ — more than twice as large. This large difference indicates that the reconstructed state is not close to $|\Phi^+\rangle$ specifically, but — as confirmed below by the near-uniform populations of $|\psi_{\text{opt}}\rangle$ — is close to *some* maximally entangled pure state. The Werner-state fit confirms this: fitting $\hat{\rho}$ to a Werner state built from $|\Phi^+\rangle$ gives a poor parameter $p = 0.22$, while fitting it to a Werner state built from the optimal pure state (the dominant eigenvector) gives $p = 0.84$, with predicted purity, concurrence, and fidelity all matching the measured values closely.

Identifying the source state

The dominant eigenvector $|\psi_{\text{opt}}\rangle$ accounts for 88% of the reconstructed state and has populations in the $\{H, V\}$ basis of $\{0.283,\ 0.247,\ 0.256,\ 0.215\}$ for $\{|HH\rangle, |HV\rangle, |VH\rangle, |VV\rangle\}$ — all close to 0.25, the signature of a maximally entangled state. Decomposing $|\psi_{\text{opt}}\rangle$ in the Bell basis gives

$$|\psi_{\text{opt}}\rangle \approx (-0.632{+}0.205i)\,|\Phi^+\rangle{+}(-0.120{-}0.205i)\,|\Phi^-\rangle{+}(0.425{+}0.513i)\,|\Psi^+\rangle{+}(0.183{-}0.160i)\,|\Psi^-\rangle, \tag{5.22}$$

with Bell-state probabilities $\{0.441,\ 0.056,\ 0.444,\ 0.059\}$. The dominant eigenvector is therefore essentially

$$|\psi_{\text{opt}}\rangle \approx \alpha\,|\Phi^+\rangle + \beta\,|\Psi^+\rangle, \qquad |\alpha|^2 \approx |\beta|^2 \approx 0.44, \tag{5.23}$$

with distinct complex phases for α and β. This is consistent with a maximally entangled state that has been rotated away from the standard $\{H, V\}$ basis — for instance by a polarization rotation introduced by the U-bench collimators or the SMF fiber — rather than with a partially entangled or mixed source state. The source itself appears to produce a genuinely strong, near-maximally entangled state; the purity measured in QST 4 ($\mathcal{P} = 0.79$) reflects experimental imperfections (residual PMD, alignment, detector noise) acting on that state, not a fundamental limitation of the source.

The full eigendecomposition $\hat{\rho} = \sum_i \lambda_i\,|\psi_i\rangle\langle\psi_i|$ shows that all eigenvector with a significant weight have high concurrence, indicating that the loss of purity follows a definite structure rather than a random mixture of separable contributions. The complete decomposition, including the Bell-basis representation of each eigenvector, is given in Appendix A.

5.5 Distribution and comparison with theoretical predictions

The polarization characterization presented in Sections 5.2–5.4 establishes that the EPPS source produces a genuinely strong, near-maximally entangled state. In this part of the project, records only the time-correlated coincidences between the two photons after they have traveled through the building's fiber infrastructure. This is consistent with the scope of this work: polarization characterization demonstrates that the photon pairs are entangled in polarization, and not only in time, which is the property required by polarization-based applications such as quantum key distribution or entanglement-based teleportation. Implementing and operating such a polarization-based distribution link is left as a direction for future work (Section 6.4). The present distribution experiment establishes the time-correlation baseline over the full inter-laboratory link, using the SMF configuration validated in QST 4.

5.5.1 Distribution setup and fiber infrastructure

The distribution experiment uses the fiber infrastructure and architecture described in Section 4.2: the EPPS source in Laboratory 1 sends both photon channels through three passive patch panels (Laboratory 1, sixth floor, Laboratory 2), looping back at Laboratory 2 and returning to the SPAD detectors in Laboratory 1, for a total OTDR-measured path of 738 m (Figure 14). The SMF adjustable U-bench configuration of QST 4 (Section 5.2.5) was used, with 9 dB attenuators at each SPAD input (Section 4.3). A direct-connection reference measurement, using the same attenuators and a short SMF cable between source and detectors, was performed immediately before the distribution measurement to provide a baseline under identical detector conditions.

5.5.2 Loss characterization

The insertion loss of the two fiber channels was characterized with two independent methods: an OTDR trace at 1310 nm, and a direct power measurement using the IDPhotonics CoBrite DX4 tunable laser (1550 nm) and the Thorlabs PM100A power meter, with a reference power of $F_{\text{ref}} = 3.18\,\text{mW}$ measured through a short (2–3 m) SMF reference cable.

Table 15: Insertion loss for the two distribution channels, from OTDR (1310 nm) and power meter (1550 nm) measurements. η is the transmission efficiency.

	Channel 1	Channel 2	
OTDR span length	737.6 m	739.8 m	
OTDR total loss	4.145 dB	2.982 dB	(η = 0.385 / 0.503)
Fiber attenuation	0.572 dB	0.275 dB	
Connector losses	3.573 dB (3 events)	2.707 dB (5 events)	
Power meter total loss	4.055 dB	2.849 dB	(η = 0.393 / 0.519)

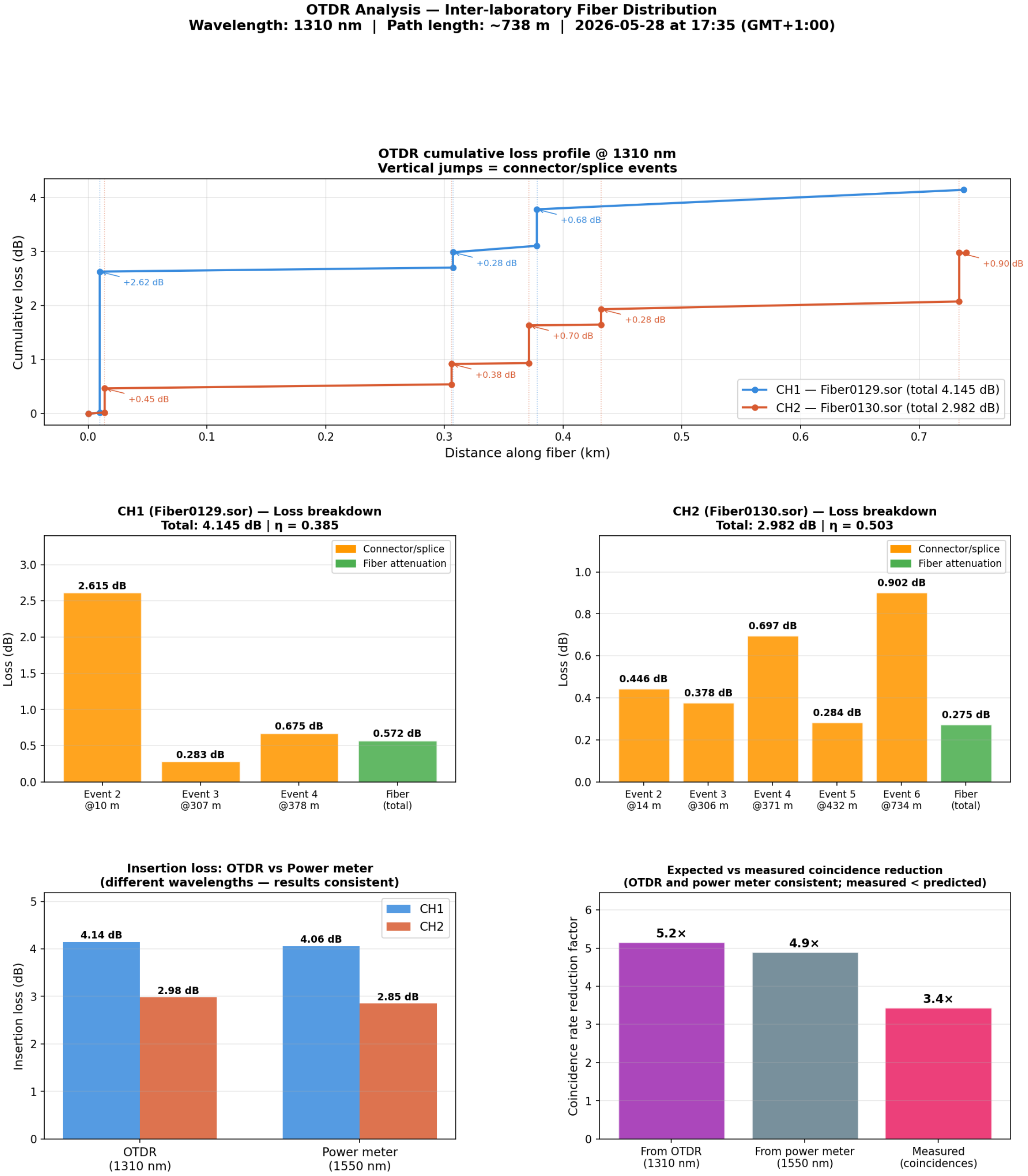

Figure 34: OTDR cumulative loss profile at 1310 nm for the two distribution channels (top), with the corresponding loss breakdown into connector/splice events and fiber attenuation (bottom left and centre), and a comparison between OTDR- and power-meter-derived insertion losses (bottom right).

The OTDR and power meter measurements agree closely for both channels (4.145 dB vs 4.055 dB for Channel 1; 2.982 dB vs 2.849 dB for Channel 2), which supports the reliability of both measurements.

The loss profile of Channel 2 (Figure 34, top) maps cleanly onto the physical route: five connector events are visible, corresponding to the patch panel in Laboratory 1, the sixth-floor patch panel (outbound), the loopback connection at Laboratory 2, the sixth-floor patch panel (return), and the patch panel in Laboratory 1 (return). The largest single event (0.902 dB at 734 m) occurs near the end of the return path. Channel 1, by contrast, shows only three events, dominated by a single very large jump (2.615 dB) within the first 10 m of fiber. This is consistent with a poorly-mated or partially damaged connector in the short segment near the source (Section 4.2); the remaining two events on Channel 1 are broadly consistent with two of the five events seen on Channel 2, but the OTDR trace does not resolve the full set of connector events on this channel. The total loss value for Channel 1 is nevertheless considered reliable, since it agrees closely with the independent power meter measurement (4.145 dB vs 4.055 dB); what remains uncertain is only the precise distribution of that loss among the individual connectors along the route. A repeated OTDR measurement could clarify this distribution, but was not available within the time frame of this work

From the total transmission efficiencies η_1 and η_2, the expected reduction in coincidence rate relative to the direct-connection reference is $\eta_1 \cdot \eta_2$, since both photons of each pair must traverse the full link to be detected in coincidence:

$$\eta_1\eta_2\big|_{\text{OTDR}} = 0.385 \times 0.503 = 0.194 \quad (5.2\times \text{ reduction}), \tag{5.24}$$

$$\eta_1\eta_2\big|_{\text{power meter}} = 0.393 \times 0.519 = 0.204 \quad (4.9\times \text{ reduction}). \tag{5.25}$$

These two independent estimates of the expected coincidence reduction agree closely with each other (5.2× and 4.9×), providing a theoretical prediction against which the measured coincidence reduction is compared in the following section.

5.5.3 Coincidence rates and histogram comparison

A second source characterization, identical in procedure to that of Section 5.1 but using 9 dB attenuators (matching the distribution measurement), was performed immediately before the distribution measurement to serve as the direct-connection reference. The single-channel rates were $\bar{R}_3 = 72\,619 \pm 303$ counts/s and $\bar{R}_4 = 76\,407 \pm 282$ counts/s, with a coincidence rate of 100.1 ± 12.6 counts/s (CAR = 14.2, ±0.5 ns window).

The distribution measurement gave $\bar{R}_3 = 47\,076 \pm 1890$ counts/s and $\bar{R}_4 = 62\,243 \pm 1592$ counts/s, with a coincidence rate of 29.0 ± 7.9 counts/s (CAR = 7.7, ±0.5 ns window).

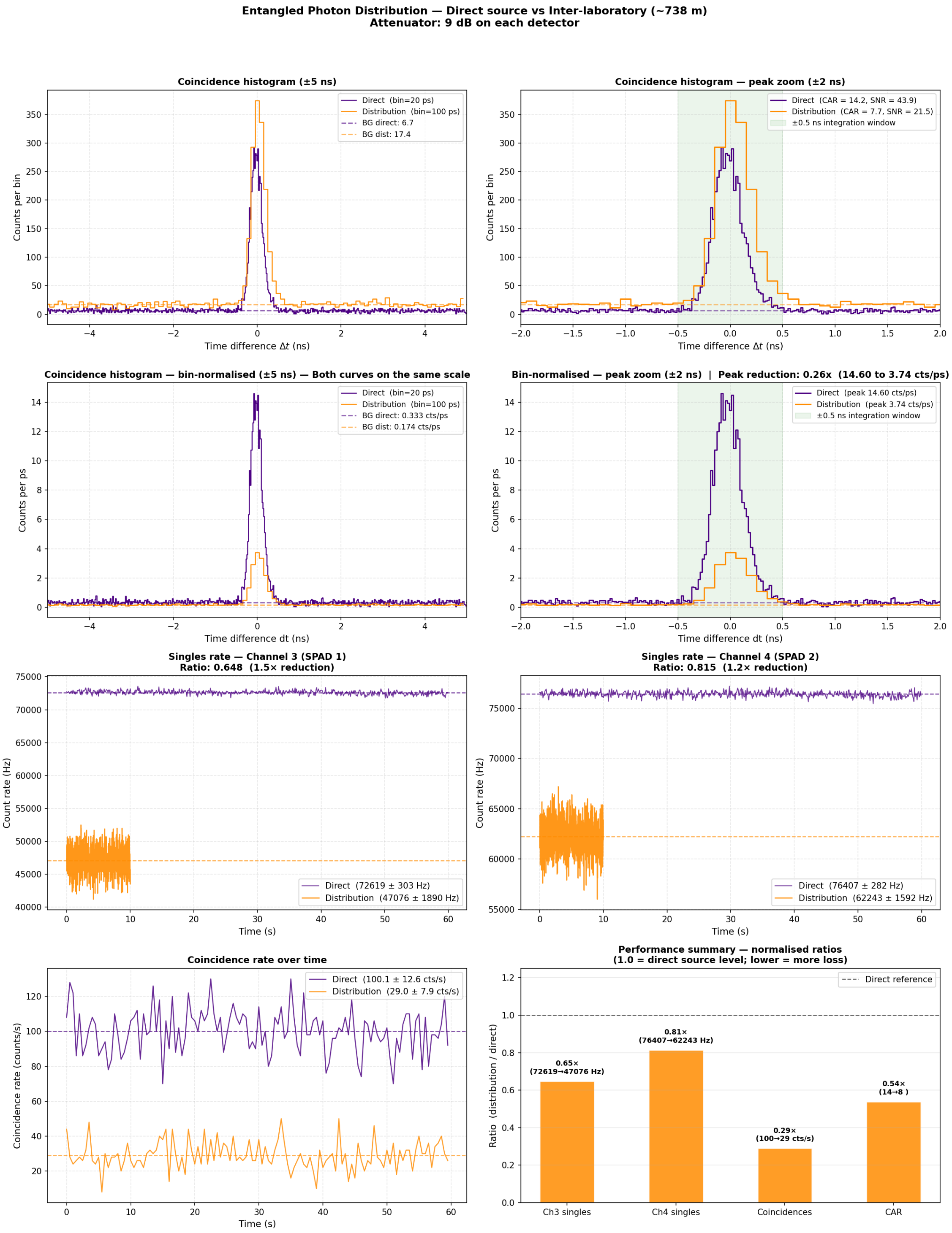

Figure 35: Comparison between the direct-connection reference and the inter-laboratory distribution (738 m)**, both with** 9 dB **attenuators**

Table 16: Comparison between direct-connection reference and distribution (738 m)**,** 9 dB **attenuation.**

Quantity	Direct	Distribution	Ratio
Channel 3 singles	72 619 ± 303 counts/s	47 076 ± 1890 counts/s	0.648
Channel 4 singles	76 407 ± 282 counts/s	62 243 ± 1592 counts/s	0.815
Coincidence rate	100.1 ± 12.6 counts/s	29.0 ± 7.9 counts/s	0.290
CAR	14.2	7.7	0.54

The measured coincidence rate reduction is 0.290, corresponding to a 3.5× reduction — smaller than the 5.2× and 4.9× reductions predicted from the OTDR and power meter insertion loss measurements in Section 5.5.2. The single-channel reductions (0.648 for channel 3, 0.815 for channel 4) are also smaller than the individually-measured channel efficiencies (η_1 = 0.385–0.393, η_2 = 0.503–0.519) would suggest. The origin of this discrepancy was discussed; a possible contributing factor is detector saturation effects under the higher count rates of the direct-connection reference, although this was not investigated further within the scope of this work. The CAR also decreased from 14.2 to 7.7, reflecting the increased relative background contribution at the lower signal level after the 738 m link.

Chapter 6.

Conclusions and future work

6.1 Conclusions

The general objective of this thesis was to characterize and distribute pairs of entangled photons through the optical fiber infrastructure connecting two laboratories at CTU (Section 2.1). Within this general objective, we proposed specific objectives, all of which have been well achieved.

The work began with the characterization of the detectors and the source (Section 5.1): the two SPAD detectors with the most similar dark count rates were selected, and the EPPS source was confirmed to operate as expected, producing a bright photon-pair flux with low accidental background (SNR = 32.9, CAR = 11.4), consistent with the values reported in the manufacturer's specifications.

The central challenge of this work emerged in the first QST measurement (Section 5.2.1), which yielded a purity of only $\mathcal{P} = 0.28$ — far below the entanglement expected from the source. Diagnosing the cause of this degradation required applying the polarization mode dispersion framework introduced in Section 3.5, which identified the PM fiber inside the fixed U-benches as the source of the problem: its large birefringence, combined with the broadband spectrum of the EPPS source, destroys polarization coherence within centimeters. Two intermediate mitigation attempts — narrowband spectral filtering (QST 2, $\mathcal{P} = 0.61$) and mechanical stabilization of the fiber (QST 3, $\mathcal{P} = 0.53$) — achieved only a partial or inconsistent improvement, confirming that the filters alone could not fully compensate for the PMD introduced by the fiber. Replacing the PM fiber with SMF-fiber-coupled adjustable U-benches in QST 4 resolved the problem directly, raising the purity to $\mathcal{P} = 0.79$ and validating the diagnosis quantitatively.

The full set of entanglement metrics computed for the QST 4 state (Section 5.4) showed that the dominant eigenvector of the reconstructed density matrix corresponds to a near-maximally entangled state, expressed as an almost equal superposition of $|\Phi^+\rangle$ and $|\Psi^+\rangle$. This indicates that the EPPS source itself produces a genuinely strong entangled state, and that the moderate purity measured experimentally reflects a rotation away from the standard $\{H, V\}$ basis together with residual experimental imperfections, rather than a fundamental limitation of the source.

Finally, the SMF configuration validated in QST 4 was used to distribute the entangled photon pairs over a 738 m inter-laboratory link (Section 5.5). The measured coincidence rate reduction (3.5×) was smaller than predicted from independent OTDR and power meter insertion-loss measurements

(5.2× and 4.9× respectively), The most likely explanation is that in the direct-connection reference measurement, the EPPS was saturating the detector: the attenuation used may not have been sufficient to keep the SPAD detectors in their linear regime, making the reference coincidence rate appear lower than it actually was, and improving the apparent reduction factor relative to the distribution measurement. Under this hypothesis, the true loss is expected to agree more closely with the OTDR and power meter predictions; this was not verified experimentally due to time constraints during the research stay. The time-correlated coincidences confirmed that the entangled pairs survive transmission through the building's fiber infrastructure, completing the distribution objective of this thesis.

Taken together, these results establish a fully characterized polarization-entangled photon source and a validated distribution link between the two laboratories, providing the experimental foundation on which the subsequent phases of the broader CTU project (Section 6.4) will extend.

6.2 Contributions and practical recommendations

Beyond resolving the entanglement degradation observed in this particular setup, the diagnostic approach developed in this work — combining the analytical PMD model with the numerical density-matrix simulation of Section 5.2.2 — is not specific to this experiment. It provides a transferable method for identifying and quantifying PMD-induced decoherence in any broadband SPDC source distributed through birefringent fiber, and could be applied directly to diagnose similar issues in future extensions of this project or in other entangled-photon distribution setups.

6.3 Impact and alignment with the UN Sustainable Development Goals

The United Nations 2030 Agenda for Sustainable Development establishes 17 Sustainable Development Goals (SDGs), adopted in 2015 as a shared framework for addressing global social, economic, and environmental challenges [35]. While this thesis is a laboratory-scale experimental work and does not aim to address these goals directly, three of them are significantly connected with the nature of the project and the way it was carried out.

Figure 36: United Nations Sustainable Development Goals addressed in this work: Goal 4 (Quality Education), Goal 9 (Industry, Innovation and Infrastructure), and Goal 17 (Partnerships for the Goals). Icons reproduced from the official United Nations SDG communications materials [35].

SDG 4 — Quality Education. This thesis was carried out as an international research stay, combining the academic training received at UPV with hands-on experimental work in quantum optics at CTU. Beyond the specific technical results, the project provided training in experimental methodology, problem diagnosis, and rigorous scientific reporting that goes beyond what a conventional university laboratory course can offer, contributing to the author's formation as a future engineer and researcher.

SDG 9 — Industry, Innovation and Infrastructure. The distribution of entangled photon pairs over real building-scale fiber infrastructure, rather than a controlled laboratory bench, is a direct step towards the infrastructure required for quantum communication networks. This work, together with its planned extensions (Section 6.4), provides a possible experimental basis for emerging quantum communication technologies, such as quantum key distribution and quantum networking.

SDG 17 — Partnerships for the Goals. This work was made possible by an international academic collaboration between two institutions, UPV (Spain) and CTU (Czech Republic), under joint supervision from both. This kind of cross-border academic partnership, in which students and supervisors from different countries collaborate on a shared research project, is itself an example of the cooperation that SDG 17 represents.

6.4 Future work

As I already indicated, this work forms part of a broader project at CTU that will continue beyond the timeframe of this thesis (Section 1.1). TThe next phase aims to establish the distribution between more than two nodes dynamically, using temporal multiplexing and a software layer that allocates entanglement on demand between pairs of nodes as required, rather than maintaining a single fixed point-to-point link.

Returning to the scope of this project, the polarization-entangled pairs characterized in this thesis are themselves the resource required for applications that go beyond simple time-correlation and rely on the polarization degree of freedom: quantum key distribution [2], where the polarization basis encodes the cryptographic key; entanglement-based teleportation [36], where an unknown polarization state is transferred between nodes using a shared entangled pair; entanglement swapping [37], which extends entanglement between nodes that have never directly shared a photon pair by performing a joint measurement at an intermediate node; and superdense coding [38], where entanglement allows more classical information to be transmitted per photon than would otherwise be possible. One of the requirements for realizing any of these applications would be the ability to distribute polarization-resolved entanglement over the existing fiber infrastructure. The architecture proposed below addresses this specific requirement.

The distribution experiment of Section 5.5 measures only time-correlated coincidences; recovering and distributing the polarization entanglement characterized in Sections 5.2–5.4 over the same inter-laboratory link was outside the scope of this work, but the infrastructure used here would support it with the addition of some extra components. Since each SMF channel rotates the photon polarization in a fixed but unknown way, this rotation can be compensated, to a large extent, rather than avoided: a polarization controller placed on each channel, just before the detectors, can undo the rotation introduced by that channel and recover a well-defined polarization state, without requiring any significant changes to the building's existing fiber infrastructure.

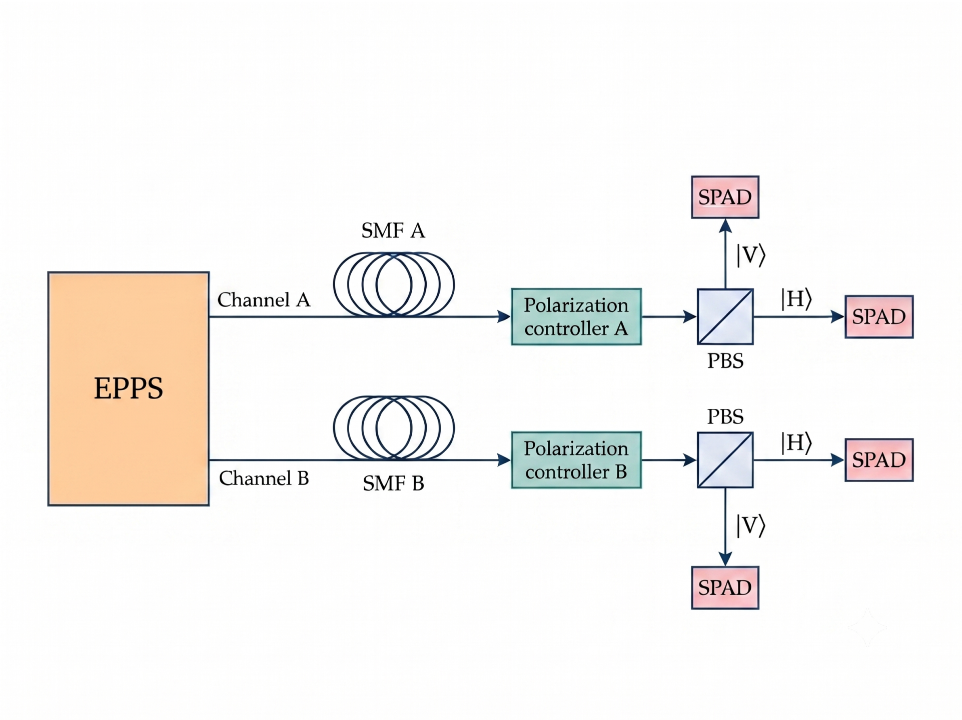

Figure 37: Proposed architecture for polarization-resolved distribution over the existing SMF infrastructure: a polarization controller on each channel compensates the unknown rotation introduced by the fiber, followed by a polarizing beam splitter (PBS) and two SPAD detectors per channel to resolve the two output polarization components.

The optimal setting of each polarization controller could be found either manually — by adjusting the waveplates while monitoring the detected count rates, in a similar way to the manual QST protocol of Section 4.4 — or automatically, with an optimization routine that iteratively adjusts the controller while maximizing a target metric (for instance, the coincidence rate in a chosen polarization basis). Once each channel is compensated, a PBS placed after each controller, with two SPAD detectors at its two output ports, would allow the two polarization components (e.g. $|H\rangle$ and $|V\rangle$) to be resolved independently on each channel. This architecture would provide the polarization-resolved entanglement distribution required as a building block for applications such as quantum key distribution or entanglement-based teleportation between the two laboratories. Even with this compensation, the purity recovered at the receiving end is hard to predict: the controller could improve it by correcting the projection mismatch introduced by the fiber rotation, but additional insertion loss, residual PMD over the full link, and imperfections in the compensating components would work in the opposite direction.

Bibliography

[1] Michael A. Nielsen and Isaac L. Chuang. *Quantum Computation and Quantum Information*. 10th Anniversary. Cambridge, UK: Cambridge University Press, 2010. ISBN: 978-1-107-00217-3.

[2] Charles H. Bennett and Gilles Brassard. "Quantum cryptography: Public key distribution and coin tossing". In: *Proceedings of the IEEE International Conference on Computers, Systems and Signal Processing*. Bangalore, India: IEEE, 1984, pp. 175–179.

[3] Artur K. Ekert. "Quantum cryptography based on Bell's theorem". In: *Physical Review Letters* 67.6 (1991), pp. 661–663. DOI: `10.1103/PhysRevLett.67.661`.

[4] Paul G. Kwiat et al. "New high-intensity source of polarization-entangled photon pairs". In: *Physical Review Letters* 75.24 (1995), pp. 4337–4341. DOI: `10.1103/PhysRevLett.75.4337`.

[5] European Commission. *European Quantum Communication Infrastructure (EuroQCI) Initiative*. Online. Signed by all 27 EU Member States since June 2019. `https://digital-strategy.ec.europa.eu/en/policies/quantum` [Accessed: June 2026]. 2019.

[6] Sören Wengerowsky et al. "Entanglement distribution over a 96-km-long submarine optical fiber". In: *Proceedings of the National Academy of Sciences* 116.14 (2019), pp. 6684–6688. DOI: `10.1073/pnas.1818752116`.

[7] Shi-Chang Zhuang et al. "Ultrabright Entanglement Based Quantum Key Distribution over a 404 km Optical Fiber". In: *arXiv preprint* (2024). arXiv:2408.04361 [quant-ph].

[8] Juan Yin et al. "Satellite-based entanglement distribution over 1200 kilometers". In: *Science* 356.6343 (2017), pp. 1140–1144. DOI: `10.1126/science.aan3211`.

[9] Hyang-Tag Lim, Kang-Hee Hong, and Yoon-Ho Kim. "Effects of polarization mode dispersion on polarization-entangled photons generated via broadband pumped spontaneous parametric down-conversion". In: *Scientific Reports* 6 (2016), p. 25846. DOI: `10.1038/srep25846`.

[10] Daniel F. V. James et al. "Measurement of qubits". In: *Physical Review A* 64.5 (2001), p. 052312. DOI: `10.1103/PhysRevA.64.052312`.

[11] Joseph B. Altepeter, Daniel F. V. James, and Paul G. Kwiat. "Qubit Quantum State Tomography". In: *Quantum State Estimation*. Ed. by Matteo G. A. Paris and Jaroslav Řeháček. Vol. 649. Lecture Notes in Physics. Berlin, Heidelberg: Springer, 2004, pp. 113–145. DOI: `10.1007/978-3-540-44481-7_4`.

[12] Roman Schmied. "Quantum state tomography of a single qubit: comparison of methods". In: *Journal of Modern Optics* 63.18 (2016), pp. 1744–1758. DOI: 10.1080/09500340.2016.1142018.

[13] Max Born and Emil Wolf. *Principles of Optics: Electromagnetic Theory of Propagation, Interference and Diffraction of Light*. 7th. Cambridge University Press, 1999.

[14] M. M. Fejer et al. "Quasi-phase-matched second harmonic generation: tuning and tolerances". In: *IEEE Journal of Quantum Electronics* 28.11 (1992), pp. 2631–2654. DOI: 10.1109/3.161322.

[15] S-Fifteen Instruments Pte. Ltd. *Entangled Photon Pair Source – Product Brochure*. Datasheet, EPPS_Product_Brochure_Rev03.pdf. Revision 03, July 2025, Singapore. 2025.

[16] Hans-A. Bachor and Timothy C. Ralph. *A Guide to Experiments in Quantum Optics*. 2nd. Weinheim: Wiley-VCH, 2004. DOI: 10.1002/9783527619238.

[17] Micro Photon Devices. *PDM-IR Series: Single Photon Avalanche Diode – Fiber-coupled module datasheet*. Datasheet, MPD_PDMIR_Datasheet_Fiber.pdf. Revision 1.1.5.

[18] J. P. Gordon and H. Kogelnik. "PMD fundamentals: Polarization mode dispersion in optical fibers". In: *Proceedings of the National Academy of Sciences* 97.9 (2000), pp. 4541–4550. DOI: 10.1073/pnas.97.9.4541.

[19] Corning Incorporated. *Corning® SMF-28® Ultra Optical Fiber*. Product Information Sheet PI-1424-AEN. [Accessed: June 2026]. 2014. URL: https://www.corning.com/media/worldwide/coc/documents/Fiber/product-information-sheets/PI-1424-AEN.pdf.

[20] Hanno Hammer. "Characteristic Parameters in Integrated Photoelasticity: An Application of Poincaré's Equivalence Theorem". In: *arXiv preprint* (2003). eprint: physics/0305034. URL: https://arxiv.org/abs/physics/0305034.

[21] William K. Wootters. "Entanglement of Formation of an Arbitrary State of Two Qubits". In: *Physical Review Letters* 80.10 (1998), pp. 2245–2248. DOI: 10.1103/PhysRevLett.80.2245.

[22] Asher Peres. "Separability Criterion for Density Matrices". In: *Physical Review Letters* 77.8 (1996), pp. 1413–1415. DOI: 10.1103/PhysRevLett.77.1413.

[23] Michał Horodecki, Paweł Horodecki, and Ryszard Horodecki. "Separability of mixed states: necessary and sufficient conditions". In: *Physics Letters A* 223.1–2 (1996), pp. 1–8. DOI: 10.1016/S0375-9601(96)00706-2.

[24] Guifré Vidal and Reinhard F. Werner. "Computable measure of entanglement". In: *Physical Review A* 65.3 (2002), p. 032314. DOI: 10.1103/PhysRevA.65.032314.

[25] Reinhard F. Werner. "Quantum states with Einstein–Podolsky–Rosen correlations admitting a hidden-variable model". In: *Physical Review A* 40.8 (1989), pp. 4277–4281. DOI: 10.1103/PhysRevA.40.4277.

[26] Santec Corporation. *OTF-300 Optical Tunable Filter – Product Datasheet*. Datasheet. Type OTF-300-12S2, range 1290–1330 nm, SMF, FC/APC,

[27] Swabian Instruments. *Time Tagger Series Product Brochure*. Datasheet, timetaggerseriesproductbrochurefeb2026.pdf. Feb. 2026.

[28] Thorlabs. *FBR-AH3 Achromatic Half-Wave Plate Module for FiberBench, 1100–2000 nm*. https://www.thorlabs.com/thorproduct.cfm?partnumber=FBR-AH3. [Accessed: June 2026].

[29] Thorlabs. *FBR-AQ3 Achromatic Quarter-Wave Plate Module for FiberBench, 1100–2000 nm*. https://www.thorlabs.com/thorproduct.cfm?partnumber=FBR-AQ3. [Accessed: June 2026].

[30] Thorlabs. *FBR-LPNIR Rotating Linear Polarizer Module, 650–2000 nm*. https://www.thorlabs.com/thorproduct.cfm?partnumber=FBR-LPNIR. [Accessed: June 2026].

[31] ID Photonics. *CoBrite DX4 Tunable Laser – Product Datasheet*. Datasheet. 2025.

[32] Thorlabs. *PM100A Handheld Optical Power and Energy Meter Console*. https://www.thorlabs.com/thorproduct.cfm?partnumber=PM100A. [Accessed: June 2026].

[33] EXFO. *FTB-720-12CD-23B-EI-EA OTDR Module for the FTB-1 Platform*. Datasheet. Single-mode/multimode OTDR module, 850/1300/1310/1550 nm.

[34] Nicholas Metropolis and Stanislaw Ulam. “The Monte Carlo Method”. In: *Journal of the American Statistical Association* 44.247 (1949), pp. 335–341. DOI: 10.1080/01621459.1949.10483310.

[35] United Nations General Assembly. *Transforming our world: the 2030 Agenda for Sustainable Development*. Resolution A/RES/70/1. 2015.

[36] Charles H. Bennett et al. “Teleporting an Unknown Quantum State via Dual Classical and Einstein-Podolsky-Rosen Channels”. In: *Physical Review Letters* 70.13 (1993), pp. 1895–1899. DOI: 10.1103/PhysRevLett.70.1895.

[37] Marek Żukowski et al. ““Event-Ready-Detectors” Bell Experiment via Entanglement Swapping”. In: *Physical Review Letters* 71.26 (1993), pp. 4287–4290. DOI: 10.1103/PhysRevLett.71.4287.

[38] Charles H. Bennett and Stephen J. Wiesner. “Communication via One- and Two-Particle Operators on Einstein-Podolsky-Rosen States”. In: *Physical Review Letters* 69.20 (1992), pp. 2881–2884. DOI: 10.1103/PhysRevLett.69.2881.

[39] Matteo G. A. Paris and Jaroslav Řeháček, eds. *Quantum State Estimation*. Vol. 649. Lecture Notes in Physics. Berlin, Heidelberg: Springer, 2004. ISBN: 978-3-540-22329-0. DOI: 10.1007/b98673.

[40] D. T. Smithey et al. “Measurement of the Wigner distribution and the density matrix of a light mode using optical homodyne tomography: Application to squeezed states and the vacuum”. In: *Physical Review Letters* 70.9 (1993), pp. 1244–1247. DOI: 10.1103/PhysRevLett.70.1244.

Part II

Appendices

Appendix A.

Additional listings

This appendix contains selected excerpts from the Python notebooks used for data processing and analysis throughout this thesis. The listings correspond to the core computational steps; routine file I/O, plotting, and exploratory code have been omitted for brevity.

A.1 Source characterization: peak and background extraction

The following excerpt, taken from the source characterization notebook (Section 5.1), identifies the coincidence peak in the raw histogram, shifts the time axis so the peak sits at $\Delta t = 0$, and computes the background level and the net coincidence count within the ±0.5 ns window used to obtain the SNR and CAR values reported in Table 11.

```python
# --- A. DETECTOR STATISTICS ---
ch3_col = 'Count rate (counts/s), channel 3'
ch4_col = 'Count rate (counts/s), channel 4'

print("=== SOURCE STATISTICS (10 dB) ===")
for label, col in [("Channel 3", ch3_col), ("Channel 4", ch4_col)]:
    mean_val = df_rate[col].mean()
    std_val = df_rate[col].std()
    var_val = df_rate[col].var()
    print(f"{label}: Average = {round(mean_val)} Hz | Std Dev = {
        round(std_val)} Hz | Variance = {round(var_val)} Hz^2")

# --- B. COINCIDENCE HISTOGRAM & DELAY CORRECTION ---
# Convert picoseconds to nanoseconds for readability
df_hist['Time_ns'] = df_hist['Time differences (ps)'] / 1000.0

# 1. Identify the natural peak position (physical delay due to
    fibers/spectrum)
max_counts = df_hist['Counts per bin'].max()
original_peak_pos_ns = df_hist.loc[df_hist['Counts per bin'].idxmax
    (), 'Time_ns']

# 2. Shift the time axis so the peak is exactly at 0.0 ns
```

```python
df_hist['Time_ns_shifted'] = df_hist['Time_ns'] - original_peak_pos_ns

# 3. Calculate background (accidental coincidences) away from the peak
baseline = df_hist[(df_hist['Time_ns_shifted'] < -2) | (df_hist['Time_ns_shifted'] > 2)]['Counts per bin'].mean()

# 4. Calculate the area of the peak (real entanglement pairs)
mask_peak = (df_hist['Time_ns_shifted'] >= -0.5) & (df_hist['Time_ns_shifted'] <= 0.5)
total_counts_window = df_hist[mask_peak]['Counts per bin'].sum()
num_bins_in_window = mask_peak.sum()
true_coincidences = total_counts_window - (baseline * num_bins_in_window)
```

Listing A.1: Peak identification and background estimation from the coincidence histogram.

A.2 Pauli operator basis

The 16 two-qubit operators T_j used as the basis for the density matrix parametrization (Section 3.6.1) are built from the tensor products of the single-qubit Pauli matrices.

```python
# Standard Pauli Matrices
sigma_0 = np.array([[1, 0], [0, 1]], dtype=complex)    # I (Identity)
sigma_1 = np.array([[0, 1], [1, 0]], dtype=complex)    # X (Diagonal basis)
sigma_2 = np.array([[0, -1j], [1j, 0]], dtype=complex) # Y (Circular basis)
sigma_3 = np.array([[1, 0], [0, -1]], dtype=complex)   # Z (Computational basis)
pauli_matrices = [sigma_0, sigma_1, sigma_2, sigma_3]

# Generate the 16 Gamma_j matrices (tensor product of Pauli matrices for 2 photons)
Gamma = []
for pauli_photon1 in pauli_matrices:
    for pauli_photon2 in pauli_matrices:
        Gamma.append(np.kron(pauli_photon1, pauli_photon2))  # tensor product (kron)
```

Listing A.2: Construction of the Pauli operator basis used in the tomographic reconstruction.

A.3 Design matrix construction

Each of the 36 measurement files is read and matched to its corresponding pair of polarization bases from the filename; the net coincidence count is extracted with the same peak/background procedure as in Appendix A.1, and the resulting $\hat{\Pi}_k$ is built as the tensor product of the two single-photon projectors. The design matrix A is assembled by evaluating $A_{kj} = \mathrm{Tr}(\hat{T}_j \hat{\Pi}_k)$ for every combination of measurement and Pauli operator (Section 3.6.2).

```
files = glob.glob("Bidirectional_histogram*.txt")
files.sort()  # Sort alphabetically to ensure consistent vector order

n_vector = []
P_k_matrices = []  # projector for each physical measurement
extracted_counts_dict = {}
valid_bases = ['H', 'V', 'D', 'A', 'R', 'L']
processed_count = 0

for file in files:
    # Clean the filename to extract just the two letters (e.g. "HH", "DA"...)
    base_name = os.path.basename(file).replace("Bidirectional_histogram_", "") \
                                       .replace(".txt", "").strip().upper()

    if len(base_name) >= 2:
        photon_1, photon_2 = base_name[0], base_name[1]

        if photon_1 in valid_bases and photon_2 in valid_bases:
            # Get net coincidences using the peak/background procedure
            net_counts = process_file(file)
            n_vector.append(net_counts)

            clean_key = f"{photon_1}{photon_2}"
            extracted_counts_dict[clean_key] = net_counts

            # Build the 2-photon projector
            P_k = np.kron(P_base[photon_1], P_base[photon_2])
            P_k_matrices.append(P_k)

            processed_count += 1

if processed_count != 36:
    print(f"CRITICAL WARNING: Processed {processed_count} valid files instead of 36.")
    print("The Moore-Penrose pseudoinverse might fail or give wrong results. Check your folder!")
else:
    print("Successfully processed exactly 36 valid measurement files.")

n_vector = np.array(n_vector)  # Our complete measurement vector

# Build Design Matrix A (rows = processed_count x 16 columns)
A = np.zeros((processed_count, 16), dtype=complex)
for k in range(processed_count):
    for j in range(16):
```

```
        A[k, j] = np.trace(Gamma[j] @ P_k_matrices[k])

A = np.real(A)
```

Listing A.3: Extraction of the 36 measurement counts and construction of the design matrix.

A.4 Maximum likelihood estimation with Cholesky parametrization

The cost function below implements the exact Poisson negative log-likelihood (Section 3.6.3). The 16 real parameters t_j define a lower triangular complex matrix T, which guarantees that the resulting density matrix is positive semi-definite and normalized by construction.

```
def mle_cost_function(t, n_measured, projectors, N_total):
    """
    Objective function: builds T, calculates the parameterized rho,
    and returns the exact Poisson negative log-likelihood.
    """
    # 1. Build lower triangular matrix T (16 real parameters)
    T = np.zeros((4, 4), dtype=complex)
    T[0,0] = t[0]
    T[1,0] = t[4] + 1j*t[5]
    T[1,1] = t[1]
    T[2,0] = t[10] + 1j*t[11]
    T[2,1] = t[6] + 1j*t[7]
    T[2,2] = t[2]
    T[3,0] = t[14] + 1j*t[15]
    T[3,1] = t[12] + 1j*t[13]
    T[3,2] = t[8] + 1j*t[9]
    T[3,3] = t[3]

    # 2. Parameterization (guarantees positive semi-definite & trace 1)
    T_dagger = T.conj().T
    rho_trial = (T_dagger @ T) / np.trace(T_dagger @ T)

    # 3. Exact Poisson negative log-likelihood
    total_error = 0.0
    for k in range(len(n_measured)):
        expected_prob = np.real(np.trace(rho_trial @ projectors[k]))
        n_expected = N_total * expected_prob
        if n_expected < 1e-9:
            n_expected = 1e-9
        total_error += n_expected - n_measured[k] * np.log(n_expected)

    return total_error

# Initial vector t0 (maximally mixed state: t1..t4 = 1, rest = 0)
t_initial = np.zeros(16)
t_initial[0:4] = 1.0

```

```
# Optimizer execution (L-BFGS-B algorithm)
opt_result = minimize(
    mle_cost_function,
    t_initial,
    args=(n_vector, P_k_matrices, N_total),
    method='L-BFGS-B',
    options={'maxiter': 5000, 'disp': False}
)

# Reconstruction of the optimal density matrix
t_opt = opt_result.x
T_opt = np.zeros((4, 4), dtype=complex)
T_opt[0,0] = t_opt[0]
T_opt[1,0] = t_opt[4] + 1j*t_opt[5]
T_opt[1,1] = t_opt[1]
T_opt[2,0] = t_opt[10] + 1j*t_opt[11]
T_opt[2,1] = t_opt[6] + 1j*t_opt[7]
T_opt[2,2] = t_opt[2]
T_opt[3,0] = t_opt[14] + 1j*t_opt[15]
T_opt[3,1] = t_opt[12] + 1j*t_opt[13]
T_opt[3,2] = t_opt[8] + 1j*t_opt[9]
T_opt[3,3] = t_opt[3]

rho_mle = (T_opt.conj().T @ T_opt) / np.trace(T_opt.conj().T @ T_opt
    )
```

Listing A.4: MLE cost function with Cholesky parametrization and optimizer execution.

A.5 Entanglement metrics and Werner-state fit

The functions below compute the full set of entanglement metrics introduced in Section 3.7 from the reconstructed density matrix $\hat{\rho}$, including the concurrence (Wootters' formula), the entanglement of formation, and the Werner parameter obtained by fitting $\hat{\rho}$ against the dominant eigenvector rather than a standard Bell state.

```
def partial_trace_B(rho):
    """Trace out photon B from a 4x4 two-qubit density matrix.
    Returns the 2x2 reduced density matrix of photon A.
    Basis: {|HH>, |HV>, |VH>, |VV>} -- photon A first, photon B
       second.
    """
    rho_A = np.zeros((2, 2), dtype=complex)
    rho_A[0, 0] = rho[0, 0] + rho[1, 1]
    rho_A[0, 1] = rho[0, 2] + rho[1, 3]
    rho_A[1, 0] = rho[2, 0] + rho[3, 1]
    rho_A[1, 1] = rho[2, 2] + rho[3, 3]
    return rho_A


def von_neumann_entropy(rho_2x2):
```

```
    """S(rho) = -sum(lambda_i * log2(lambda_i)), with 0*log(0) = 0."""
    eigvals = np.real(np.linalg.eigvalsh(rho_2x2))
    eigvals = np.clip(eigvals, 1e-15, 1.0)
    return float(-np.sum(eigvals * np.log2(eigvals)))


def concurrence(rho):
    """C(rho) = max(0, lambda_1 - lambda_2 - lambda_3 - lambda_4),
    where lambda_i are the eigenvalues in decreasing order of
    R = sqrt(sqrt(rho) . rho_tilde . sqrt(rho)),
    rho_tilde = (sigma_y (x) sigma_y) rho* (sigma_y (x) sigma_y).
    """
    sigma_yy = np.kron(sigma_2, sigma_2)
    rho_tilde = sigma_yy @ rho.conj() @ sigma_yy

    sqrt_rho = sqrtm(rho)
    R = sqrtm(sqrt_rho @ rho_tilde @ sqrt_rho)

    eigvals = np.sort(np.real(np.linalg.eigvalsh(R)))[::-1]
    return float(max(0.0, eigvals[0] - eigvals[1] - eigvals[2] -
        eigvals[3]))


def entanglement_of_formation(C):
    """E_F = h((1 + sqrt(1-C^2)) / 2), where h is the binary entropy
        ."""
    if C <= 0.0:
        return 0.0
    if C >= 1.0:
        return 1.0
    mu = (1.0 + np.sqrt(1.0 - C**2)) / 2.0
    mu = np.clip(mu, 1e-15, 1.0 - 1e-15)
    return float(-mu * np.log2(mu) - (1 - mu) * np.log2(1 - mu))


def werner_p_from_fidelity(F):
    """Werner parameter from fidelity to the closest pure state:
    F = (1 + 3p) / 4  ->  p = (4F - 1) / 3.
    """
    return float((4 * F - 1) / 3)


# Dominant eigenvector -- closest pure state to rho_mle
eigvals_rho, eigvecs_rho = np.linalg.eigh(rho_mle)
dominant_state = eigvecs_rho[:, -1]
F_max_pure = float(eigvals_rho[-1])

# Fidelity to the optimal pure state and corresponding Werner fit
F_optimal = float(np.real(dominant_state.conj() @ rho_mle @
    dominant_state))
p_werner_opt = werner_p_from_fidelity(F_optimal)
```

Listing A.5: Concurrence, entanglement of formation, and Werner-state fit.

A.6 PMD decoherence simulation

The following excerpt implements the density-matrix simulation of polarization mode dispersion discussed in Section 3.5. The initial Bell state is propagated through a birefringent fiber of length L for every frequency component of the photon's spectral distribution, and the resulting mixed state is obtained by averaging over the full spectrum.

```python
# Spectral bandwidth: 25 nm FWHM per photon, converted to angular frequency std dev
sigma_omega = (2*np.pi*c / lam0**2) * dlam_fwhm / (2*np.sqrt(2*np.log(2)))

# Gaussian spectrum S(omega), sampled +/- 6 sigma around omega0
omega = np.linspace(omega0 - 6*sigma_omega, omega0 + 6*sigma_omega, N_omega)
d_omega = omega[1] - omega[0]
S = np.exp(-0.5 * ((omega - omega0) / sigma_omega)**2)
S /= S.sum() * d_omega  # normalise so integral = 1

# Initial density matrix rho_0 = |psi><psi|, |psi> = (1/sqrt(2))(|HH> + |VV>)
psi0 = np.array([1, 0, 0, 1], dtype=complex) / np.sqrt(2)
rho0 = np.outer(psi0, psi0.conj())

def jones_operator(omega_val, dn, L):
    """Single-photon Jones operator for one fiber arm."""
    delta_phi = dn * L * omega_val / c
    return np.array([[1, 0],
                     [0, np.exp(1j * delta_phi)]], dtype=complex)

def two_photon_operator(omega_val, dn, L):
    """U(omega) (x) U(omega) in the 4-dimensional two-photon space."""
    U = jones_operator(omega_val, dn, L)
    return np.kron(U, U)

def compute_rho_final(dn, L):
    """rho_final = integral S(omega) * UU(omega) rho0 UU^dagger(omega) d_omega."""
    rho_final = np.zeros((4, 4), dtype=complex)
    for k, om in enumerate(omega):
        UU = two_photon_operator(om, dn, L)
        rho_k = UU @ rho0 @ UU.conj().T
        rho_final += S[k] * rho_k * d_omega
    return rho_final

# Sweep over fiber length L (PM fiber, 0 to 50 cm)
L_PM = np.linspace(0, 0.50, 60)
purity_PM, concurrence_PM = [], []
for L in L_PM:
    rho = compute_rho_final(dn_PM, L)
    purity_PM.append(purity(rho))
    concurrence_PM.append(concurrence(rho))
```

Listing A.6: Density-matrix simulation of PMD-induced decoherence as a function of fiber length.

A.7 Monte Carlo angular error analysis

The loop below implements the Monte Carlo analysis of Section 5.3. For each of the 500 realizations, a Gaussian angular error $\delta \sim \mathcal{N}(0, \sigma)$ is drawn independently for every waveplate and polarizer, the corresponding "real" projectors are built, and synthetic Poisson-distributed counts are generated from the reference state. The reconstruction is then performed using the nominal (error-free) projectors, exactly as in the laboratory, where the angular errors are unknown.

```python
purity_samples = np.zeros(N_ITER)
eigvals_samples = np.zeros((N_ITER, 4))
rho_samples = np.zeros((N_ITER, 4, 4), dtype=complex)

for i in tqdm(range(N_ITER)):
    # Polarizer errors: fixed for the 36 measurements
    d_pol_A = rng.normal(0.0, SIGMA_DEG)
    d_pol_B = rng.normal(0.0, SIGMA_DEG)

    # Build the 36 "real" projectors and simulate counts
    n_counts_sim = np.zeros(36)

    for k, joint in enumerate(twobits_states):
        wp_type_A, _ = LAB_STATES[joint[0]]
        wp_type_B, _ = LAB_STATES[joint[1]]

        # Waveplate errors: independent for each measurement, only if waveplate present
        d_wp_A = rng.normal(0.0, SIGMA_DEG) if wp_type_A != 'NONE' else 0.0
        d_wp_B = rng.normal(0.0, SIGMA_DEG) if wp_type_B != 'NONE' else 0.0

        # Build the "real" projector with all the errors applied
        Proj_real = joint_projector(joint[0], joint[1], d_wp_A, d_wp_B, d_pol_A, d_pol_B)

        # Expected count under the reference state and the real projector
        mu_k = max(0.0, N_total * np.real(np.trace(rho_ref @ Proj_real)))
        n_counts_sim[k] = rng.poisson(mu_k)  # add Poisson noise (shot noise)

    # Reconstruct rho assuming nominal projectors (the lab does not know delta)
    opt_result = minimize(
        mle_cost_function,
```

```
        t_initial,
        args=(n_counts_sim, PROJECTORS_NOMINAL, N_total),
        method='L-BFGS-B'
    )
```

Listing A.7: Monte Carlo loop for the angular error analysis.

A.8 OTDR analysis

The excerpt below parses the EXFO OTDR XML reports for both channels (Section 5.5.2), separates connector losses from fiber attenuation, and computes the transmission efficiency η used to predict the expected coincidence rate reduction reported in Section 5.5.3.

```
def parse_otdr_xml(filepath):
    """Parse an EXFO OTDR XML report and return a structured dictionary."""
    tree = ET.parse(filepath)
    root = tree.getroot()
    trace = root.find('.//Trace')

    lm = trace.find('LinkMeasurement')
    span_loss = float(lm.find('SpanLoss').text.replace(' dB', '').strip())
    span_length = float(lm.find('SpanLength').text.replace(' m', '').strip())

    segments = []
    for ev in trace.findall('.//Event'):
        loc = ev.find('Location').text.strip()
        typ = ev.find('Type').text.strip()
        loss_raw = ev.find('Loss').text.strip()

        loss_val = None
        if loss_raw not in (' ', '- -', ''):
            try:
                loss_val = float(loss_raw)
            except ValueError:
                pass

        # Parse location: either '0.0097' (connector) or '(0.0097 km)' (fiber section)
        if loc.startswith('(') and 'km' in loc:
            loc_km = float(loc.replace('(', '').replace(')', '').replace('km', '').strip())
            seg_type = 'fiber'
        else:
            loc_km = float(loc)
            seg_type = 'connector' if typ not in ('Launch Level', 'End of Fiber') else typ

        segments.append({'loc_km': loc_km, 'type': seg_type, 'loss_dB': loss_val})
```

```python

    return {'span_loss_dB': span_loss, 'span_length_m': span_length,
        'segments': segments}

# Load both channels and compute derived quantities
otdr = {ch: parse_otdr_xml(xml_file) for ch, xml_file in XML_FILES.
    items()}

for ch, d in otdr.items():
    connectors = [s for s in d['segments'] if s['type'] == '
        connector' and s['loss_dB'] is not None]
    fibers = [s for s in d['segments'] if s['type'] == 'fiber' and s
        ['loss_dB'] is not None]
    d['total_conn_loss'] = sum(c['loss_dB'] for c in connectors)
    d['total_fiber_loss'] = sum(f['loss_dB'] for f in fibers)
    d['eta'] = 10**(-d['span_loss_dB']/10)

# Expected coincidence reduction from the combined transmission of
    both channels
eta1_otdr = otdr['CH1']['eta']
eta2_otdr = otdr['CH2']['eta']
expected_reduction = 1 / (eta1_otdr * eta2_otdr)
```

Listing A.8: Parsing of OTDR XML reports and link budget calculation.

Full notebooks

The complete Jupyter notebooks used throughout this work — including the parts not shown above, such as reading the raw data files, generating plots, and exploratory steps — are available at: `https://github.com/slopmuo/TFG-Entangled-Photon-Distribution`

Appendix B.

Equipment datasheets

This appendix reproduces the specifications page of the datasheets for the three active components that generate, detect, and timestamp the data in the experiment, in the following order: the entangled photon pair source (S-Fifteen EPPS-O), the single-photon detectors (MPD PDM-IR), and the time-to-digital converter (Swabian Instruments Time Tagger 20 — note that the Time Tagger datasheet also lists the Time Tagger Ultra and Time Tagger X models, which were not used in this work). The remaining equipment listed in Table 9 — waveplates, polarizers, filters, and auxiliary instrumentation — is referenced in the Bibliography, where the corresponding datasheets can be consulted in full.

Polarization-entangled Photon-Pair Source - EPPS-O by S-Fifteen Instruments

1 Features

- Bright polarization-entangled photon pairs source
- Pair spectrum centered at 1320 nm
- Spectral width of 100 nm
- High polarization-entanglement visibility
- High brightness
- Minimum dispersion in G652/G657 fibers

Applications: Quantum key distribution, quantum metrology, absorption spectroscopy, 2-photon interference, sub-shot-noise imaging, random number generation, clock synchronization, ghost imaging, entanglement swapping

2 General Description

This photon pair source generates polarization-entangled photons at 1320 nm via spontaneous parametric down-conversion in a PPKTP crystal. The down-conversion process is driven with the integrated 660 nm pump laser achieving a photon pair rate >500 000 pairs/s and a photon-heralding probability of >30%. The spectrally non-degenerate photons in each pair are separated with a wavelength-division multiplexer. The visibility >96% of the polarization-entangled photons makes it an ideal photon-pair source for quantum optics applications.

3 Specifications

Table 1: Device specifications

Photon Pair Source Performance	
Center wavelength	1320 nm
Bi-photon bandwidth	100 nm
Photon pair rate	>500 000 pairs/s (before detection)
Polarization-entanglement visibility	>96%
Photon-heralding probability	>25%
Photon Output Fibers	ITU-T G.657.A1
Software Control	
Physical port	USB 2.0, Type B
Communication	Serial communication via virtual COM port / USB CDC ACM class
Crystal temperature	Ambient temperature to 70°C
Laser temperature	18–40°C
Laser current	0–100 mA
Electrical Specifications	
Power Supply	12 V DC, Max. 50 Watt, 2.1mm Barrel socket, Supply included
Physical dimensions	
Size (L x W x H)	350 mm x 155 mm x 70 mm
Weight	3.4 kg

PDM-IR control

The PDM-IR module is controlled through a PC software interface or an SDK library. With the user-friendly software, it is possible to set all the programmable parameters, like gate settings, SPAD settings, outputs, and get the counters value. The software can save and load up to 10 configurations and set one of them as power up configuration. The power up configuration is automatically applied and the SPAD is turned on after few seconds from the powering time. Concerning the SPAD parameters, hold-off time, excess bias voltage and SPAD temperature are all user-selectable to get the best results from the measurement.

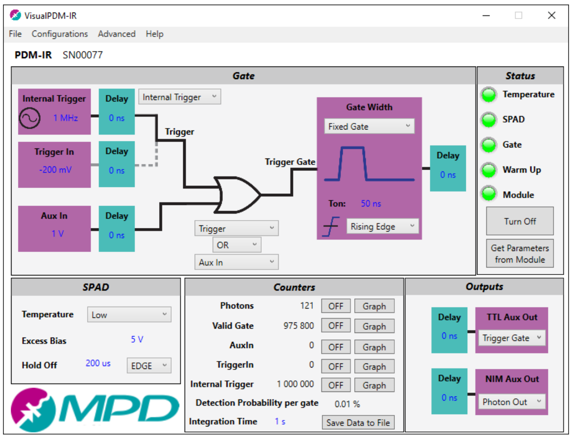

Specifications[1]

Parameter	Notes		Min	Typ	Max	Units
Fiber pigtail type	FC/PC – uses 10 µm SPAD		SMF-28[2]			
	FC/PC – uses 25 µm SPAD		MMF 50 µm GI, NA = 0.2[2]			
Photon Detection Efficiency	V_{EX} = 7 V, λ = 1550 nm			25		%
Timing jitter (FWHM)	At V_{EX} = 4 V (all working modes)	10 µm SPAD	130	200		ps
		25 µm SPAD	90	130		ps
	At V_{EX} = 7 V (Fixed Gate mode only)	10 µm SPAD[3]	70	100		ps
		25 µm SPAD	50	70		ps
IRF decay time	At V_{EX} = 4 V. For λ < 975 nm photons start to be absorbed in the top InP layer, decay time increases			60	100	ps
DCR (dark counting rate)	At V_{EX} = 2 V, Temperature set to "*Low*", module in free running mode, hold-off time = 100 µs. In case of the SFF module, case temperature was kept at 25°C	SMF-28 SFF		0.5	1.2	kcps
		SMF-28 DI		0.25	0.6	kcps
		MMF-50GI DI/SFF		2.6	5	kcps
SPAD temperature	SW selectable, four predefined values		225		243	K
Gate rise time	(20% – 80%)			2		ns
Excess bias range	Free Gate and Free Running		2		5	V
	Fixed Gate		2		7	V
Hold-off time	SW selectable @ 10 ns step		1 µ		3 m	s
Gate width	SW selectable @ 1 ns step		1 n		1.5 m	s
Gate repetition frequency					100	MHz
Internal trigger frequency	SW selectable @ 1 Hz step		100		100 M	Hz
Delay path	SW selectable @ 1 ns step		0		100	ns
Counter integration time	SW selectable @ 20 ms step		0.1		60	s
PHOTON OUT, NIM OUT	NIM output (50 Ω termination required)		-800		0	mV
PHOTON OUT	Pulse width			10		ns
TRIGGER IN, AUX IN	Amplitude		-2		3	V
	Input impedance			50		Ω
	Pulse width		800			ps
TTL OUT	Output levels (when 50 Ω terminated)		0		2.7	V
Power supply DI	included AC/DC power supply		80 - 264 VAC, 47 - 63 Hz			
	Power consumption				80	W
	Module DC INPUT voltage (for reference only)			24		V
Power supply SFF	included AC/DC power supply		100 - 240 VAC, 50 - 60 Hz			
	Power consumption				20	W
	Module DC INPUT voltage (for reference only)			12		V
Operating range	Ambient temperature		15		35	°C

[1]See the user-manual for the full list of module's specifications. Module designed and built compliant with the European Union Directive 2011/65/CE.
[2]Exposed fiber of SFF module version is not light-tight thus any measurement (including DCR characterisation) should ensure a proper and complete fiber shielding.
[3]A secondary bump, three orders of magnitude below the main IRF peak and within 3 ns of it, may appear when V_{EX} > 6 V.

Specifications

Timing precision	Time Tagger 20	Time Tagger Ultra		Time Tagger X
RMS jitter (typical)	34 ps	42 ps (Value)	8 ps (Performance)	2 ps
RMS jitter (typical, HighRes)	-	3 / 4 / 6 ps (2 / 4 / 8 HighRes channels)		1.5 ps (5 HighRes channels)
FWHM jitter (typical)	80 ps	100 ps (Value)	19 ps (Performance)	4.7 ps
FWHM jitter (typical, HighRes)	-	7 / 10 / 14 ps (2 / 4 / 8 HighRes channels)		3.5 ps (5 HighRes channels)
digital resolution	1 ps	1 ps		1 ps

Processing capabilities			
input channels	8	4 to 18	4 to 20
dead time	6 ns	2.1 ns	1.5 ns
data rate (USB to PC)	9 Mtags/s	90 Mtags/s	90 Mtags/s
data rate (SFP+, QSFP+ to FPGA)	-	-	300, 1200 Mtags/s
burst memory	8 Mtags	512 Mtags	512 M tags
maximum input frequency	167 MHz	475 MHz	700 MHz

Input signals			
input impedance	50 Ω	50 Ω	50 Ω / 1 MΩ
recommended input signal range	0 to 3 V	-3 to 3 V	-1.5 to 1.5 V
input signal range	-0.3 to 5 V	-5 to 5 V	-3 to 3 V
trigger level range	0 to 2.5 V	-2.5 to 2.5 V	-1 to 1 V
minimum pulse width	1000 ps	500 ps	350 ps
minimum pulse height	100 mV	100 mV	100 mV

External clock input			
frequency	-	10 MHz or 500 MHz	10 MHz or 500 MHz
coupling	-	AC, 50 Ω	AC, 50 Ω
amplitude	-	1 to 3 Vpp	0.5 to 4 Vpp

General parameters			
data interface	USB 2.0	USB 3.0	USB 3.0, SFP+, QSFP+
size (L x W x H) in mm	145 x 100 x 50	190 x 140 x 60	380 x 480 x 90 (2U)

Typical performance

Instrument response

1 MHz square wave, 1 Vpp, 1 ns rise, applied to two input channels, trigger 50%. The standard deviation σ of the distribution measures the jitter of two input channels. The RMS jitter of each individual channel is σ/√2. The FWHM jitter of each channel is 2.35 σ/√2.

RMS Jitter

The plots show the RMS jitter obtained from instrument response measurements with all pairs of the first 8 input channels.

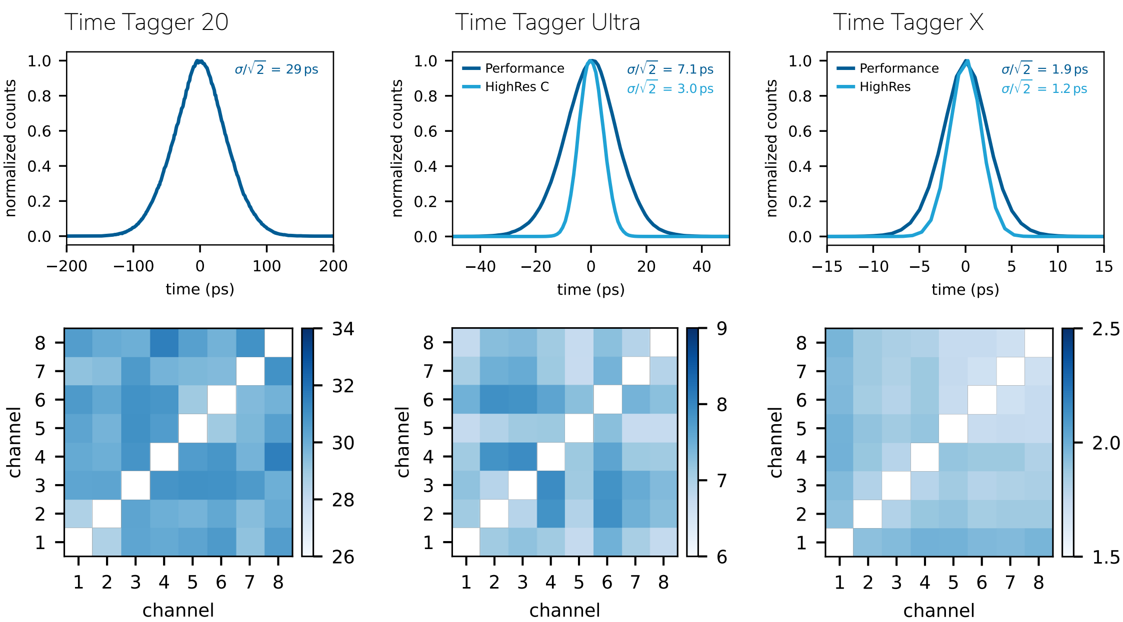

Appendix C.

Third-party image licences

Figure 9 is reproduced from:

> Lim, H.-T., Hong, K.-H. & Kim, Y.-H. *Effects of polarization mode dispersion on polarization-entangled photons generated via broadband pumped spontaneous parametric down-conversion.* Sci. Rep. **6**, 25846 (2016).
> `https://doi.org/10.1038/srep25846`

Figure 4 is adapted from:

> Smite-Meister. *Bloch sphere.svg*. Wikimedia Commons.
> `https://commons.wikimedia.org/wiki/File:Bloch_sphere.svg`
>
> The-tenth-zdog (derivative work). *Poincare Sphere with Polarizations.svg*. Wikimedia Commons.
> `https://commons.wikimedia.org/wiki/File:Poincare_Sphere_with_Polarizations.svg`